

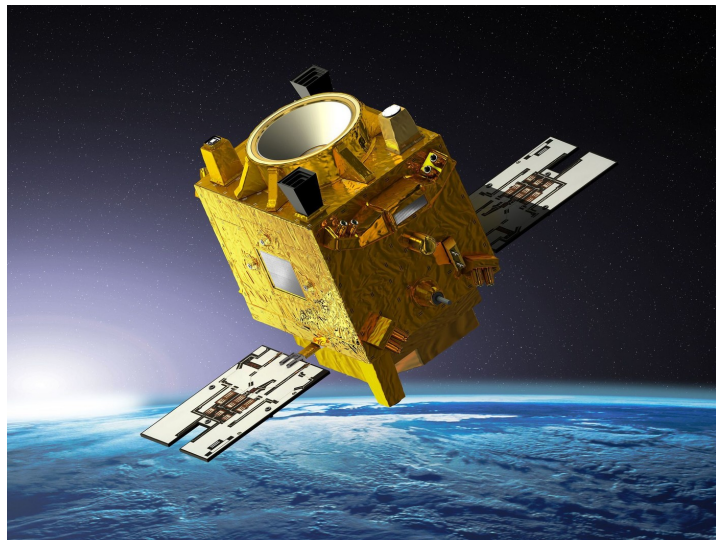
Improvement of the instrumental model for the MICROSCOPE space mission

Master Thesis Report

by

Sébastien Belis

**MSc Student at TU Delft
Student Number: 4630548**



as part of

MSc Space Flight - Space Exploration profile

in MSc. Aerospace Engineering

at Delft University of Technology

Tutors: Dr. ir. E.J.O Schrama TU Delft
Manuel Rodrigues ONERA - The French Aerospace Lab

Thesis Committee: Prof. dr. ir. Pieter Visser Astrodynamics and Space Missions
Dr. Pavel Ditmar Physical and Space Geodesy
Dr. ir. E.J.O Schrama Astrodynamics and Space Missions
Dr. ir. Jose van den IJssel Astrodynamics and Space Missions

Preface

This Master thesis position has been a great opportunity to confront the theoretical knowledge I have acquired through such courses as Satellite Data Processing, Space Instrumentation, and Mission Orbit Design, during my first year at TU Delft, to experimental needs in a space company.

I would like to thank particularly my internship supervisor Manuel Rodrigues, as well as my thesis supervisor Ernst Schrama for the strong support they gave me throughout my research. Despite their respective key role within ONERA and TU Delft, and therefore their busy schedule, Manuel and Ernst have always found time to guide my work, give me advice, and discuss the various difficulties and interrogations I have met in my work, with infinite patience and pedagogy. I feel I have learned a lot during this Master thesis, and it is mainly thanks to them. I would also like to thank the IEA Service team who helped me to blend in and to achieve my several objectives. Additionally, I would like to thank my family, my girlfriend and my friends for their continuous support. Their combined energy has given me at times the extra motivation, strength and confidence necessary to complete this work.

Abstract

The MICROSCOPE mission launched on April 25th 2016 represents the first space-based test of the Equivalence Principle, one of the foundational pillars of the well-known Einstein's theory of General Relativity established in 1915. This principle is indeed challenged by some theories attempting to unify General Relativity and Quantum Mechanics, such as the string theory. The MICROSCOPE mission therefore intends to confirm or overturn the Equivalence Principle by testing one of its basis, known as the universality of free-fall, with an unrivaled precision objective of 10^{-15} (meaning a precision a hundred times higher than the one obtained with the current experiment set-up on Earth). The test is performed by means of a differential accelerometer, on board a drag-free microsatellite, in which two test-masses of different materials are held on the same trajectory by means of electrostatic forces. The masses are concentric coaxial cylinders, each surrounded by a set of electrodes allowing both detection and control of the test-mass position in six degrees of freedom (3 translations and 3 rotations). A difference observed in the the forces required to maintain their common center of mass would prove a violation of the universality of free fall, and hence, of the Equivalence Principle. If an EP violation should be pointed out, this would involve that Einstein's General Relativity theory, on which is based all modern physics, has to be completed. On the contrary, if no violation should be identified by the mission, this would bring additional constraints on some alternative theories predicting an EP violation, and thus would represent a step forward for the Science field. Because of the high sensitivity of the instrument, the measurement precision is limited by a number of perturbations. Among these perturbations, the knowledge of certain instrument parameters (inertial or dimensional) is crucial for the accuracy of the computations. These parameters nonetheless cannot be estimated on-ground with the required precision. Dedicated in-orbit calibration sessions have therefore been designed and implemented within the mission scenario to finely characterize some of them and thus correct the measurement. Various other perturbations are taken into account during the data processing, such as saturation events due to the satellite environment (impact with micrometeorites), instrument noise, random thermal fluctuations and data gaps in the measurement (caused by transmission losses or outliers). A protocol has thus been elaborated to carefully process the scientific data. The first results of the experiment released on December 2017, and based on 120 orbits among the 1900 realized so far by the microsatellite, have allowed to deduce the non-violation of the Equivalence Principle with an accuracy of about $2 \cdot 10^{-14}$ (improvement of one order of magnitude compared to the current most precise on-ground experiments). Nonetheless, these first results have been computed with conservative upper limits for some errors, such as coupling defects and thermal sensitivity. The data collection will continue until the end of the mission in October 2018. The processing of the additional scientific data will allow a more thorough analysis of the errors perturbing the measurement, and thus the design of more accurate models for the overestimated perturbations, leading to an improvement of the mission performance. This is the purpose of this Master thesis project.

Keywords: MICROSCOPE microsatellite, satellite instrumentation, test of the Equivalence Principle, satellite data processing, electrostatic accelerometer, coupling defects, thermal sensitivity

Contents

Preface	iii
Abstract	v
List of Figures	ix
List of Tables	xi
List of Acronyms	xiii
	xv
Introduction	xvii
1 Experimental tests for the Equivalence Principle	1
1.1 The Equivalence Principle	1
1.2 Interests of an Equivalence Principle test	2
1.3 On-ground experimental tests of the Equivalence Principle: State-of-the-art	2
1.4 Motivation for a space-based experiment	4
2 The MICROSCOPE experiment	7
2.1 Description of the MICROSCOPE space mission	7
2.2 Presentation of the payload: The T-SAGE instrument	10
2.2.1 Instrument overview	10
2.2.2 Operating principle of the servo-controlled electrostatic accelerometer	12
2.3 The measurement equation	16
2.3.1 Derivation of the applied electrostatic acceleration	17
2.3.2 Instrument imperfections	19
2.3.3 Derivation of the measured electrostatic acceleration	20
2.3.4 Estimation of the WEP violation parameter	22
2.3.5 Other perturbations in the measurement	22
3 Coupling between axes	25
3.1 Definition of the coupling between axes	25
3.2 Exploitation of the in-orbit calibration sessions	25
3.2.1 Overview of the calibration sessions	25
3.2.2 Presentation of the instrumental model	26
3.2.3 Processing of the calibration sessions in the investigation of the coupling factors:	31
3.3 Exploitation of a new type of mission phase	38
3.4 Design of an instrument simulator	43
4 Thermal Sensitivity of the instrument	51
4.1 Thermal perturbations in the measurement process	51
4.2 Thermal mission phases	53
4.2.1 Presentation of the thermal mission phases	53
4.2.2 Exploitation of the thermal sessions in the investigation of the instrument thermal sensitivity	53
5 Conclusion and prospects	57
Bibliography	59
A Anti-Aliasing Filter	63
B Control Functions Parameters	65

C	Detailed results of the calibration sessions processing	67
C.1	K_{1dx} calibration sessions	67
C.2	Θ_{dz} calibration sessions.	68
C.3	Θ_{dy} calibration sessions	68
D	Outputs provided by the simulator	69
D.1	Simulator using the linear-to-linear coupling factors first estimates	69
D.1.1	Simulation n°2: Satellite oscillation along the Y-axis	69
D.1.2	Simulation n°3: Satellite oscillation along the Z-axis	70
D.2	Simulator using the adjusted linear-to-linear coupling factors	70
D.2.1	Simulation n°1: Satellite oscillation along the X-axis	70
D.2.2	Simulation n°2: Satellite oscillation along the Y-axis	71
D.2.3	Simulation n°3: Satellite oscillation along the Z-axis	71

List of Figures

1.1	Illustration of the torsion pendulum experiment [31]	3
2.1	Attitude and Orbit Control Loop [2]	8
2.2	(Left side) Inertial Mode configuration. (Right side) Spin mode configuration. Increasing the spin rate increases the WEP test frequency. The blue arrows represent the orientation of the instrument axis. [7]	9
2.3	(Left side) T-SAGE instruments. (Right side) Cross Section of the Sensor Unit [4].	10
2.4	Electrode Configuration for the SAGE instrument. The test-mass is included (in yellow) in both diagrams. The X and ϕ control uses variations of the covering area, that is to say the area of the test-mass facing the electrodes. Radial control (Y, Z, θ and ψ) uses variations of the gap between the test-mass and the electrode [4].	11
2.5	Test-mass control loop [18]	12
2.6	Variation of Capacitance due to mass displacement. (Left side) Gap variation. (Right side) Covering area variation [7].	13
2.7	Test-mass control by gap variation. The electrostatic force is attractive, so the accelerometer electrodes act in pairs to provide both a positive and a negative force, but with a different magnitude. The resulting force tends to bring the test-mass at its equilibrium point, at the center of the cage [7].	15
2.8	Test-mass control by variation of the covering area [7].	16
2.9	PSD noise model on the X-axis considering all noise sources [7].	20
2.10	OLS uncertainty with respect to the number of gaps per orbit. [7]	23
3.1	(a) Illustration of the instrument loop along the X-axis, for a K_{1dx} calibration session. The axes labelled <i>IS1</i> refer to the internal test-mass axes and those labelled <i>IS2</i> refer to the external test-mass axes. (b) Another illustration of the instrument loop along the X-axis, for a K_{1dx} calibration session, with a detailed representation of the accelerometer control laws.	27
3.2	General form of a Proportional-Integral-Differential controller	28
3.3	Illustration of the instrument loop for the linear and angular axes, for a K_{1dx} calibration session.	30
3.4	Bode Diagram of the estimated linear AOCS block transfer function with respect to the real magnitude and phase values provided by the <i>CNES</i>	33
3.5	Acceleration measured in-orbit along the linear axes during a K_{1dx} calibration session	34
3.6	Illustration of the instrument control loop along the X-axis for the technical session n°516	39
3.7	Acceleration measured in-orbit along the linear axes during the technical session n°516	39
3.8	Illustration of the pure phase delay in the drag-free control loop - XIS2 sensor	40
3.9	Illustration of the <i>Simulink</i> Simulator of the instrument	43
3.10	Outputs provided by the instrument simulator for the first simulation (Excitation along the X-axis)	45
3.11	Confrontation between the amplitudes of the accelerations provided by each simulator sensor, and the values measured in-flight during dedicated mission phases	50
4.1	Illustration of the MICROSCOPE Payload Block [4]	52
4.2	Evolution of both the SU (in blue) and the FEEU (in orange) temperatures throughout a SU thermal session realized with the SUEP instrument	53
4.3	Evolution of both the SU (in blue) and the FEEU (in orange) temperatures throughout a FEEU thermal session realized with the SUEP instrument	53
A.1	Gain diagram of an ideal anti-aliasing filter	63
A.2	Bode diagram of a 5 th Butterworth filter with a cut-off frequency $f_c = 2\text{Hz}$	64

D.1	Outputs provided by the simulator for the second simulation (Excitation along the Y-axis) - Coupling factors first estimates	69
D.2	Outputs provided by the simulator for the third simulation (Excitation along the Z-axis) - Coupling factors first estimates	70
D.3	Outputs provided by the simulator for the first simulation (Excitation along the X-axis) - Coupling factors adjusted values	71
D.4	Outputs provided by the simulator for the second simulation (Excitation along the Y-axis) - Coupling factors adjusted values	71
D.5	Outputs provided by the simulator for the third simulation (Excitation along the Z-axis) - Coupling factors adjusted values	72

List of Tables

1.1	Eötvös parameter values obtained with both the torsion pendulum and the LLR experiments . . .	4
3.1	Gain and Phase values of the linear AOCS system for discrete values of frequency, provided by the <i>CNES</i>	32
3.2	Estimated values for the parameters of the linear AOCS block transfer function	33
3.3	Algorithm used to extract the differential linear-to-linear coupling factors from the K_{1dx} calibration sessions	36
3.4	Processing of the $K_{1dx-DFIS2}$ calibration sessions and 3- σ estimation of $(\alpha_{XYIS1} - \alpha_{XYIS2})$ and $(\alpha_{XZIS1} - \alpha_{XZIS2})$ for the SUEP instrument	36
3.5	Processing of the $K_{1dx-DFIS1}$ calibration sessions and 3- σ estimation of $(\alpha_{XYIS2} - \alpha_{XYIS1})$ and $(\alpha_{XZIS2} - \alpha_{XZIS1})$ for the SUEP instrument	37
3.6	Processing of the Θ_{dy} and Θ_{dz} calibration sessions and 3- σ estimation of the remaining differential linear-to-linear coupling factors for the SUEP instrument	38
3.7	Processing of the K_{1dx} , Θ_{dy} and Θ_{dz} calibration sessions and 3- σ estimation of the differential linear-to-linear coupling factors for the SUREF instrument	38
3.8	Algorithm used to extract the linear-to-linear coupling factors from the technical session n°516	42
3.9	Processing of the technical session n°516: estimation of the linear-to-linear coupling factors and confrontation with the results obtained with the calibration sessions	42
3.10	Results obtained with the instrument simulator - Linear-to-linear coupling factors initialized with the values computed in section 3.3	45
3.11	Algorithm used to adjust the values of the linear-to-linear coupling factors	46
3.12	Adjusted linear-to-linear coupling factors provided by the optimization process	47
3.13	Results obtained with the instrument simulator using the adjusted linear-to-linear coupling factors	47
4.1	Algorithm used to extract the instrument thermal sensitivity from the thermal sessions	54
4.2	Processing of the SU thermal session and estimation of the SU temperature sensitivity λ	55
B.1	Values of the control functions parameters for the internal test-mass of both the SUEP and the SUREF instrument	65
B.2	Values of the control functions parameters for the external test-mass of the SUEP instrument	66
B.3	Values of the control functions parameters for the external test-mass of the SUREF instrument	66
C.1	Processing of the $K_{1dx-DFIS2}$ calibration sessions and 3- σ estimation of $(\alpha_{XYIS1} - \alpha_{XYIS2})$ and $(\alpha_{XZIS1} - \alpha_{XZIS2})$ for the SUREF instrument	67
C.2	Processing of the $K_{1dx-DFIS1}$ calibration sessions and 3- σ estimation of $(\alpha_{XYIS2} - \alpha_{XYIS1})$ and $(\alpha_{XZIS2} - \alpha_{XZIS1})$ for the SUREF instrument	67
C.3	Processing of the $\Theta_{dz-DFIS2}$ calibration sessions and 3- σ estimation of $(\alpha_{YXIS1} - \alpha_{YXIS2})$ and $(\alpha_{YZIS1} - \alpha_{YZIS2})$ for the SUEP instrument	68
C.4	Processing of the $\Theta_{dz-DFIS2}$ calibration sessions and 3- σ estimation of $(\alpha_{YXIS1} - \alpha_{YXIS2})$ and $(\alpha_{YZIS1} - \alpha_{YZIS2})$ for the SUREF instrument	68
C.5	Processing of the $\Theta_{dy-DFIS2}$ calibration sessions and 3- σ estimation of $(\alpha_{ZXIS1} - \alpha_{ZXIS2})$ and $(\alpha_{ZYIS1} - \alpha_{ZYIS2})$ for the SUEP instrument	68
C.6	Processing of the $\Theta_{dy-DFIS2}$ calibration sessions and 3- σ estimation of $(\alpha_{ZXIS1} - \alpha_{ZXIS2})$ and $(\alpha_{ZYIS1} - \alpha_{ZYIS2})$ for the SUREF instrument	68

List of Acronyms

AOCS	Attitude and Orbit Control System
CNES	Centre National d'Etudes Spatiales
DOF	Degree Of Freedom
DVA	Digital Voltage Amplifier
EEP	Einstein's Equivalence Principle
EP	Equivalence Principle
ESA	European Space Agency
FEEU	Front End Electronic Unit
GR	General Relativity
ICU	Interface Control Unit
LLR	Lunar Laser Ranging
MICROSCOPE	MICROSatellite with drag free control for the Observation of the Equivalence Principle
OLS	Ordinary Least Squares
ONERA	<i>Office National d'Etudes et de Recherches Aerospatiales (The French Aerospace Lab)</i>
PID	Proportional-Integral-Derivative controller
PSD	Power Spectral Density
SUEP	Sensor Unit for the test of the Equivalence Principle
SUREF	Reference Sensor Unit
T-SAGE	Twin-Space Accelerometers for Gravitation Experiment
WEP	Weak Equivalence Principle

*“Life is like riding a bicycle. To keep your balance,
you must keep moving.”*

Albert Einstein

Introduction

For decades, fundamental physics has been able to accurately interpret an ever wider range of phenomena, going from the cosmological universe to the quantum world of particles, but it is now facing new challenges in its attempt to fully explain the dynamics of celestial bodies at the scales of galaxies. The dynamics of bodies separated by astrophysical distances, is driven by a fundamental interaction named gravitation and accurately described by the General Theory of Relativity developed by the well-known physicist Albert Einstein in 1915 [8]. The general relativity is a geometric theory describing the gravitational interaction as an effect of the space-time curvature, due to the mass and energy it contains. This theory has been proven remarkably accurate and robust through several experiments over the last century [32], such as, recently, the direct observation of gravitational waves from a binary black hole merger as predicted by the general relativity [6]. These tests have allowed to confirm, with the precision of experimental means, the compatibility of the theory with observations.

The general theory of relativity is based on the Equivalence Principle, providing that all bodies fall in the same way in a uniform gravitational field, irrespective of their internal structure, mass and composition. The universality of free fall, stating that in a uniform gravitational field, the acceleration undergone by any particle is independent of its nature, is a concrete consequence of the Equivalence Principle. This statement leads to the equality between the gravitational mass of a body, representing the intensity of the gravitational force undergone by it, and its inertial mass, determining its ability to oppose any movement or modification of state imparted to it. In other terms, the effects on a body of a constant acceleration, and of a uniform gravitational field cannot be distinguished. This last formulation is named the Weak Equivalence Principle (WEP). Einstein later extended the WEP to the invariance of all laws of physics for an observer in free-fall within a uniform gravitational field, referred to as the Einstein Equivalence Principle (EEP) [19].

Nonetheless, the physicists Stephen Hawking and Roger Penrose's singularity theorem, produced in 1970 [20], suggests that the standard model of general relativity and particle physics is incomplete in that it cannot fully explain the origin of the universe known as the "Big Bang" singularity. Indeed, the "Big Bang" singularity is a point of space-time where the theory necessarily breaks down. Theorists are therefore currently trying to elaborate a unified theory of both quantum and cosmological scales. Some of these theories, such as the string theory [24], predict the existence of new interactions which could depend on the composition of the particles, and therefore challenge the Equivalence Principle. To confirm or rule out the new theoretical developments, the general theory of relativity needs to be more precisely tested by experimenting one of its pillars: the WEP.

Since the beginning of the 17th century, several experiments have been undertaken in order to test the Equivalence Principle [11]. The most precise test developed up to now is the lunar laser-ranging (LLR) method, using the precise measurement of the distance separating the Moon from the Earth over a long period of time provided by laser telemetry to investigate the fall of the Moon within the Sun's gravitational field [35]. The current state-of-the-art ground-based WEP tests reach a precision of the order of 10^{-13} , but are nonetheless limited by instabilities inherent to the near-Earth environment, such as the non-uniformity of the gravitational field, thermal fluctuations and seismic perturbations. A space-based experiment would overcome these limitations and thus allow a more precise test.

The MICROSCOPE space mission, developed by the French national center for space studies (referred to as CNES), represents the first space-based test of the equivalence principle, and will attempt to achieve an unrivaled precision of 10^{-15} [28] (two orders of magnitude better than the best ground-based results to date). The experiment consists in a modified free-fall test in which two test-masses are maintained on the same trajectory by means of electrostatic forces. A difference observed in the forces necessary to maintain the test-masses common center of mass will indicate a violation of the equivalence principle. The MICROSCOPE mission was successfully launched on April 25th, 2016 from Kourou, French Guyana and placed on a near-polar,

quasi-circular Sun-synchronous orbit at an altitude of 711 kilometers. The satellite carries on-board the T-SAGE Experiment (standing for Twin Space Accelerometers for space Gravity Experiment). This experiment, constituting the only payload of the 330-Kg satellite, is composed of two differential electrostatic accelerometers developed by the French national aerospace research center (referred to as ONERA). Each electrostatic accelerometer computes the acceleration of two concentric cylindrical and coaxial test-masses. In the accelerometer referred to as SUREF, the two test-masses have the same composition: a platinum-rhodium alloy. SUREF is used both as a calibration and as an experimental reference. In the second accelerometer, referred to as SUEP, the two test-masses have a different composition: the inner mass is made of a titanium alloy while the outer mass is made of the same platinum-rhodium as in the SUREF accelerometer. The test-masses are servo-controlled by surrounding electrodes which maintain them at the center of the accelerometer sensor cages by applying small accelerations. Thanks to this servo-control loop, each test-mass is maintained on the same trajectory and undergo the same gravitational field. The instruments are designed to operate in orbit, where only very weak accelerations are required to maintain the masses position. The signal investigated during the mission is then the difference between the electrostatic accelerations applied by the electrodes to the internal and external test-masses, projected on the test-masses longitudinal axis (named the sensitive axis of the accelerometer) and referred to as the differential acceleration. These projected accelerations vary during an orbit revolution because of the satellite attitude control. A violation of the weak equivalence principle would thus be highlighted by a periodic characteristic difference observed between the measured accelerations of the SUEP test-masses. In order to improve the precision of the measurements, additional servo-loops have been set up to reduce non-gravitational accelerations for the six degrees of freedom of the satellite (three translations and three rotations). This is achieved by cold gas microthrusters driven by the measurements provided by the accelerometers.

The success of the MICROSCOPE mission relies on a thorough and careful data analysis to point out a possible signal of a WEP violation among time variations observed in the data caused by other physical phenomena such as perturbations due to the instrument imperfections. Some of the perturbations, such as small misalignments in the satellite design, can be accurately modeled and corrected; Some other perturbations occur at frequencies different than the equivalence principle test, and thus induce a bias in the measurement. These perturbations, coupled with unpredictable events within the satellite, or in the satellite environment, could limit the accuracy of the MICROSCOPE experiment. The instruments must therefore be carefully characterized to identify the effects of any imperfections, and to measure the sensitivity of the instrument to its environment.

A scientific article presenting the first results of the MICROSCOPE experiment has been released on December 2017 [29]. Up to now, the results have allowed to deduce a non-violation of the WEP with a precision of about $2 \cdot 10^{-14}$, constituting an improvement of one order of magnitude in comparison with the current most precise on-ground experiments. Nonetheless, the results have been computed with conservative upper limits for some errors, such as coupling defects and thermal sensitivity. The forthcoming sessions of the mission will thus be dedicated to a more detailed analysis of the systematic errors, by integrating the signal of the differential accelerometer over longer periods of time. The design of more accurate models for the overestimated errors, from the analysis of the additional scientific data available by the end of the mission (in October 2018), will allow an improvement of the mission performance, and thus to get closer to the mission precision objective. This is the purpose of this Master thesis project. The thesis will therefore carefully investigate the various ways in which the instrumental model used for the MICROSCOPE data processing can be improved. A thorough and detailed study of satellite data processing and space instrumentation as well as an in-depth analysis of the satellite environment and mission scenario will be essential in the completion of the research objective.

The [chapter 1](#) will review the motivation for a weak equivalence principle test as well as the state-of-the-art experiments in this area. The [chapter 2](#) will present the MICROSCOPE satellite as well as the T-SAGE experiment. This chapter will lead to the formulation of the measurement equation, and the description of the various perturbations to take into account in the data processing. The following chapters will be dedicated to the improvement of the model used for some perturbations limiting the measurement precision: the [chapter 3](#) will present a plan to thoroughly estimate the coupling factors of the instrument, while the [chapter 4](#) will investigate the instrument thermal sensitivity.

Chapter 1

Experimental tests for the Equivalence Principle

Contents

1.1 The Equivalence Principle	1
1.2 Interests of an Equivalence Principle test	2
1.3 On-ground experimental tests of the Equivalence Principle: State-of-the-art	2
1.4 Motivation for a space-based experiment	4

This first chapter will introduce the challenges of the MICROSCOPE space mission: the motivations for an Equivalence Principle test will be developed, and the current state-of-the-art experiments in this field, as well as their limits, will be thoroughly presented.

1.1. The Equivalence Principle

As previously stated in the introduction, the MICROSCOPE mission aims at testing the Equivalence Principle through one of its foundation, known as the universality of free fall. Although this phenomenon can be observed in nature, it however has no theoretical basis.

Newton was the first physicist to distinguish between an inertial mass m_I , defining the ability of a body to oppose any movement or modification of state that is imparted on it, and a gravitational mass m_g , which represents the intensity of the gravitational force undergone by a body. Throughout his investigation of the gravity behavior, Newton noticed that the gravitational acceleration does not depend on the composition of the masses [12], and hence, that the inertial mass m_I is proportional to the gravitational mass m_g . The assumption of the equality of the two masses is known as the Weak Equivalence Principle (WEP) and constitutes the first manifestation of the equivalence principle. It has been verified by Newton in 1686 with a precision of about 10^{-3} , by means of pendulums made of various materials [14]. The Eötvös parameter is defined as the difference in acceleration undergone by two test bodies exposed to the same gravitational field:

$$\eta_{1,2} = \frac{a_1 - a_2}{(a_1 + a_2)/2} = 2 \frac{\frac{m_{g,1}}{m_{I,1}} - \frac{m_{g,2}}{m_{I,2}}}{\frac{m_{g,1}}{m_{I,1}} + \frac{m_{g,2}}{m_{I,2}}}$$

The WEP can therefore be translated into $\eta_{i,j} = 0$ for all bodies i and j .

Over two hundred years later, Einstein expanded the WEP, proposing the complete equivalence between an accelerated reference frame and a reference frame in a gravitational field, as a foundation for the General Relativity (geometric theory interpreting the gravitational interaction as an effect of the curvature of space-time due to the mass and energy it contains [1]). The Einstein Equivalence Principle (EEP) can be summarized by three conditions:

- The WEP is valid
- Non-gravitational experiments are independent of the velocity of their reference frame (referred to as the local Lorentz invariance)
- Non-gravitational experiments are independent of when and where they are performed (referred to as the local position invariance)

A theory violating the WEP would automatically violate the EEP; a theory satisfying the WEP but violating the EEP could be possible, but yet hard to imagine ([10] gives an example of particles that would spin while falling, betraying the effect of gravitation).

The equivalence principle has not only profound implications on the nature of spacetime, but leads to physical effects that can be inferred from it without writing any relativistic equation. It constitutes one of the pillars of the theory of General Relativity, which is, up to now, the most accurate theory describing the gravitational interaction. This theory has allowed to describe several phenomenon, both qualitatively and quantitatively with a high accuracy, such as the existence of gravitational waves generated from black hole mergers([5]), the gravitational redshift ([25]), and the perihelion advance of Mercury ([23]). Nonetheless, some phenomenon observed, especially at large astronomical scales, remain unexplained by the theoretical development stated. This suggests a need to perform ever more accurate tests of general relativity.

1.2. Interests of an Equivalence Principle test

As previously introduced, although General Relativity has been verified experimentally, it is not, at present, considered as a complete theory. It is indeed unable to explain some anomalies observed in astrophysics, such as the accelerating expansion of the universe (investigated from the observation of supernovae [26]). This anomaly has been regarded as a proof of the existence of a dark energy provided with a negative pressure tending to accelerate the expansion of the universe. However, this anomaly could also result from deviations from the theory of General Relativity. This type of anomaly encourages the need for ever precise tests of the theory.

Moreover, there is a well-known contradiction between the two different descriptions of the world currently available known as the geometric theory of gravitation and the quantum field theory. This contradiction motivates the development of a gravitational theory compatible with the Standard Model describing the three other fundamental forces (weak, strong and electromagnetic). Some new theoretical developments are therefore currently investigated to unify both the quantum and the gravitational theory. Among these trials are string theory models which try to unify all fundamental interactions and postulate that particles can be modeled by one-dimensional strings whose vibrational state determines the properties of the particles. One of these states gives rise to a particle, named graviton, carrying the gravitational interaction. Nonetheless, string theory models can lead to violations of the equivalence principle at different levels ([33]): a violation anywhere from 10^{-14} to 10^{-23} could be possible. An equivalence principle test is therefore of great interest for the progress toward unification of the fundamental interactions. The confirmation of equivalence, to any accuracy, would increase the range of confirmed validity of general relativity, and also places more stringent constraints on modern theories.

1.3. On-ground experimental tests of the Equivalence Principle: State-of-the-art

The previous subsection showed that a modification of general relativity in an effort to build a universal theory of astronomic and quantum scales may lead to a violation of the equivalence principle, motivating the need for a more precise test than previous experiments. Numerous tests of the equivalence principle currently exist. Free fall testing offers a direct measurement of the ratio between the inertial and the gravitational mass, and thus, a direct verification of the WEP. This subsection will briefly review the most accurate experimental tests of the WEP that have been performed up to now: the torsion pendulum experiment and the lunar laser telemetry. A given WEP experimental test is characterized by three main parameters: **the nature of the test bodies investigated, the gravitational source used, and the range of the gravitational interaction.**

Torsion pendulum experiment

In 1885, the physicist Loránd Eötvös implemented a WEP experiment based on a torsion pendulum. The instrument consists in two test-masses, made of different material, attached at both ends of an ideally massless rigid frame (also named rod) supported by a torsion fiber as illustrated [Figure 1.1](#). The suspension point is chosen to annul the torque caused by the gravitational forces undergone by the test-masses.

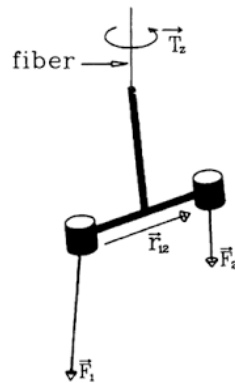


Figure 1.1: Illustration of the torsion pendulum experiment [\[31\]](#)

On [Figure 1.1](#), \vec{F}_1 and \vec{F}_2 denote the resulting external forces undergone respectively by the test-masses 1 and 2, \vec{r}_{12} represents the vector joining the two ends of the horizontal frame. The torque T_z about the fiber axis is expressed by the following relation:

$$T_Z = \frac{(\vec{F}_1 \times \vec{F}_2) \cdot \vec{r}_{12}}{\|\vec{F}_1 + \vec{F}_2\|} \quad (1.1)$$

The term $(\vec{F}_1 \times \vec{F}_2)$ in the previous relation shows that the torque on the wire depends on the angle between \vec{F}_1 and \vec{F}_2 . A WEP violation would be expressed by an inequality of the ratios of the gravitational and inertial forces $\left(\frac{F_{G,k}}{F_{I,k}}, k = 1, 2\right)$ of the two test-masses. A difference observed between these two ratios would mean that the resulting external forces \vec{F}_1 and \vec{F}_2 applied on the two test-masses are not parallel. According to [Equation 1.1](#), a non-null torque would therefore be induced about the fiber axis. This would result in a rotation of the horizontal frame with respect to its initial position (eventually stopped by the wire stiffness). Torsion pendulums thus permit extremely sensitive WEP experiments because they only respond to a difference in the directions of the resulting external forces applied on the two test-masses, not to a difference in their magnitude. The principle of the experiment allows instruments with tolerances of the order of 10^{-5} to make measurements with a much higher precision. In 1889, this process allowed Eötvös and his team to obtain a precision of 10^{-9} . Then, the Dicke's experiment, located in Princeton, reached a precision of about 10^{-11} in 1965 [\[27\]](#), followed by the Braginsky's experiment in Moscow with a precision of 10^{-12} on the Eötvös parameter [\[9\]](#).

These experiments are nonetheless limited by the inhomogeneity of the gravitational field and by imperfections in the geometry of the instrument, causing small gravity gradients and thus inducing a slight difference in the directions of the resulting external forces undergone by the two masses. A better resolution of a WEP violation can however be obtained by rotating the torsion pendulum with respect to the gravitational attractor, in order to make the signal of interest sinusoidal. The experiments of both the Princeton and Moscow groups mentioned above used the Sun as the gravitational attractor and let the rotation of the Earth provide the rotation of the instrument. This configuration nonetheless has some disadvantages, such as the weakness of the gravitational source and the distance between the attractor and the test-bodies ($149.6 \cdot 10^6$ kilometers). Besides, the noise sources increase when the frequency decreases.

At the end of the 20th century, the Eötvös Washington group managed to improve the torsion pendulum experiment by means of plates rotating with varying frequency in the Earth's gravitational field [\[31\]](#). An appropriate arrangement of masses around the instrument as well as a horizontal and rotational symmetry of

the design were implemented in order to limit the local gravitational gradients. To improve the precision of the experiment, the Eötvös-Washington group settled several other devices such as a vacuum chamber to reduce the air drag, thermal shields, and a control of the alignment of the wire with the local vertical. The measurement of the pendulum twist is achieved through the auto-collimation of an optical device. With these improvements implemented, the best precisions reached up to now are $1.8 \cdot 10^{-13}$ for beryllium-titanium test-bodies and $1.5 \cdot 10^{-13}$ for beryllium-aluminum test-bodies [16]. Currently, the main limitations of the torsion pendulum test can be divided into, on the one hand, the systematic errors due to time-dependent local gradients, and on the other hand, the thermal fluctuations from the damping losses of the wire. Moving away from on-ground gravity and thermal fluctuations by setting the test in space would allow a better control of the mentioned error sources.

Lunar laser ranging

The WEP can also be experimented by considering astronomical bodies. The Lunar Laser Ranging (LLR), or lunar laser telemetry, provides time series of precise measurements of the distance separating the Earth from the Moon. The valuable information provided by this data allows to determine if, according to the WEP, both celestial bodies fall within the gravitational field of the Sun at the same rate, in spite of their different compositions, masses and gravitational energies. The particularity of LLR experiment compared to the torsion pendulum tests is that it involves massive bodies with masses not negligible regarding the surrounding gravitational field.

The WEP test uses precise measurement of the distance between the Earth and the Moon over a long period of time, provided by laser telemetry. The LLR relies on the emission and reception by a ground-based telescope of a laser pulse between an on-ground station and a retroreflector cube placed on the Moon's surface. The lunar retroreflectors were installed during the American manned space mission Apollo 11, 14, 15, and by the Russian robotics space missions Lunokhod 1 and 2 [34]. The Earth-Moon distance is then deduced from the pulse round-trip travel time. The current experiments allow a centimetric precision on the distance measurement. Because of both the dispersion of the pulse and the refraction effects, the telescope only collects 1 photon every 100 laser shots of 10^{19} photons each. Nonetheless, to achieve a millimeter-range precision, more photons must be received by the telescope. Indeed, more collected photons would allow to compute an average round-trip travel time of the pulse and therefore improve the precision of the measurement. Such a specification requires a larger telescope. This is the purpose of the project named Apache Point Observatory Lunar Laser-ranging Operation and referred to as APOLLO project, that uses a 3.5-meter telescope and thus allowing the collection of more than one photon per laser shot [22].

The careful analysis of precise LLR measurements of the Earth-Moon distance provides increasingly strict limits on any WEP violation: current WEP experimental tests based on the lunar laser telemetry experiment reach a precision up to $1.8 \cdot 10^{-13}$ [36], and the APOLLO project is expected to allow the gain of one additional order of magnitude. The precision of this experiment nonetheless remains limited by some modelling errors. To improve the precision of the test, the errors in the position of the on-ground LLR observatory and of the lunar retroreflectors, as well as the errors in the pulse round-trip travel time caused by the atmosphere crossing, need to be carefully modelled. These errors being inherent to the near-Earth environment, a space-based experiment could overcome them.

Table 1.1: Eötvös parameter values obtained with both the torsion pendulum and the LLR experiments

EP Experiment	Torsion Pendulum		Lunar Laser Ranging
Test Bodies	Beryllium-Titanium	Beryllium-Aluminum	Earth-Moon
Eötvös parameter value	$1.8 \cdot 10^{-13}$	$1.5 \cdot 10^{-13}$	$1.8 \cdot 10^{-13}$

1.4. Motivation for a space-based experiment

The main arguments justifying a space-based experiment in order to achieve the precision objective of the mission are:

- The space environment provides soft and stable conditions to perform the experiment, and allows to

be freed from all on-ground perturbation sources, such as the electromagnetic, thermal and vibrational perturbations induced by human activity. These perturbations can be consistently reduced or, at least, easily controlled in space. Moreover, the Earth's gravity gradient fluctuations are lower than on ground because of the decrease of all the derivatives of the gravitational potential with distance.

- An in-orbit experiment provides long free-fall times in steady conditions since the signal can be integrated during several orbits to average the stochastic disturbances. The duration of free-fall can thus be several days.

This first chapter has carefully introduced the equivalence principle as a cornerstone to discriminate between new proposals for unified theories in modern physics. These new theoretical developments require a step forward in the precision of the equivalence principle test, in order to better constrain the key-parameters of the theories (in case of a non-violation of the WEP) or to pave the way for new physics (in case of a violation). The current state-of-the-art experiments reach a precision of 10^{-13} on the Eötvös parameter. However these on-ground experiments are limited by near-Earth environment perturbations (sismic or thermal) or errors in the modelling of Earth dynamics. A space-based test would therefore overcome these limitations: this statement leads to the design of the MICROSCOPE space mission that would be thoroughly presented in the next chapter.

Chapter 2

The MICROSCOPE experiment

Contents

2.1 Description of the MICROSCOPE space mission	7
2.2 Presentation of the payload: The T-SAGE instrument	10
2.2.1 Instrument overview	10
2.2.2 Operating principle of the servo-controlled electrostatic accelerometer	12
2.3 The measurement equation	16
2.3.1 Derivation of the applied electrostatic acceleration	17
2.3.2 Instrument imperfections	19
2.3.3 Derivation of the measured electrostatic acceleration	20
2.3.4 Estimation of the WEP violation parameter	22
2.3.5 Other perturbations in the measurement	22

The [chapter 1](#) motivated the needs for a more precise equivalence principle test to better constraint new theoretical developments in modern physics, and presented the limits of the current state-of-the-art on-ground experiments. This chapter will now introduce the MICROSCOPE space mission as a first space-based test of the equivalence principle, attempting to reach an unrivaled precision of 10^{-15} on the Eötvös parameter. The payload of the satellite, referred to as the T-SAGE experiment will be thoroughly described and justified. This description will lead to both the derivation of the model equations used to estimate the WEP violation parameter, and the presentation of the various perturbations limiting the measurement precision.

2.1. Description of the MICROSCOPE space mission

MICROSCOPE is a French acronym standing for Microsatellite with drag free control for the observation of the Equivalence Principle. The MICROSCOPE space mission has been designed by the French space agency CNES as a relatively low cost, first space-based test of the Equivalence Principle. This experiment benefits from a highly precise measurement instrument, a low noise environment, as well as the availability of long measurement duration to attempt to reach an unrivalled precision of 10^{-15} on the Eötvös parameter [28].

The microsatellite, placed on a low-Earth orbit, carries on board a set of two differential electrostatic accelerometers referred to as the T-SAGE experiment (an acronym for Twin Space Accelerometers for Gravitational Experiment) and constituting the primary payload of the mission. Both accelerometers are specifically designed to contain and control two test-masses for the space-based test. The test-masses, made of different material, are precisely placed on the same orbit around Earth, and will naturally continue on the same free-fall trajectory only if the equivalence principle holds. The MICROSCOPE experiment differs from the traditional ground-based WEP tests introduced in [chapter 1](#) because, while previously the difference in

the trajectories followed by the test-masses would be measured, with MICROSCOPE, the masses are forced through an electrostatic set-up to maintain the same trajectory, and the difference in the required restoring forces is investigated. Such an active control of the test-masses is allowed by both a detection of their position by capacitive sensing and the implementation of a servo-controlled loop. The levitation of the test-masses is achieved by surrounding electrodes exerting electrostatic forces on them. Indeed, the instrument has been designed to operate in orbit, where only very weak accelerations are required to maintain the masses position. To allow the test-masses to undergo the exact same gravitational field, their shapes are concentric coaxial cylinders, so that the distance between their centers of inertia is as little as possible.

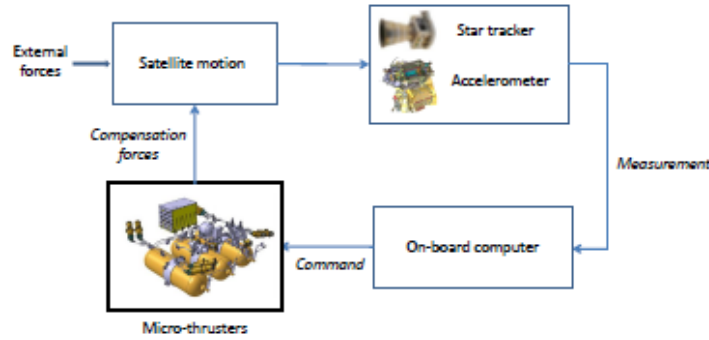


Figure 2.1: Attitude and Orbit Control Loop [2]

The payload of the space mission is constituted of two SAGE instruments, developed by the French aerospace laboratory ONERA, whose characteristics will be described in detail in [section 2.2](#). In the first electrostatic accelerometer (referred to as SUREF), the two test-masses are made of the same material: a platinum-rhodium alloy (more precisely, 10% rhodium and 90% platinum). This instrument serves both as a confirmation of the test precision and results, and as a calibration, to detect any bias in the measurements provided by the sensors. In the second accelerometer (referred to as SUEP), the two test-masses have a different composition: the external mass is made of a titanium alloy (4% vanadium, 6% aluminium and 90% titanium) while the inner mass is made of the same platinum-rhodium alloy as in the SUREF instrument. A WEP violation would be highlighted by a difference observed between the electrostatic accelerations applied to the SUEP test-masses, resulting in a violation signal proportional to the Eötvös parameter δ and to the gravitational acceleration at the satellite altitude. The materials composing the test-masses have been selected by taking into account both theoretical test aspects and more practical concerns of their physical properties: a significant difference in subatomic particles between the two materials increases the probability of a detectable WEP violation.

The MICROSCOPE satellite is part of the CNES Myriade line [3], which was initially developed to send low-cost scientific missions on geocentric orbits. The Attitude and Orbit Control System (AOCS) is provided by one star sensor, the science instruments themselves, and a set of cold gas thrusters. This innovative control system measures and compensates for all non-gravitational forces imparted to the microsatellite, including the solar radiation pressure and the atmospheric drag. For both the SUREF and the SUEP instruments, the signal of interest is the differential acceleration, defined as the difference between the electrostatic accelerations applied to the two test-masses to maintain them on the same trajectory. Since the non-gravitational forces act equally on both test-masses, their effect should be nullified by computing the differential acceleration, and thus, compensating the atmospheric drag should not be a necessary condition for the MICROSCOPE experiment. Nonetheless, because of the imperfections of the two sensors, a disturbing term, proportional to the common acceleration, defined as the average acceleration measurement from the two masses, and thus to the non-gravitational forces is introduced. The drag compensating system is thus essential to annul the coupling between the common and differential accelerations. The AOCS loop is illustrated in [Figure 2.1](#). The control system uses the acceleration measurement from one of the test-masses (depending on the session) of the instrument under test (SUREF or SUEP), as well as data from the star tracker to complete the angular rates of the test-masses for precise attitude control. These measurements are then sent to the on-board

computer that determines the commands to be sent to the cold gas microthrusters in order to correct for the external perturbation acting on the satellite. The cold gas propulsion system is ideal for drag-compensation as it enables to apply micro-newton thrusts of short duration. This drag compensating system is essential for the mission performance, reducing to less than $10^{-12} m \cdot s^{-2}$ the drag-free residual acceleration at the WEP test frequency, while its stochastic fluctuations are lower than $10^{-10} m \cdot s^{-2} \cdot \sqrt{Hz}$.

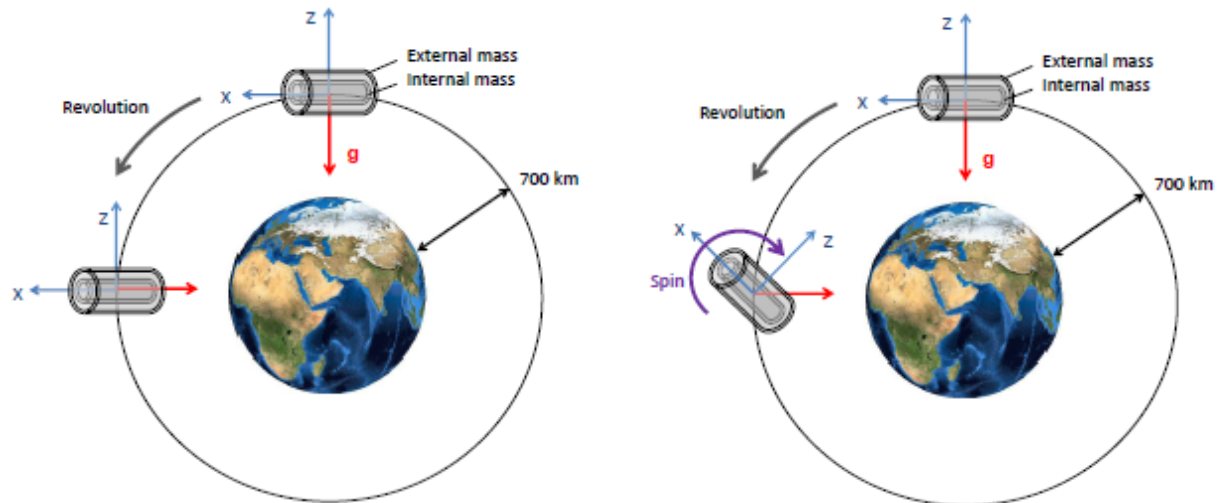


Figure 2.2: (Left side) Inertial Mode configuration. (Right side) Spin mode configuration. Increasing the spin rate increases the WEP test frequency. The blue arrows represent the orientation of the instrument axis. [7]

The MICROSCOPE microsatellite has been placed on a quasi-circular and quasi-polar geocentric orbit. With such an orbit, chosen to be Sun-synchronous and with an inclination of 98.5° , the periods of eclipse are minimal to allow a relative thermal stability during long measurement periods while providing an optimal power supply during all the mission. The orbit eccentricity had to be below $5 \cdot 10^{-3}$ to maintain the gravitational signal as constant as possible and thus to avoid perturbing effects on the measurement due to the Earth's gravity gradient. The chosen orbit altitude is 700km, in order to maximize the intensity of the Equivalence Principle test signal (which is proportional to the magnitude of the gravity field), while limiting the atmospheric drag to levels which can be compensated by the cold gas thrusters of the AOCS.

One of the particularity of the MICROSCOPE mission is the ability to finely tune the frequency at which the test is performed. This is achieved thanks to the satellite attitude control. The attitude control can function in two modes as illustrated in Figure 2.2. For the Inertial pointing mode, the sensitive axis of the instrument (the longitudinal axis of the test-mass cylinder) is maintained parallel to the orbital plane, while for the Spin configuration, the microsatellite rotates around the axis perpendicular to the orbital plane. Modifying the frequency of the test signal can confirm that the possible WEP violation signal is independent of other perturbing effects. It also allows to bring the frequency of the test signal closer to the frequency corresponding to the minimum instrumental noise, as explained in subsection 2.3.2. The lowest test frequency, corresponding to the Inertial mode, is equal to the orbital frequency $f_{orb} = 1.66 \cdot 10^{-4} Hz$. In spin mode, the test frequency is equal to the sum of the orbital and spin frequencies $f_{orb} + f_{spin}$. To better reject the orbital frequency perturbations, the spin frequency should not be an even multiple of the orbit frequency.

The acceleration measurement provided by the accelerometer inertial sensor is not rigorously equal to the electrostatic acceleration applied to the test-masses. The measured acceleration is derived from the correction voltage applied to the surrounding electrodes, and therefore undergoes slight defects throughout the measurement process [17]. These defects are divided into, on the one hand, the systematic errors (including axis couplings and misalignment, non linearity and scaling differences), and the stochastic errors (including electronic noise, thermal fluctuations and stochastic variations of the applied electrostatic forces). The stochastic errors can be reduced down to a desired level by both increasing the frequency of the WEP test

(by increasing the spin rate of the satellite), and integrating numerous data points over a long enough period of time. Because of the systematic errors, the accuracy of the measurements is limited by the partial knowledge of the physical parameters of the instrument. Therefore, for the MICROSCOPE experiment to reach the required precision, important in-orbit calibration sessions are needed to finely characterize the instrument and thus to correct the measurement. During these calibration phases, the satellite and the instrument are excited in various ways with a known sinusoidal signal to estimate the desired instrument characteristics. Throughout the mission, the in-orbit calibration sessions as well as the WEP test sessions have been performed several times in different conditions.

In order to both pilot the various mission operational phases and carefully process the data received from the satellite, a dedicated ground segment has been established, divided in two parts:

- The Microsatellite Ground Segment (MIGS), located in the CNES center in Toulouse and composed of the control and command centre as well as the ground station network. The MIGS receives the telemetry from the satellite and transmits it to the drag compensation system expertise center (whose French acronym is CECT).
- The scientific mission center (whose French acronym is CMS), located in the ONERA facilities near Paris, responsible for both the scientific data processing and the mission and payload monitoring.

2.2. Presentation of the payload: The T-SAGE instrument

The SAGE (Space Accelerometer for Gravitational Experimentation) instrument is a differential electrostatic accelerometer containing two test-masses whose positions are controlled in six degrees of freedom (three translations X, Y, Z , and three rotations ϕ, θ, ψ) by means of electrostatic forces. This instrument follows a long line of electrostatic accelerometers developed by ONERA. Nonetheless, it significantly differs from the previous instruments because of its high accuracy requirements, and its particular configuration with two concentric, coaxial and cylindrical test-masses. This subsection will carefully describe the design of the SAGE instrument, and the requirements needed to reach the performance objectives.

2.2.1. Instrument overview

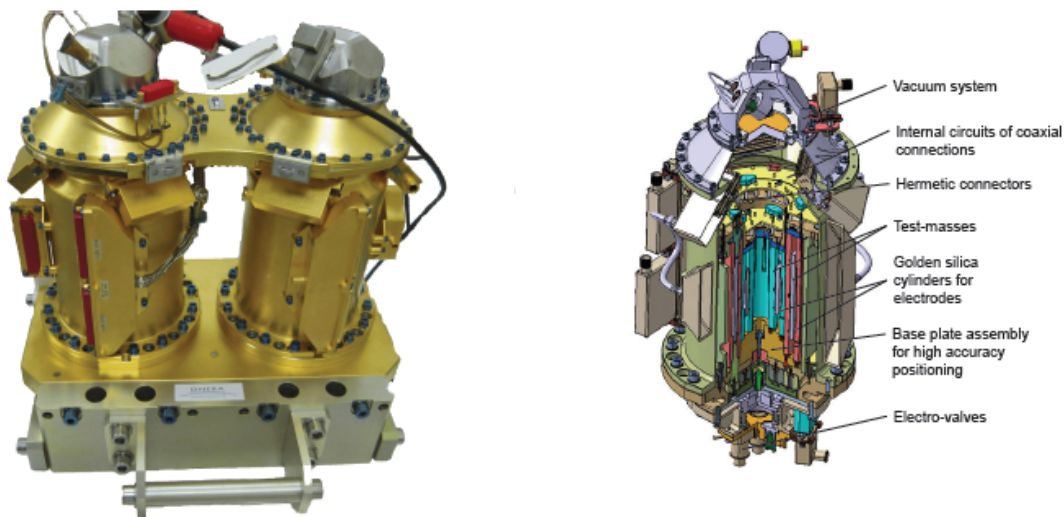


Figure 2.3: (Left side) T-SAGE instruments. (Right side) Cross Section of the Sensor Unit [4].

As previously mentioned in [section 2.1](#), the payload used for the MICROSCOPE space mission consists in two SAGE instruments. The first one (referred to as SUEP) is dedicated to the WEP test and contains test-masses of different composition (PtRh for the inner mass and TA6V for the outer one). The second instrument (referred to as SUREF) serves both as a calibration, to detect a potential bias in the measurement, and as a con-

firmation of the test precision. Both test-masses of the SUREF instrument are made with PtRh. A differential electrostatic accelerometer is composed of the three following units:

- **The Front-End Electronic Unit (FEEU)** contains the analogue electronics of the control loop and connects directly to the SU. It includes the capacitive sensors of both test-masses, the reference voltage sources, and the electronics generating the voltages applied to the surrounding electrodes.
- **The Sensor Unit (SU)**, composed by two concentric and coaxial cylindrical test-masses surrounded by four silica cores. The whole is disposed inside the same tight cage, as illustrated in Figure 2.3. In order to reduce the parasitic forces acting on the test-masses, such as radiometric forces or gas damping, a vacuum system maintains the pressure in the housing below 10^{-5} Pa.
- **The Interface Control Unit (ICU)** hosts the digital laws controlling the motion of both test-masses, and serves as the interface to the on-board computer.

The ICU receives the position measurement from the FEEU, computes the controls and sends them back to the FEEU. The FEEU then generates the required voltages to be applied to the SU electrodes. The components of both the SU and the FEEU require a steady thermal environment as well as a limited operating temperature range to ensure an optimal performance. The two Sensor Units and the two Front-End Electronic Units are thus gathered within a highly stabilized thermal environment referred to as the Payload Block (a passive thermal cocoon).

The two instruments can be separately switched on and off throughout the mission. Each electrostatic accelerometer has three operating modes:

- Stand-by mode: The Sensor Unit is switched off.
- Position sensing mode: The test-mass control does not operate in closed-loop. Therefore, only the test-mass position is measured.
- Acceleration sensing mode: The servo-control loop of the test-mass is closed. This last mode has two possible configurations: the full range mode (referred to as FR mode), offering a broader measurement range but a lower resolution, and the high resolution mode (referred to as HR mode), in which the resolution is higher, but the measurement range is narrower. During the WEP test sessions, the HR mode is used.

The configuration of the set of electrodes as well as the test-masses orientation with respect to the sensor unit are illustrated in Figure 2.4.

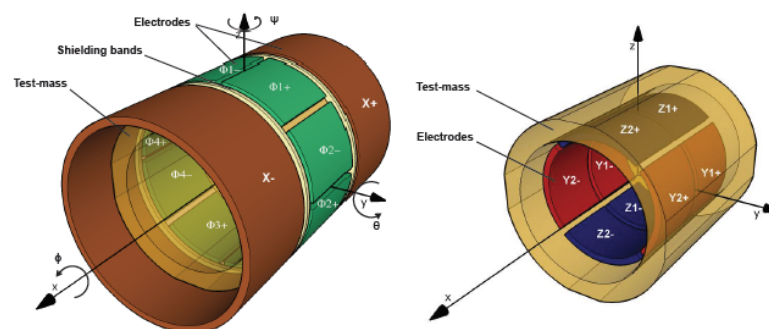


Figure 2.4: Electrode Configuration for the SAGE instrument. The test-mass is included (in yellow) in both diagrams. The X and ϕ control uses variations of the covering area, that is to say the area of the test-mass facing the electrodes. Radial control (Y, Z, θ and ψ) uses variations of the gap between the test-mass and the electrode [4].

The X-axis corresponds to the axial direction of the cylindrical test-mass, and provides the most sensitive measurements, which are used for the WEP test. The Z-axis is oriented along one of the radial directions of the test-mass and is in the orbital plane. The Y-axis orientation is chosen to form an orthogonal triad with the X, and Z axis. The Y-axis is therefore normal to the orbital plane, as illustrated in Figure 2.4. ϕ , θ and ψ respectively represent the rotation angles around the X, Y and Z axis. Both the axial and radial motion

of the test-mass are controlled by the surrounding electrodes, exerting electrostatic forces on it. The X and ϕ control is achieved through a change of capacitance caused by a variation of the surface of the test-mass facing the electrodes (referred to as variation of the covering area). The control in radial directions is achieved through the variations of the gap between the electrode and the test-mass (referred to as gap variation). The next subsection will thoroughly introduce the operating principle of the SAGE instruments, as well as the electrostatic detection and control of the test-masses.

2.2.2. Operating principle of the servo-controlled electrostatic accelerometer

Within the electrostatic accelerometer, the test-mass is levitated by means of electrostatic forces applied by the surrounding electrodes. A servo-controlled loop, based on the study of the electrostatic forces necessary to maintain the test-mass motionless at the center of the accelerometer cage allows the direct measurement of the acceleration. The control forces to be applied are inferred from the test-mass position measurement, through capacitive sensing.

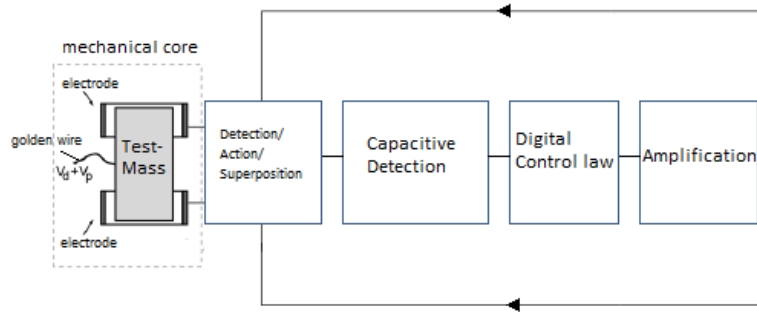


Figure 2.5: Test-mass control loop [18]

Every loop of the servo-controlled system contains both a detection step and an actuation step, as illustrated in Figure 2.5. First, a shift in the test-mass position is detected through capacitive sensing. The test-mass motion within the accelerometer cage indeed induces a capacity variation between the electrodes, which is then converted into an output voltage by the Capacitive Detection block. This output is used by the Digital Control Law block to compute the control signal, which is then amplified and applied to the surrounding electrodes to bring the test-mass back to its initial position, at the center of the cage. In the SAGE instruments, the same electrodes are used for both detection and action. In order to allow this control system to work properly, the test-mass potential V_m is controlled via a thin gold wire, which extends from one end of each mass to a pin on the facing end plate. This fragile yet essential wire, characterized by a thickness of $7\mu m$, represents the only physical contact between the masses and the rest of the sensor.

Detection of a test-mass displacement

A test-mass displacement along a given axis is measured by a pair of electrodes either facing or surrounding the test-mass as illustrated in Figure 2.4. Although the differential instrument for the MICROSCOPE mission requires cylindrical masses, with corresponding curved electrodes, this part will use a basic parallelepipedic form to present the accelerometer concept with basic equations. This simple form has been used for previous highly successful space instruments, such as the STAR for the CHAMP mission, and the SuperSTAR for the GRACE mission.

The control electrodes function in pairs in order to simultaneously measure and control the test-mass position, with the complete set providing the control in six degrees of freedom. Each electrode forms a capacitor with the surface of the test-mass facing it, whose capacitance will be denoted C_i . To enable the position detection, a sinusoidal reference voltage V_d , whose frequency is about 100kHz, is applied to the test-mass via a fine gold wire to generate currents across the capacitors. The detector output voltage is, in the end, proportional to the capacitances difference ($C_1 - C_2$):

$$V_{det} = G_{det}(C_1 - C_2) \quad (2.1)$$

Where V_{det} is the detector output voltage and G_{det} denotes the sensitivity gain of the capacitive sensor: $G_{det} = \frac{2V_d}{C_{eq}}$. V_d is the potential of the test-mass, and C_{eq} represents the sensor capacitance when the test-mass is located at the center of the cage (referred to as the mean capacitance).

For plane parallel surfaces separated by vacuum, the capacitance of the capacitor can be expressed by:

$$C_i = \frac{\epsilon_0 S_i}{e_i} \quad (2.2)$$

Where ϵ_0 is the dielectric permittivity of vacuum, S_i represents the area of the electrode i facing the test-mass, and e_i denotes the distance separating the electrode i and the test-mass. Assuming perfectly conducting surfaces under vacuum, the capacitance only depends on the configuration geometry. A test-mass displacement therefore results in a variation of the capacitance, either by changing the separation distance when the test-mass moves toward or away from the electrode (detection by gap variation), or by changing the covering surface area, when the test-mass moves parallel to the electrode surface (detection by variation of the covering area). Both detection techniques are detailed below.

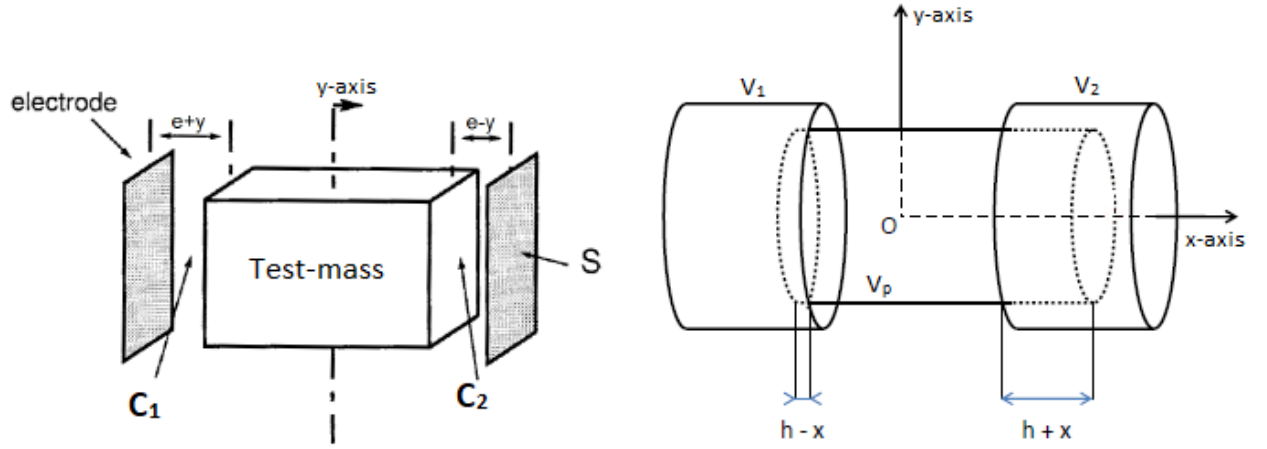


Figure 2.6: Variation of Capacitance due to mass displacement. (Left side) Gap variation. (Right side) Covering area variation [7].

2.2.2.1.1 Detection by gap variation: The detection by gap variation is used for a test-mass displacement in the Y and Z directions. Such a shift in the test-mass position would induce a variation of the distance e_i separating the electrode i and the test-mass, referred to as gap, as illustrated in Figure 2.6. For a displacement of the test-mass along the Y-axis, the gap of each capacitor can be expressed by:

$$e_i = \begin{cases} e - y & \text{if } i = 2 \\ e + y & \text{if } i = 1 \end{cases} \quad (2.3)$$

Where e denotes the distance separating the test-mass and the electrode, when the test-mass is located at the center of the accelerometer cage. If only small displacements around the equilibrium position are considered (that is to say if $y \ll e$), according to Equation 2.1, the detector output voltage can be written as:

$$V_{det} = G_{det} \epsilon_0 S \left(\frac{1}{e-y} - \frac{1}{e+y} \right) \approx \frac{2G_{det} \epsilon_0 S}{e^2} \cdot y + o\left(\left(\frac{y}{e}\right)^3\right) \quad (2.4)$$

The detector output voltage provided by the position sensor is therefore proportional to the test-mass displacement y . The gain depends both on the sensitivity of the sensor (with the term G_{det}), and on the instrument geometry (with the terms e and S). A good knowledge of these two parameters is therefore essential to precisely deduce the test-mass displacement.

2.2.2.1.2 Detection by variation of the covering area: An other detection method, based on the variation of the covering area S of the capacitance, is used to detect the displacement of the test-mass along the X-axis. We consider a cylindrical test-mass surrounded by a pair of concentric electrodes of similar shape, as

illustrated in [Figure 2.6](#). When the test-mass is at the center of the accelerometer cage, at position $x = 0$, each electrode covers the test-mass over a distance h . The area of the test-mass covered by the electrode i can be expressed by:

$$S_i = 2\pi r h_i \quad (2.5)$$

Where r represents the radius of the electrode i , and h_i denotes the covering distance:

$$h_i = \begin{cases} h - x & \text{if } i = 1 \\ h + x & \text{if } i = 2 \end{cases} \quad (2.6)$$

The detector output voltage is therefore equal to:

$$V_{det} = -\frac{G_{det}\epsilon_0 4\pi r}{e} \cdot x \quad (2.7)$$

Contrary to the expression of the output voltage for the detection by gap variation, the relation in [Equation 2.7](#) is exact and does not stem from a first order Taylor expansion. Consequently, in case of a detection by variation of the covering area, the output voltage is directly proportional to the test-mass displacement x .

Action to compensate for the displacement

The detector output voltage is digitized to be processed by the servo-control loop. The servo-control loop aims at nullifying the voltage V_{det} by applying an actuation voltage to the surrounding electrodes to compensate for the test-mass displacement and thus bring it back to its equilibrium position, at the center of the accelerometer cage.

Let us consider a single capacitor of capacitance C_i . It is assumed that the medium in-between is vacuum and that each plate carries a constant charge equal to $\pm Q$. The constant voltage V between the plates produces a force F_{el} undergone by the movable plate. According to the definition of the kinetic energy, an elementary displacement Δ of the movable plate leads to a work of the force F_{el} equal to:

$$dE_k = F_{el} \cdot \Delta \quad (2.8)$$

The potential energy stored in the electrode-mass capacitor is equal to:

$$E_p = \frac{1}{2} QV \quad (2.9)$$

Thanks to the definition of the capacitance $C_i = \frac{Q}{V}$, the relation previously derived can be rewritten as:

$$E_p = \frac{1}{2} C_i V^2 \quad (2.10)$$

And hence, the infinitesimal potential energy during dt is equal to:

$$dE_p = \frac{1}{2} V^2 dC_i \quad (2.11)$$

The infinitesimal power supplied by the generator during dt is equal to:

$$dE = V dQ = V^2 dC_i \quad (2.12)$$

Assuming no energy loss by Joule heating, the relation of energy conservation can be written as:

$$dE = dE_k + dE_p \quad (2.13)$$

This last relation means that the energy supplied by the generator is either stored in the capacitor, or turned into work. The [Equation 2.13](#) leads to:

$$V^2 dC_i = F_{el} \cdot du + \frac{1}{2} V^2 dC_i \quad (2.14)$$

The applied electrostatic force F_{el} can therefore be deduced and is equal to:

$$F_{el} = \frac{1}{2} V^2 \nabla C \quad (2.15)$$

Where V denotes the potential difference between the plates $V = V_i - V_p$. V_p , referred to as polarization, represents the constant potential at which the test-mass is maintained via the golden wire. V_i is the potential of the electrodes, which can be tuned by the servo-control loop. ∇C denotes the capacitance spatial gradient. According to Equation 2.15, a careful control of the potentials of both the test-mass and the electrodes enables to finely control the applied electrostatic force.

As for the detection of a test-mass displacement, the test-mass position control is achieved by two different techniques, respectively referred to as Gap control and Covering area control. Both control methods are described in the following.

2.2.2.2.1 Gap control This technique is used to control the test-mass motion along the Y and Z-axis (referred to as radial motion). As illustrated in Figure 2.7, the resulting force undergone by the test-mass is the sum of the electrostatic forces applied by the two electrodes. For a control along the Y-axis, the resulting force can be expressed as:

$$F_{el,y} = F_{el,1,y} + F_{el,2,y} = \frac{1}{2} \epsilon_0 S \left(-\frac{(V_1 - V_p)^2}{(e+y)^2} + \frac{(V_2 - V_p)^2}{(e-y)^2} \right) \quad (2.16)$$

Equal yet opposite control voltages are applied to the two electrodes of a pair: $V_1 = -V_e$ and $V_2 = V_e$. If only small test-mass displacements around the equilibrium position are considered (in other words, if $y \ll e$), a first order Taylor expansion leads to:

$$F_{el,y} = \frac{1}{2} \frac{\epsilon_0 S}{e^2} \left[-V_p V_e + (V_p^2 + V_e^2) \frac{y}{e} \right] + o\left(\left(\frac{y}{e}\right)^3\right) \quad (2.17)$$

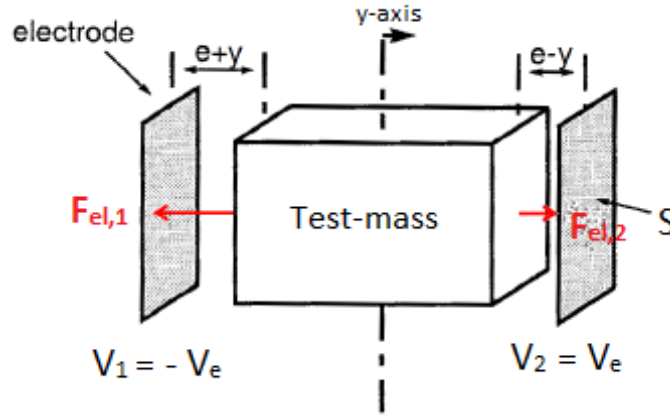


Figure 2.7: Test-mass control by gap variation. The electrostatic force is attractive, so the accelerometer electrodes act in pairs to provide both a positive and a negative force, but with a different magnitude. The resulting force tends to bring the test-mass at its equilibrium point, at the center of the cage [7].

This resulting applied force can be converted into an applied acceleration Γ_y , expressed in terms of both an actuation gain G_{act} and an electrostatic stiffness coefficient ω_p^2 :

$$\Gamma_y = \frac{F_{el,y}}{m_I} = -G_{act} V_e + \omega_p^2 \left[1 + \left(\frac{V_e}{V_p} \right)^2 \right] y \quad (2.18)$$

Where m_I is the inertial mass of the test-mass, and:

$$G_{act} = \frac{2\epsilon_0 S V_p}{m_I e^2} \quad \& \quad \text{and} \quad \omega_p^2 = \frac{2\epsilon_0 S V_p^2}{m_I e^3} \quad (2.19)$$

If only the first term of the right-hand side of the Equation 2.19 is considered, a good knowledge of the actuation gain G_{act} would be sufficient to derive the test-mass acceleration Γ_y from the applied voltage V_e . The measurement is nonetheless perturbed by the second term (proportional to ω_p^2) inducing a bias if the test-mass is not maintained at the center of the accelerometer cage ($y = 0$). However, it has been proved that the asymmetry included here as well as the displacement amplitude are small enough to neglect the second term with respect to the first one.

A similar technique is used for the angular control around the X-axis (Θ angle), but two pairs of electrodes are necessary to be able to induce a torque to the test-mass.

2.2.2.2 Covering area control This technique is used to control the test-mass motion along the X-axis (referred to as axial motion). As illustrated in Figure 2.8, the resulting force undergone by the test-mass can be expressed as:

$$F_{el,x} = F_{el,1,x} + F_{el,2,x} = \frac{2\pi r \epsilon_0}{e} \left[V_p(V_1 - V_2) + \frac{V_2^2 - V_1^2}{2} \right] \quad (2.20)$$

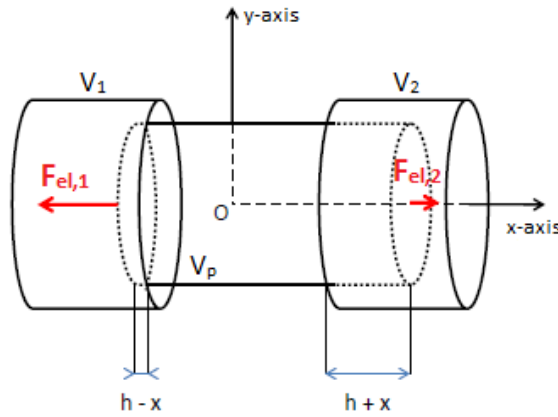


Figure 2.8: Test-mass control by variation of the covering area [7].

With equal yet opposite control voltages applied to the two electrodes of a pair: $V_1 = -V_e$ and $V_2 = V_e$, the applied acceleration can be expressed as:

$$\Gamma_x = -\frac{4\pi r \epsilon_0 V_p}{m_I e} V_e \quad (2.21)$$

In case of a control by variation of the covering area, the applied acceleration is therefore directly proportional to the electrodes potential. Contrary to the control by gap variation, the acceleration of the test-mass does not include any perturbation term proportional to the electrostatic stiffness. For this reason, the X-axis is referred to as the sensitive axis of the instrument, and is used for the WEP test.

Detection and Action Management

As mentioned in subsection 2.2.1, in a SAGE instrument, the same electrodes are used for both detection and action. This is achieved by using a different frequency for the detection potential V_d (production of a current across the capacitors), and the actuation potential V_p used to adjust the potential of the electrodes. Such a configuration allows the decoupling between the detection and the action processes. The value of the test-mass potential is therefore equal to $V_p + V_d$.

2.3. The measurement equation

This chapter has so far presented the operating process of the SAGE instruments. This subsection will now derive the physical equations modelling the in-orbit measurements provided by the instrument sensors. This

will be divided into, on the one hand, the derivation of the electrostatic acceleration applied to the test-mass, and on the other hand, the actual measured acceleration including the instrument defects and the other disturbances perturbing the estimation of the Eötvös parameter.

2.3.1. Derivation of the applied electrostatic acceleration

Let us consider a system defined by a test-mass i of a single inertial sensor. Its inertial mass is denoted m_i , its gravitational mass is denoted \tilde{m}_i , and its center of inertia is denoted O_i . This system undergoes the gravitational force $F_{g,i}$ (equal to $\tilde{m}_i g$), the electrostatic force $f_{e,i}$, as well as the sum of all other disrupting forces $f_{p,i}$. The gravitational acceleration g of a point of the test-mass includes the contribution of two main gravitational sources which are, on the one hand, the Earth, and on the other hand the microsatellite carrying the SAGE instrument. The effects of distant astrophysical sources, such as the Sun or the Moon, are negligible and their contribution is thus omitted in the following, leading to $g = g_{Earth} + g_{Satellite}$.

Let us now consider a system defined by the microsatellite. Its inertial mass, excluding the test-masses, is denoted M , its gravitational mass is denoted \tilde{M} and its center of inertia is denoted O_S . This system is subject to the gravitational force $F_{g,sat}$, the non-gravitational external forces F and the electrostatic forces from all the N test-masses.

Since the test-mass is not located at the satellite center of inertia O_S , some inertia terms are introduced. The study of these inertia terms requires the introduction of a satellite reference frame, fixed to the satellite platform and referred to as R_{sat} . The R_{sat} reference frame rotates with respect to the inertial reference frame R_{in} with an angular velocity $\Omega_{R_{sat}/R_{in}} = \Omega$. The composition of acceleration leads to:

$$\Gamma(O_i)|_{R_{in}} = \Gamma(O_S)|_{R_{in}} + \Omega \times (\Omega \times O_S O_i) + \dot{\Omega} \times O_S O_i + 2\Omega \times \left[\frac{dO_S O_i}{dt} \right]_{R_{sat}} + \left[\frac{d^2 O_S O_i}{dt^2} \right]_{R_{sat}} \quad (2.22)$$

In order to simplify the previous equation, the following notations are introduced:

$$O_S \dot{O}_i = \left[\frac{dO_S O_i}{dt} \right]_{R_{sat}} \quad \text{and} \quad O_S \ddot{O}_i = \left[\frac{d^2 O_S O_i}{dt^2} \right]_{R_{sat}} \quad (2.23)$$

The inertia gradient matrix $[In]$ as well as the angular velocity matrix $[\Omega]$ are introduced as well and defined as:

$$[\Omega] = \begin{pmatrix} 0 & -\Omega_z & \Omega_y \\ \Omega_z & 0 & -\Omega_x \\ -\Omega_y & \Omega_x & 0 \end{pmatrix} \quad (2.24)$$

Where Ω_x , Ω_y and Ω_z represent the components of the angular velocity vector Ω and:

$$[In] = [\Omega^2] + [\dot{\Omega}] \quad (2.25)$$

Finally, the Equation 2.22 giving the test-mass kinematic equation in the R_{sat} reference frame can be rewritten as:

$$\Gamma(O_i)|_{R_{in}} - \Gamma(O_S)|_{R_{in}} = [In]O_S O_i + 2[\Omega]O_S \dot{O}_i + O_S \ddot{O}_i \quad (2.26)$$

The Newton's second law therefore leads to:

$$[In]O_S O_i + 2\Omega O_S \dot{O}_i + O_S \ddot{O}_i = \frac{1}{m_i} f_{e,i} + \frac{1}{M} \sum_{j=1}^N f_{e,j} + \frac{1}{m_i} F_{g,i} - \frac{1}{M} F_{g,sat} + \frac{1}{m_i} f_{p,i} - \frac{1}{M} F \quad (2.27)$$

The parameters δ_i and δ_S are introduced:

$$\delta_i = \frac{\tilde{m}_i}{m_i} - 1 \quad \text{and} \quad \delta_S = \frac{\tilde{M}}{M} - 1 \quad (2.28)$$

While $[T](A)$ denotes the gravitational gradient computed at point A, and defined as the Jacobian matrix of the gravitational potential U. It can be written that:

$$\frac{1}{m_i} F_{g,i} - \frac{1}{M} F_{g,sat} \approx g_{S,i} + (\delta_i - \delta_S) g_E(A) + [T](A) \cdot [O_S O_i + (\delta_i A O_i - \delta_S A O_S)] \quad (2.29)$$

The order of magnitude of the gravitational gradient at a 700km altitude is about $10^{-6} s^{-2}$, and it has been stated in [chapter 1](#) that current on-ground EP experiments proved that $\delta < 10^{-12}$. The last term in parenthesis in the expression above leads to an acceleration error lower than $10^{-18} m \cdot s^{-2}$ (to be compared to the mission precision objective of $10^{-15} m \cdot s^{-2}$), and can therefore be neglected. The [Equation 2.27](#) can therefore be rewritten as:

$$[In]O_S O_i + 2\Omega O_S \dot{O}_i + O_S \ddot{O}_i = \frac{1}{m_i} f_{e,i} + \frac{1}{M} \sum_{j=1}^N f_{e,j} + g_{S,i} + (\delta_i - \delta_S) g_E(A) + [T](A) \cdot O_S O_i + \frac{1}{m_i} f_{p,i} - \frac{1}{M} F \quad (2.30)$$

In order to simplify the [Equation 2.30](#), the following parameters are introduced:

- The mechanical bias, defined as the sum of the mechanical perturbations on the test-masses and the microsatellite self-gravity: $b_i = -\frac{1}{m_i} f_{p,i} - g_{S,i}$.
- The vector joining the satellite center of inertia and the one of the test-mass, referred to as the off-centering vector: $\Delta_i = O_S O_i$
- The electrostatic acceleration applied to the test-mass i : $\Gamma_{App,i} = \frac{1}{m_i} f_{e,i}$

The [Equation 2.30](#) can thus be re-arranged as:

$$\left(1 + \frac{m_i}{M}\right) \Gamma_{App,i} = -[T](A) \cdot \Delta_i - (\delta_i - \delta_S) g_E(A) + [In] \Delta_i + 2[\Omega] \dot{\Delta}_i + \ddot{\Delta}_i + b_i + \frac{1}{M} F - \sum_{j \neq i}^N \frac{m_j}{M} \Gamma_{App,j} \quad (2.31)$$

The MICROSCOPE space mission objective consists in studying the difference between the acceleration undergone by the two test-masses. It is therefore useful to introduce a parameter defined as the half difference of the accelerations applied to the two test-masses of one SU and referred to as the differential acceleration:

$$\Gamma_{App,d} = \frac{1}{2} (\Gamma_{App,1} - \Gamma_{App,2}) \quad (2.32)$$

Where index 1 refers to the internal test-mass and index 2 refers to the external test-mass of the SU. The common acceleration, defined as the half-mean of the applied accelerations, is also introduced:

$$\Gamma_{App,c} = \frac{1}{2} (\Gamma_{App,1} + \Gamma_{App,2}) \quad (2.33)$$

More generally, the common and differential modes are defined for any quantity y_i as:

$$y_c = \frac{1}{2} (y_1 + y_2) \quad (2.34)$$

$$y_d = \frac{1}{2} (y_1 - y_2) \quad (2.35)$$

The expressions for both the differential and common acceleration can therefore be derived:

$$\begin{aligned} \Gamma_{App,c} &= \frac{1}{1 + \alpha_c} \left\{ -([T] - [In]) \cdot (\Delta_c - \alpha_d \Delta_d) - (\delta_c - \alpha_d \delta_d) g_E \right. \\ &\quad + \delta_S g_E + 2[\Omega] (\dot{\Delta}_c - \alpha_d \dot{\Delta}_d) + \ddot{\Delta}_c - \alpha_d \ddot{\Delta}_d \\ &\quad \left. + b_c - \alpha_d b_d + \frac{1}{M} F - \sum_{j \neq 1,2}^N \frac{m_j}{M} \Gamma_{App,j} \right\} \\ &\approx -([T] - [In]) \cdot \Delta_c - (\delta_c - \delta_S) g_E + 2[\Omega] \dot{\Delta}_c + \ddot{\Delta}_c + b_c + \frac{1}{M} F - \sum_{j \neq 1,2}^N \frac{m_j}{M} \Gamma_{App,j} \end{aligned} \quad (2.36)$$

and

$$\Gamma_{App,d} = -([T] - [In]) \cdot \Delta_d - \delta_d g_E + 2[\Omega] \dot{\Delta}_d + \ddot{\Delta}_d + b_d \quad (2.37)$$

Where $\alpha_c = \frac{m_1 + m_2}{M}$, $\alpha_d = \frac{m_1 - m_2}{M}$ and δ_d denotes the differential WEP parameter, approximately equal to half the Eötvös parameter. Since $m_j \ll M$, the ratios α_c and α_d are small with respect to 1. It can be observed that, contrary to the expression of the common acceleration, the expression of the differential acceleration does not depend on the non-gravitational external forces F , nor on the reaction of the microsatellite to the electrostatic accelerations applied to the other test-masses.

2.3.2. Instrument imperfections

The subsection 2.3.1 derived the equation of the applied electrostatic acceleration. Nonetheless, in practice, the measurement provided by the accelerometer inertial sensor is not rigorously equal to $\Gamma_{App,i}$. The measured acceleration is derived from the correction voltage applied to the electrodes, and is therefore subject to slight defects throughout the measurement process. These defects can be divided into, on the one hand, the systematic errors (including axis couplings and misalignment, non linearity and scaling differences), and the stochastic errors (including electronic noise, thermal fluctuations and stochastic variations of the forces applied to the masses).

Deterministic errors

The systematic instrumental errors are listed and formalized below.

- The coupling between axes, resulting from the non-exact orthogonality of the sensors measurement axes and modelled by the symmetric matrix $[\eta_i]$:

$$[\eta_i] = \begin{pmatrix} 0 & \eta_{zi} & \eta_{yi} \\ \eta_{zi} & 0 & \eta_{xi} \\ \eta_{yi} & \eta_{xi} & 0 \end{pmatrix}$$

These couplings will be thoroughly investigated in the next chapter.

- The measurement scale factors, depending on the instrument geometry (surface of the electrode, equilibrium gap and mass of the test-mass) and modelled by the diagonal matrix $[K_{1i}]$:

$$[K_{1i}] = \begin{pmatrix} K_{1xi} & 0 & 0 \\ 0 & K_{1yi} & 0 \\ 0 & 0 & K_{1zi} \end{pmatrix}$$

The measurement scale factors can depend on the temperature, but their thermal sensitivities are assumed to be negligible.

- The small misalignments and rotations between the satellite reference frame, and the test-mass reference frame, modelled by the antisymmetric rotation matrix $[\Theta_i]$:

$$[\Theta_i] = \begin{pmatrix} 1 & \Theta_{zi} & -\Theta_{yi} \\ -\Theta_{zi} & 1 & \Theta_{xi} \\ \Theta_{yi} & -\Theta_{xi} & 1 \end{pmatrix}$$

- The coupling of the linear acceleration with the angular acceleration, resulting from the slight perturbations caused by the angular control on the linear control, and modelled by the coupling matrix $[C_i]$.
- The electrical bias, including all the parasitic constant terms, and denoted b_{0i} . The bias depends on the temperature. This will be investigated more in-depth in [chapter 4](#).
- The quadratic term Q_i , modelling the non-linearities, and proportional to the squared components of the applied acceleration: $Q_i = K_{2i} \circ [\Theta_i] \Gamma_{App,i}^2$, where \circ denotes the operator multiplying two arrays element by element, and K_{2i} represents the 3-components quadratic coefficient vector:

$$[K_{2i}] = (K_{2ixx} \quad K_{2iyy} \quad K_{2izz})$$

The scale factors $[K_{1i}]$, the coupling between axes $[\eta_i]$, as well as the slight misalignments $[\Theta_i]$ are gathered in the sensitivity matrix $[A_i]$ defined as:

$$[A_i] = ([K_{1i}] + [\eta_i]) \cdot [\Theta_i] \approx \begin{pmatrix} K_{1xi} & \eta_{zi} + \Theta_{zi} & \eta_{yi} - \Theta_{yi} \\ \eta_{zi} - \Theta_{zi} & K_{1yi} & \eta_{xi} + \Theta_{xi} \\ \eta_{yi} + \Theta_{yi} & \eta_{xi} - \Theta_{xi} & K_{1zi} \end{pmatrix}$$

Because $\eta_{ki} \ll 1$, and $\Theta_{ki} \ll 1$, where $k \in (x, y, z)$. The symmetric part of the sensitivity matrix corresponds to the coupling between axes, while its antisymmetric part corresponds to the misalignments and small rotations. The diagonal of $[A_i]$ includes the scale factors.

Noise

As previously mentioned, the measurement process is perturbed by some random disturbances referred to as stochastic noise. The instrumental stochastic noise, denoted by a variable n_i , is characterized by its power spectral density (PSD) expressed, for a quantity expressed in a unit U, in $U^2 \cdot \text{Hz}^{-1}$. If the PSD depends on the frequency, the noise is said "coloured", otherwise, the noise is said "white". The main contributions of the instrument stochastic noise are:

- **The electronic noise** coming from the capacitive detectors, whose contribution is low at the WEP test frequency, but predominant at high frequency.
- **The thermal acceleration noise**, which can be divided into, on the one hand, the radiometric noise (resulting from the momentum exchange between the particles in the accelerometer cage and the test-mass), and on the other hand, the noise originating from the thermal radiation of the test-mass environment and referred to as radiation pressure.
- **The noise resulting from both the stiffness and the damping of the gold wire used to maintain the test-mass at a constant potential.** The damping noise is the principal contributor to the measurement uncertainty at the WEP test frequency.

Other sources of noise, such as the fluctuations of the magnetic field, are also included in the instrumental stochastic noise, but will not be detailed here. The total acceleration noise, for a test-mass i , is obtained by summing all contributions. Assuming that all noise sources are independent, the PSDs can be summed as well, resulting in the PSD noise model illustrated in Figure 2.9.

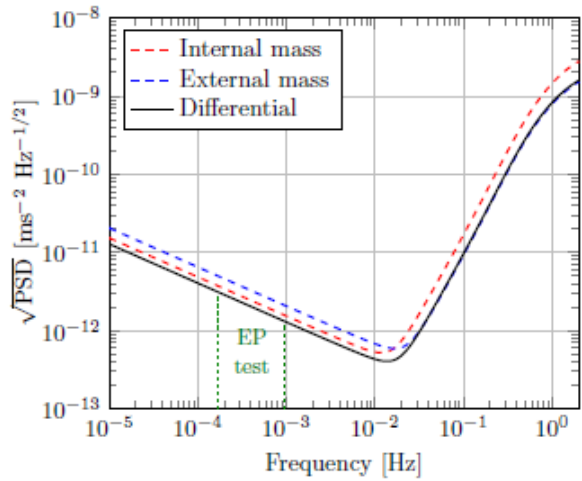


Figure 2.9: PSD noise model on the X-axis considering all noise sources [7].

When the satellite is in Spin mode, the WEP test frequency increases, resulting, according to Figure 2.9, in a reduction of the instrumental noise. It can also be inferred from Figure 2.9 that a rotation rate higher than the one selected for the Spin mode configuration would lead to a better noise reduction. Nonetheless, such a choice would have drastically reduced the duration of the space mission. The rotation rate of the satellite has thus been selected as a trade-off between the reduction of the noise and the mission lifetime.

The test uncertainty being inversely proportional to the integration time [7], the instrument stochastic noise can be reduced down to a desired level by integrating numerous data points over a sufficient long period of time. In order to be compatible with the mission precision objective of 10^{-15} , the WEP test sessions for the inertial and the spin mode have to last respectively 120 orbits and 20 orbits.

2.3.3. Derivation of the measured electrostatic acceleration

According to the previous parts, the acceleration measurement $\Gamma_{mes,i}$ affected by all the systematic and stochastic errors can be defined as:

$$\Gamma_{mes,i} = b_{0i} + [A_i]\Gamma_{App,i} + Q_i + [C_i]\dot{\Omega}_i + n_i \quad (2.38)$$

Where $\Gamma_{App,i}$ is the electrostatic acceleration applied to the test-mass. The Equation 2.34 allows to derive the expressions for both the common and differential measured accelerations:

$$\Gamma_{meas,c} = b_{0c} + [A_c]\Gamma_{App,c} + [A_d]\Gamma_{App,d} + Q_c + n_c \quad (2.39)$$

$$\Gamma_{meas,d} = b_{0d} + [A_c]\Gamma_{App,d} + [A_d]\Gamma_{App,c} + Q_d + n_d \quad (2.40)$$

To lighten the two relations above, the couplings of the linear acceleration with the angular acceleration modelled by the coupling matrix $[C]$ were omitted. They will be included again if needed in the next developments.

The objective of the MICROSCOPE experiment is to evaluate the parameter δ_d , corresponding to the amplitude of a potential WEP violation signal. In order to reach this goal, the measurement equation previously derived must be decomposed into a signal of interest (including the parameter δ_d), and a sum of perturbing signals that can be measured, modelled, or controlled to remain at a value compatible with the mission precision objective. These perturbations are then characterized and removed to reduce the error on the WEP violation signal.

To decompose the measurement equation as required, the following variables are introduced:

$$[A'_c] = [A_c][\Theta_c]^{-1}, [A'_d] = [A_d][\Theta_c]^{-1}$$

$$[\bar{A}_d] = [A'_d][A'_c]^{-1}, [\bar{A}_c] = [A_c] - [\bar{A}_d][A_d]$$

and

$$\bar{Q}_d = Q_d - [\bar{A}_d]Q_c$$

By substituting Equation 2.36 into Equation 2.39, the measured differential acceleration can be expressed as:

$$\begin{aligned} \Gamma_{meas,d} = & b_{0d} + [\bar{A}_c]\Gamma_{App,d} (-([T] - [In]) \cdot \Delta_d - \delta_d g_E + 2[\Omega]\dot{\Delta}_d\ddot{\Delta}_d + b_d) \\ & + [\bar{A}_d](\Gamma_{meas,c} - b_{0c} - n_c) + \bar{Q}_d + n_d \end{aligned} \quad (2.41)$$

The right-hand side terms of the previous equation can be either measured, modelled, or controlled to remain at an acceptable level. For instance, although the term $(\Gamma_{meas,c} - b_{0c} - n_c)$ cannot be directly measured, it is nonetheless maintained to the lowest possible value thanks to the AOCS loop that controls the common acceleration to be equal to $b_{0c} + n_c$. Some of the terms of the measurement equation are multiplied by unknown matrices ($[\bar{A}_c]$ for example). The several in-orbit calibration sessions aim at evaluating the unknown coefficients of these matrices, to be able to correct the measured differential acceleration for the corresponding perturbations, and thus to isolate the WEP violation signal $\delta_d g_E$.

The coefficients of the $[\bar{A}_d]$ and $[\bar{A}_c]$ matrices are respectively denoted:

$$[\bar{A}_d](i, j) = a_{dij} \text{ and } [\bar{A}_c] = a_{cij}$$

Then, the measured differential acceleration along the X-axis (referred to as the sensitive axis), can be expressed as a linear combination of calibration parameters, defined as known time variations $p_i(t)$ with unknown amplitudes β_i :

$$\Gamma_{meas,dx} = -a_{c11}\delta_d g_{E,x} + \sum_{i=1}^{N_p} \beta_i p_i(t) + n_d(t) \quad (2.42)$$

If the various disturbances are not rejected from the measured differential equation, they may induce a bias in the estimation of the parameter δ_d . Therefore, all the perturbations must be accurately evaluated to correct the acceleration measurements for the disturbing signals and thus reduce the systematic errors to a level compatible with the mission precision objective.

2.3.4. Estimation of the WEP violation parameter

The estimation of both the instrument calibration parameters and the WEP violation parameter δ relies on the general form of Equation 2.42:

$$\Gamma_{meas,corr,dx}(t) = \frac{1}{2}\delta g_x(t) + \sum_{i=1}^{N_p} \beta_i p_i(t) + n_{dx}(t) \quad (2.43)$$

The whole estimation process begins by the obtention of estimates $\hat{\beta}_i$ for the instrument defects β_i . This is achieved by fitting the measured or modelled signals p_i to the differential acceleration or other variables measured during dedicated in-flight calibration phases (See subsection 3.2.1). The error made in the estimation of the instrument defects will directly affect the error made on the WEP violation parameter estimation. Once the instrument parameters separately estimated, the differential acceleration of a WEP test session is computed and corrected by removing $\sum_{i=1}^{N_p} \hat{\beta}_i p_i(t)$ from the signal. The corrected acceleration obtained can be expressed as:

$$\Gamma_{meas,dx}(t) = \frac{1}{2}\delta g_x(t) + \sum_{i=1}^{N_p} (\beta_i - \hat{\beta}_i) p_i(t) + n_{dx}(t) \quad (2.44)$$

The WEP violation parameter is then evaluated by fitting the gravitational acceleration g_x to the corrected differential acceleration $\Gamma_{meas,corr,dx}$ by means of an ordinary least-squares regression:

$$\hat{\delta} = 2(g_x^T g_x)^{-1} g_x^T \Gamma_{meas,corr,dx} \quad (2.45)$$

The error made in the estimation of the instrument parameter i , denoted ϵ_i and defined as $\epsilon_i = \beta_i - \hat{\beta}_i$, depends on both the variance and the bias of the estimation. The upper bound of each ϵ_i , denoted $\bar{\epsilon}_i$, can be evaluated by a thorough analysis of the different disturbance terms involved in each in-orbit calibration phase. Then, an estimation of the maximal residual bias in the measurement can be obtained by summing the bias resulting from all the residual perturbing signals:

$$\bar{b}_\delta = 2 \sum_{i=1}^{N_p} [(g_x^T g_x)^{-1} g_x^T p_i \bar{\epsilon}_i] \quad (2.46)$$

Another contribution to the estimation error is the stochastic noise, characterized by its power spectral density (denoted PSD). The covariance of the matrix $\hat{\beta}$, defined as the one-dimensional matrix gathering the estimates of the instrument parameters, thus depends on the PSD of the instrument stochastic noise.

2.3.5. Other perturbations in the measurement

The range of data processing techniques developed in the previous sections was based on the hypothesis of a regular sampling of the measurements. Nonetheless, the ordinary least-squares estimator may be imprecise in case of a lack of several data points in the time series recorded by the instrument. In practice, some data loss may occur in the measurements, involving a modification of the projection rate, and thus an impact on the precision of the WEP violation parameter estimation. The absence or invalidity of some data (both referred to as "missing data") in the measurements can result from various physical or operational phenomena, such as telemetry losses due to errors occurred in the down-link transmission (the recovery rate remains satisfactory during transmission losses because the data remains stored in the satellite during 9 hours and thus can be downloaded again), or instrument saturation events resulting from cracks in the multilayer insulation coating, cracks in the cold gas tanks of the thrusters, and impacts with micrometeorites (because of the limited measurement range of the accelerometer, the acceleration peaks induced by the events previously mentioned can exceed the saturation threshold and thus lead to either corrupted or missing data). Missing data in the measurement leads to an increase of uncertainty because of the spectral leakage. As illustrated in Figure 2.10, the OLS uncertainty rapidly increases with the number of gaps per orbit. This phenomenon being incompatible with the MICROSCOPE mission precision objective of 10^{-15} on the Eötvös parameter, an other estimation technique is needed.

Some robust and reliable data processing techniques dedicated to deal with data gaps in the measurement have thus been developed ([18], [7]). This is the case for the general autoregressive least-squares estimator

with missing data referred to as the KARMA method [7]. The KARMA estimator allows to maintain a precision close to 10^{-15} despite the data gaps in the measurements. In order to reduce the uncertainty of the WEP test in case of missing data, a PSD estimation technique referred to as *Inpainting* has been developed, allowing an estimation of the square-root PSD with an error lower than $10^{-12} m s^{-2} / \sqrt{Hz}$ around f_{EP} , while providing faithful reconstructed data sets. The KARMA method is only mentioned and will not be thoroughly developed here.

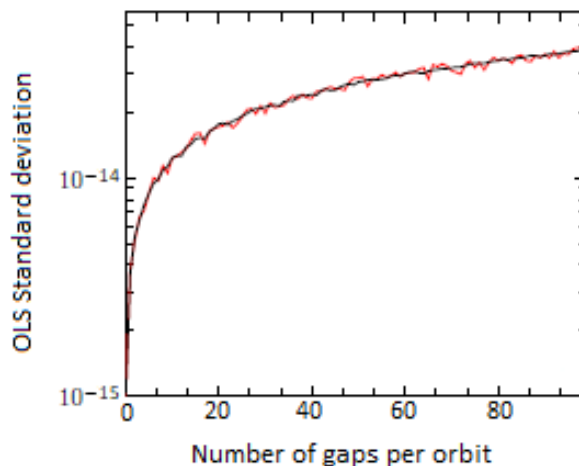


Figure 2.10: OLS uncertainty with respect to the number of gaps per orbit. [7]

This chapter carefully introduced the MICROSCOPE experiment, based on the use of two differential electrostatic accelerometers referred to as SAGE instruments. The measurements provided by each accelerometer are derived from the control voltage applied to the electrodes in order to maintain the test-masses relatively motionless at the center of the cage. The thorough instrument description has led to the derivation of the measurement equation, taking into account the several perturbations occurring throughout the measurement process and thus limiting the measurement precision. The amplitudes of these disturbing signals, depending both on the instrument characteristics and defects, may induce a bias in the measurement of a possible WEP violation and must therefore be carefully estimated. The first results of the MICROSCOPE experiment released on December 2017 [29], and based on 120 orbits among the 1900 realized by the satellite so far, allowed to reach a precision ten times higher than the current ground-based WEP tests on the WEP parameter: $\delta(\mathbf{T}_i, \mathbf{P}_t) = [-1 \pm 9(\text{stochastic}) \pm 9(\text{systematic})] \cdot 10^{-15}$ for the SUEP instrument. The test performed with the SUREF instrument and based on 62 orbits led to: $\delta(\mathbf{P}_t, \mathbf{P}_t) = [+4 \pm 4(\text{systematic})] \cdot 10^{-15}$. Nonetheless, the instrumental model implemented to process the data used conservative upper limits for some systematic errors, such as the coupling defects and the thermal sensitivity. The research work developed in the following chapters will be dedicated to the design of more accurate models for both the coupling factors and the thermal sensitivity, in order to improve the mission performance. The fundamental properties and equations presented throughout this chapter will be of great interest in the upcoming work, and will thus be put into practice in the coming chapters.

Chapter 3

Coupling between axes

Contents

3.1 Definition of the coupling between axes	25
3.2 Exploitation of the in-orbit calibration sessions	25
3.2.1 Overview of the calibration sessions.	25
3.2.2 Presentation of the instrumental model	26
3.2.3 Processing of the calibration sessions in the investigation of the coupling factors:	31
3.3 Exploitation of a new type of mission phase	38
3.4 Design of an instrument simulator	43

The [chapter 2](#) thoroughly presented the MICROSCOPE experiment and introduced the slight defects perturbing the measurement process. In an attempt to improve the model used for some perturbations, this chapter will now investigate the ways to carefully estimate the coupling between axes.

3.1. Definition of the coupling between axes

Coupling refers to the interactions between the six axes of the instrument (3 translations X, Y, Z , and the 3 corresponding rotations ϕ, θ and ψ around the linear axes). Ideally, the six axes would be completely independent, but the imperfections of the SAGE instrument discussed in the previous chapter does not allow this. The coupling perturbs the measurement by creating a bias: the detector sees a non-zero position and thus offsets the test-mass to compensate for the false position reading. With the six axes functioning simultaneously, coupling from one axis will cause the control voltage on a second axis to react, which, in turn, creates a coupling effect to a third axis. The required characterization is the behavior of the six axes of the instrument in response to an external acceleration. The effects of an acceleration along one axis can be recorded in the acceleration measurements of each axis. After applying a well known acceleration on multiple axes, the data can be analyzed simultaneously to identify the coupling coefficients between each axis. To perform the measurement, a sinusoid of a specific frequency needs to be applied in the instrument loop to force an oscillation of the test-mass. Such a process is applied during the in-orbit calibration sessions, that will be discussed in the next section.

3.2. Exploitation of the in-orbit calibration sessions

3.2.1. Overview of the calibration sessions

As previously mentioned in [chapter 2](#), in order to estimate the WEP violation parameter δ with a precision objective of 10^{-15} , one should be able to extract from the measurement a signal of amplitude $\frac{1}{2} g_x(f_{EP}) \cdot \delta = 4 \cdot 10^{-15} m \cdot s^{-2}$. The disturbing terms exposed in the measurement equation derived in [subsection 2.3.3](#) are related to perturbations in the test-masses motion (parasitic electrostatic forces), to the AOCS performance,

and to the instrument characteristics. All these perturbing terms need to be precisely evaluated during dedicated calibration sessions. The calibration of the several parameters have been achieved in orbit in order to be freed from all on-ground perturbation sources (such as, for example, the thermal perturbations induced by human activity), and therefore to reach a satisfactory precision.

Therefore, specific mission phases have been designed in order to precisely evaluate the various disturbing parameters. The calibration principle for the MICROSCOPE instrument consists in exciting the satellite and the instrument in various ways to generate an acceleration signal amplifying the effect of the instrument parameter that needs to be estimated, and making it preponderant in the measurement. Contrary to the space missions using electrostatic accelerometers but not having access to a continuous Orbit Control System, such as CHAMP and GRACE [30], the MICROSCOPE calibration sessions can exploit the satellite drag compensating system. The calibration signal is therefore obtained by applying either a linear or angular oscillating movement to the satellite through the drag compensating system [15]. Contrary to the frequency of the oscillating movement imparted to the satellite, the amplitude of the motion does not need to be precisely known, since it is measured by the accelerometer. It is also possible to use for the calibration a naturally occurring signal with a high amplitude at a given frequency, such as the gravitational gradient T at twice the orbital frequency (the gravitational gradient is determined from a very precise model). The total calibration duration is 138 orbits, that is to say about 9 days. A range of specific processes dedicated to the estimation of each of the instrument parameters has therefore been developed. The calibration performance depends on the performance of the AOCS.

Among the various types of calibration sessions, the ones that can be relevantly quoted are gathered below:

- *The K_{1dx} calibration sessions:* These sessions have been designed to evaluate the differential measurement scale factor K_{1dx} introduced in subsection 2.3.2. As seen in the measurement equation derived in the previous chapter, the effect of K_{1dx} can be amplified by adding an extra command to the drag compensating control block. To perform the measurement, a sinusoid of a specific frequency f_{callin} is applied in the instrument control loop in order to force an oscillation of the test-mass position along the X-axis. The excitation signal $E(t)$ has an amplitude of $5 \cdot 10^{-8} m \cdot s^{-2}$, and a frequency of $1.23 \cdot 10^{-3} Hz$:

$$E_X(t) = (5 \cdot 10^{-8}) \cdot \sin(2\pi(1.23 \cdot 10^{-3})t)$$

- *The Θ_{dy} and Θ_{dz} calibration sessions:* These sessions have been designed to evaluate the differential misalignments Θ_{dy} and Θ_{dz} between the satellite reference frame and the test-mass reference frame introduced in subsection 2.3.2. As for the estimation of the differential measurement scale factor K_{1dx} , the effect of each parameter can be amplified by adding an extra command to the drag compensating control block. To perform the measurement, a sinusoid of frequency f_{callin} (same frequency as the one used for the K_{1dx} calibration sessions) is applied in the instrument control loop in order to force an oscillation of the test-mass position. The satellite oscillates along the Y-axis, for the estimation of Θ_{dz} , and along the Z-axis, for the estimation of Θ_{dy} . For both types of calibration session, the excitation signal $E(t)$ has an amplitude of $5 \cdot 10^{-8} m \cdot s^{-2}$, and a frequency of $1.23 \cdot 10^{-3} Hz$:

$$E_Y(t) = E_Z(t) = (5 \cdot 10^{-8}) \cdot \sin(2\pi(1.23 \cdot 10^{-3})t)$$

These various types of calibration sessions have been achieved for both the accelerometers SUEP and SUREF described in section 2.2. For each calibration scenario, the drag compensating system can be set to compensate either the motion of the internal test-mass, or the motion of the external test-mass. Each calibration scenario has been repeated several times throughout the mission in order to take into account the variations of the instrument parameters over time. Therefore, in order to differentiate among the numerous phases, each calibration session bears an unique identifying number. The next subsections will present how these calibration sessions can be used in order to estimate the instrument coupling factors.

3.2.2. Presentation of the instrumental model

Some of the calibration sessions can be used to investigate the coupling between axes. As mentioned in the previous subsection, the calibration principle consists in exciting the satellite with a known signal to amplify

the effect of the instrument parameter that needs to be estimated, and thus make it preponderant in the measurement. During some of the calibration sessions, an oscillation of the test-mass position along one axis of the instrument is forced through the Attitude and Orbit Control System. The careful study of the test-mass acceleration along the other axes can give valuable information about the coupling between axes.

Throughout this part, the coupling factors investigation process will be illustrated with the K_{1dx} calibration sessions. The same process will nonetheless also be applied to the Θ_{dy} and Θ_{dz} calibration sessions. The computations derived next will thus consider a mission phase in which an oscillation of the test-mass position along the X-direction is forced by the drag compensating control block.

Each functioning instrument model has a corresponding computer simulation, created with *Simulink*. These simulations have been used to define the control laws and confirm that the complete instrument loop is sufficient for both the initial acquisition and the stable control. The definitive instrument model will be a non-linear simulation treating each electrode separately, and including interactions between the instrument axes. However, this will be achieved in steps, starting with a simple linearized model to illustrate the principle of the calibration sessions. The instrument model used to illustrate the calibration scenario must be sufficiently simple to be easily interpreted, but also sufficiently detailed to provide an accurate representation of the instrument working principle. A simplified linear instrument model in which the electrical bias and the instrumental noise (introduced in subsection 2.3.2) are neglected is therefore used. The control in the X-direction is represented on Figure 3.1. In this illustration, the drag-compensating system is set to compensate the motion of the external test-mass, referred to as *IS2*. The internal test-mass is referred to as *IS1*.

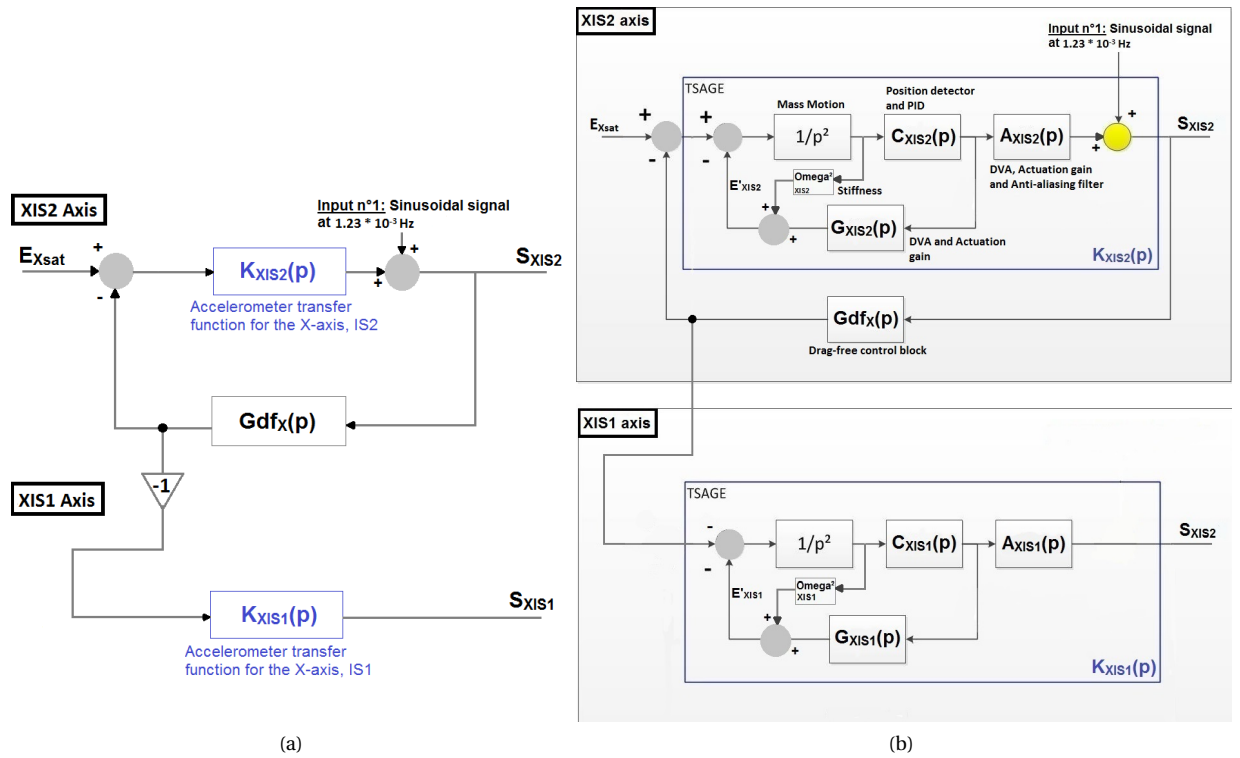


Figure 3.1: (a) Illustration of the instrument loop along the X-axis, for a K_{1dx} calibration session. The axes labelled *IS1* refer to the internal test-mass axes and those labelled *IS2* refer to the external test-mass axes. (b) Another illustration of the instrument loop along the X-axis, for a K_{1dx} calibration session, with a detailed representation of the accelerometer control laws.

E_{Xsat} denotes the external acceleration along the X-axis. In the mission phases investigated, it is assumed that:

$$E_{Xsat} \approx 0$$

S_{XIS2} and S_{XIS1} respectively represent the measured acceleration for the external and internal test-masses along the X-direction. G_{df} denotes the drag-compensating control block. $K_{XIS2}(p)$ and $K_{XIS1}(p)$ respectively denote the accelerometer transfer function along the X-direction for the external and internal test-mass. The Laplace variable p is equal to: $p = i\omega = i2\pi f$; ω is the measurement frequency, which is the frequency of the sinusoid input.

The working principle of each block is detailed below:

- **The $1/p^2$ block:** The proof-mass motion is modelled by the double integration of the acceleration applied to the mass. This block also includes rebound conditions if the mass hits the stop. However, with a stable control, this will not happen.
- **The $C_{XIS2}(p)$ block:** This block illustrates the working principle of both the position detector and the Proportional-Integral-Differential controller (referred to as PID). The mass position produced by the $1/p^2$ block is then measured by the position detector block, with a conversion from a position to a voltage. A transfer function represents the measured cut-off frequency of the detector. The output of the detector block is limited to the 15V saturation of the electronic circuit. The PID controller, illustrated in Figure 3.2, has been selected for its relative simplicity and robustness. The proportional term controls the bandwidth of the loop. The integral term provides an output proportional to the integral of the error. The differential term can reduce the overshoot of the response, but also introduces a damping factor. The PID performance objectives must meet the requirements for both the EP test, and the AOCS. In order to reach the precision objective of the EP test, a high gain is desired at low frequencies to minimize the test-mass motion. Nonetheless, since micrometeorite impacts are possible within the orbital environment, the accelerometer must also be able to support sudden shocks without the mass hitting the stops. The PID controller parameters have been calculated from the electronic components used, for a close match between the model and the actual instrument. Each axis of each mass of each instrument has its own well tuned PID.

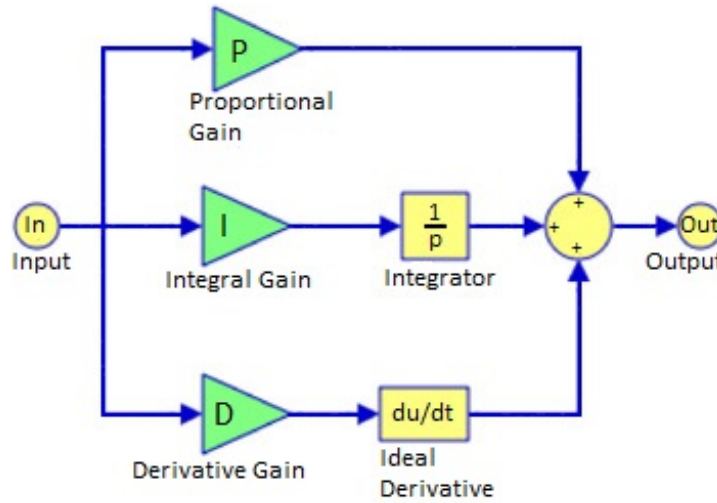


Figure 3.2: General form of a Proportional-Integral-Differential controller

The general expression of the $C(p)$ block control function, for each sensor, is detailed in the relation below:

$$C(p) = \left[\frac{G_{det}G_{fm}}{1 + \frac{p}{2\pi F_{CutOffDet}}} \right] \left[\frac{K_p}{1 + \frac{\sqrt{2}}{2\pi F_{pre}} p + \left(\frac{p}{2\pi F_{pre}}\right)^2} \right] \left[\frac{\frac{p}{2\pi F_{D1}}}{\left(1 + \frac{p}{2\pi F_{D2}}\right) \cdot \left(1 + \frac{p}{2\pi F_C}\right)} + \frac{F_{D1} + F_I}{F_{D1}} + \frac{2\pi F_I}{p} \right] \left[\frac{1}{1 + \frac{p}{2\pi F_{post}}} \right] \quad (3.1)$$

- **The $G_{XIS2}(p)$ and $A_{XIS2}(p)$ blocks:** The PID output is then amplified by the Digital Voltage Amplifier block (referred to as DVA) which consists of a measured gain, a transfer function representing the measured cut-off frequency and a saturation level corresponding to the high voltage supply. The output of the DVA corresponds to the voltage applied to the positive electrode of each pair. The actuation gain converts the

DVA output to an acceleration of the mass due to the control voltage on the electrodes. Unlike the $G_{XIS2}(p)$ block, the $A_{XIS2}(p)$ block also includes an anti-aliasing filter, which is a 5th order Butterworth low-pass filter (see [Appendix A](#) for the detailed expression of the filter transfer function $H_{Butterworth}(p)$), to restrict the bandwidth of the signal and therefore satisfy the sampling theorem. The general expressions of both the $G(p)$ and $A(p)$ block control functions, for each sensor, are detailed below:

$$G(p) = \frac{G_{DVA}}{1 + \frac{p}{2\pi F_{CutOffDVA}}} \cdot G_{actuation} \quad (3.2)$$

and

$$A(p) = G_{DVA} \cdot G_{actuation} \cdot H_{Butterworth}(p) \quad (3.3)$$

- **The ω_p^2 stiffness block:** The sensor stiffness is the component of the electrostatic force proportional to the offset of the test-mass from the center of the electrode pair applying the force. The stiffness is provided as a gain ω_p^2 . A positive sign of the stiffness indicates a destabilizing effect, since the acceleration created by the stiffness has the same sign as the position offset. The stiffness has a constant part, which could be due to a defect in the cylindricity of the test-mass or electrode cylinders, and a frequency dependant part, most likely due to a mechanical effect. The stiffness of all sensors have been accurately evaluated in-flight, with dedicated mission phases during which a sinusoid with a specific frequency was applied to the PID external input to force an oscillation of the mass position: the ratio of acceleration to position then provides a measurement of the stiffness.
- **The $G_{df_{XIS2}}(p)$ block:** The AOCs controller computes the acceleration that needs to be applied to the satellite in order to compensate for the non-gravitational accelerations. For the satellite linear acceleration, the calculation uses the instrument measurement as input, whereas for the angular acceleration, the calculation uses both the instrument and the stellar sensor measurements. This allows to combine two types of information to estimate the satellite attitude: the angular acceleration measurement provided by the instrument, more effective at high frequencies, integrated twice, and the attitude measurement provided by the stellar sensor, more effective at low frequencies. This hybridization technique allows to improve the precision of the estimated satellite attitude. The estimated attitude is obtained by applying a high-pass filter to the measured angular acceleration integrated twice, and a low-pass filter to attitude measurement provided by the stellar sensor:

$$\Phi_{hyb} = \frac{1}{p^2} \frac{p^2}{p^2 + 2a_{DF}\omega_{DF}p + \omega_{DF}^2} \Gamma_{meas,ang} + \frac{\omega_{SST}^2}{p^2 + 2a_{SST}\omega_{SST}p + \omega_{SST}^2} \Phi_{SST} \quad (3.4)$$

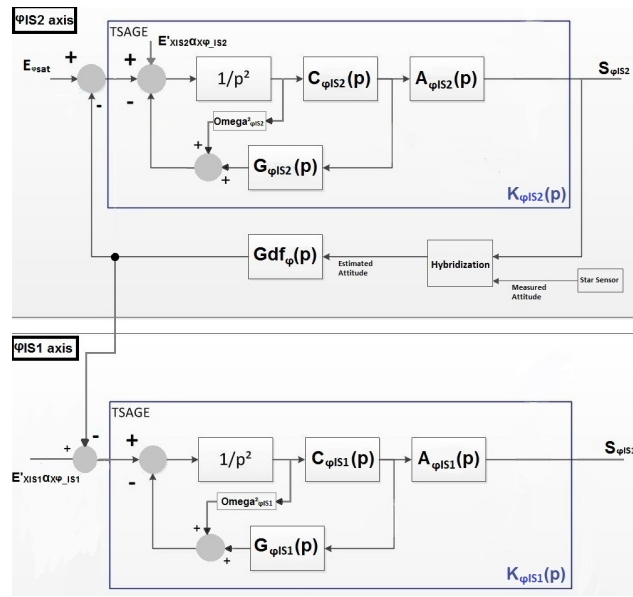
Where Φ_{hyb} refers to the estimated satellite attitude, $\Gamma_{meas,ang}$ refers to the angular acceleration measurement provided by the instrument, Φ_{SST} represents the satellite attitude measurement provided by the stellar sensor, and a_{DF} , ω_{DF} , a_{SST} , ω_{SST} are the parameters of the hybridization block. The acceleration that needs to be applied to the satellite to compensate for the non-gravitational accelerations are then computed for each axis. Two different calculator transfer functions are used for the linear and angular accelerations. These functions are provided by the CNES, which is responsible for this subsystem. Once the acceleration computed, it is applied by the propulsion system.

The various parameters of the $C(p)$, $G(p)$ and $A(p)$ block control functions introduced through the previous relations, are detailed in [Appendix B](#). As mentioned earlier, the first investigation of the coupling between axes is based on a simplified linear model. Therefore, the model used only takes into account the couplings between the axis along which the sinusoid of specific frequency is applied, and the others. In other words, concerning the K_{1dx} calibration sessions, the only coupling factors taken into account are $X > Y$, $X > Z$, $X > \phi$, $X > \psi$ and $X > \theta$. The control of the remaining axes is illustrated on [Figure 3.3](#).

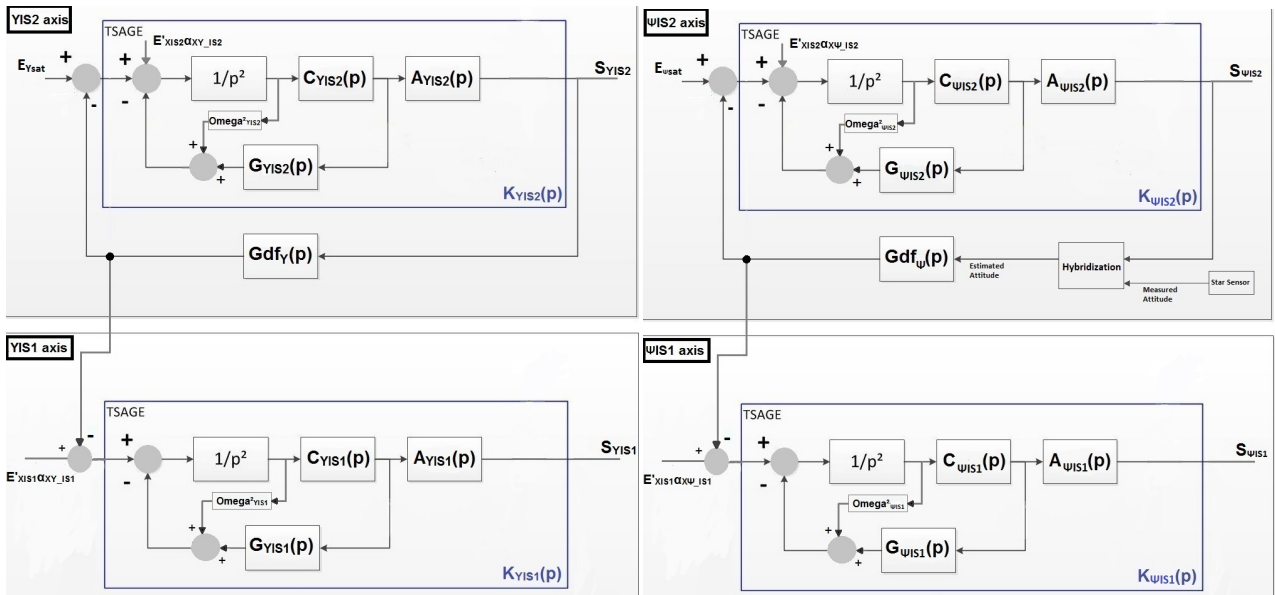
E_{Ysat} , E_{Zsat} , $E_{\phi sat}$, $E_{\psi sat}$ and $E_{\theta sat}$ denote the external acceleration along the various axes of the satellite. In the mission phases investigated, it is assumed that:

$$E_{Xsat} = E_{Ysat} = E_{Zsat} = E_{\phi sat} = E_{\psi sat} = E_{\theta sat} \approx 0$$

On [Figure 3.3](#), the α parameters refer to the coupling factors between axes, for either the internal or the external test-mass. The main objective of this chapter is to precisely evaluate their values.

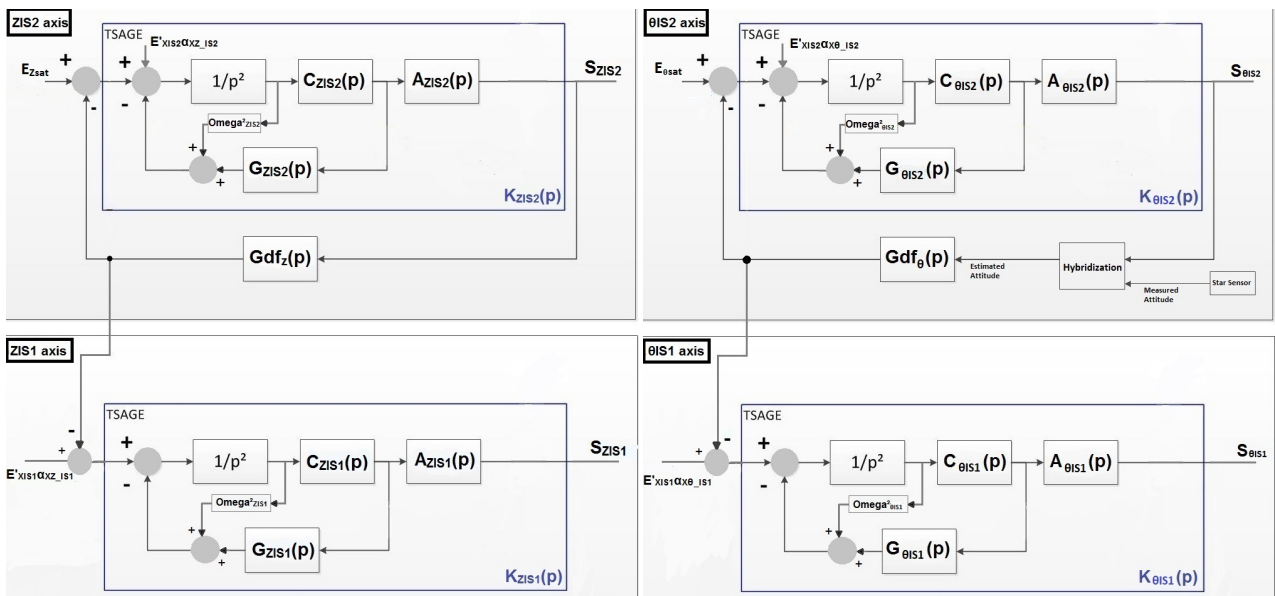


(a) ϕ -axis - Rotation around X



(b) Y-axis

(c) ψ -axis - Rotation around Y



(d) Z-axis

(e) θ -axis - Rotation around Z

Figure 3.3: Illustration of the instrument loop for the linear and angular axes, for a K_{1dx} calibration session.

3.2.3. Processing of the calibration sessions in the investigation of the coupling factors:

This subsection will be dedicated to the processing of the various calibration sessions, introduced in [subsection 3.2.1](#), in order to investigate the values of the coupling factors. Since the CNES did not provide the values of the hybridization block parameters introduced in the previous part, it will not be possible to study the coupling between the linear and the angular axes. Only the coupling factors between the linear axes, referred to as the linear-to-linear coupling factors will be explored (for instance X > Y and X > Z). The work approach will be illustrated with a K_{1dx} calibration session during which the drag-compensating system is set to compensate the motion of the external test-mass, but the same investigation process will be applied to the other types of calibration sessions to estimate the remaining linear-to-linear coupling factors.

First, the closed-loop transfer functions of the linear axes models illustrated in both [Figure 3.1](#) and [Figure 3.3](#) need to be established.

□ X_{IS2} :

$$S_{XIS2} = \left[\frac{p^2 + \omega_{pXIS2}^2 + C_{XIS2}(p)G_{XIS2}(p)}{p^2 + \omega_{pXIS2}^2 + C_{XIS2}(p)G_{XIS2}(p) + A_{XIS2}(p)C_{XIS2}(p)Gdf_X(p)} \right] E_X \quad (3.5)$$

Where E_X represents the sinusoid applied to the instrument loop to force an oscillation of the test-mass:

$$E_X(t) = (5 \cdot 10^{-8}) \cdot \sin(2\pi(1.23 \cdot 10^{-3})t)$$

In order to simplify the relations, the function $D_{i,j}(p)$ is introduced, where the index i denotes the axis (X, Y or Z) and the index j denotes the test-mass (internal IS1, or external IS2):

$$D_{i,j}(p) = p^2 + \omega_{p_{i,j}}^2 + C_{i,j}(p)G_{i,j}(p) + A_{i,j}(p)C_{i,j}(p)Gdf_i(p)$$

The [Equation 3.5](#) can consequently be rewritten as:

$$S_{XIS2} = \left[\frac{p^2 + \omega_{pXIS2}^2 + C_{XIS2}(p)G_{XIS2}(p)}{D_{XIS2}(p)} \right] E_X \quad (3.6)$$

□ X_{IS1} :

$$S_{XIS1} = - \left[\frac{A_{XIS1}(p)C_{XIS1}(p)}{p^2 + \omega_{pXIS1}^2 + C_{XIS1}(p)G_{XIS1}(p)} \right] \left[\frac{(p^2 + \omega_{pXIS2}^2 + C_{XIS2}(p)G_{XIS2}(p))Gdf_X(p)}{D_{XIS2}(p)} \right] E_X \quad (3.7)$$

□ Y_{IS2} :

$$S_{YIS2} = \left[\frac{A_{YIS2}(p)C_{YIS2}(p)}{D_{YIS2}(p)} \right] E'_{X2} \alpha_{XYIS2} \quad (3.8)$$

Where

$$E'_{X2} = - \left[\frac{\omega_{pXIS2}^2 + C_{XIS2}(p)G_{XIS2}(p)}{A_{XIS2}(p)C_{XIS2}(p)} \right] \left[\frac{A_{XIS2}(p)C_{XIS2}(p)Gdf_X(p)}{D_{XIS2}(p)} \right] E_X \quad (3.9)$$

Therefore, [Equation 3.8](#) can be written as:

$$S_{YIS2} = - \left[\frac{A_{YIS2}(p)C_{YIS2}(p)}{D_{YIS2}(p)} \right] \left[\frac{(\omega_{pXIS2}^2 + C_{XIS2}(p)G_{XIS2}(p))Gdf_X(p)}{D_{XIS2}(p)} \right] E_X \alpha_{XYIS2} \quad (3.10)$$

□ Y_{IS1} :

$$S_{YIS1} \left[\frac{p^2 + \omega_{pYIS1}^2 + C_{YIS1}(p)G_{YIS1}(p)}{A_{YIS1}(p)C_{YIS1}(p)} \right] = E'_{X1} \alpha_{XYIS1} - Gdf_Y S_{YIS2} \quad (3.11)$$

Where

$$E'_{X1} = - \left[\frac{\omega_{p_{X1S1}}^2 + C_{X1S1}(p)G_{X1S1}(p)}{p^2 + \omega_{p_{X1S1}}^2 + C_{X1S1}(p)G_{X1S1}(p)} \right] \left[\frac{(p^2 + \omega_{p_{X1S2}}^2 + C_{X1S2}(p)G_{X1S2}(p))Gdf_X(p)}{D_{X1S2}(p)} \right] E_X \quad (3.12)$$

Therefore, Equation 3.11 can be written as:

$$S_{Y1S1} \left[\frac{p^2 + \omega_{p_{Y1S1}}^2 + C_{Y1S1}(p)G_{Y1S1}(p)}{A_{Y1S1}(p)C_{Y1S1}(p)} \right] = - \left[\frac{\omega_{p_{X1S1}}^2 + C_{X1S1}(p)G_{X1S1}(p)}{p^2 + \omega_{p_{X1S1}}^2 + C_{X1S1}(p)G_{X1S1}(p)} \right] \left[\frac{(p^2 + \omega_{p_{X1S2}}^2 + C_{X1S2}(p)G_{X1S2}(p))Gdf_X(p)}{D_{X1S2}(p)} \right] E_X \alpha_{XY1S1} \\ + \left[\frac{A_{Y1S2}(p)C_{Y1S2}(p)Gdf_Y(p)}{D_{Y1S2}(p)} \right] \left[\frac{(\omega_{p_{X1S2}}^2 + C_{X1S2}(p)G_{X1S2}(p))Gdf_X(p)}{D_{X1S2}(p)} \right] E_X \alpha_{XY1S2} \quad (3.13)$$

□ **Z_{1S2} and Z_{1S1}** : Since the Y- and Z-sensors have the same working principle, it can easily be inferred from Figure 3.3 that the expressions for S_{Z1S2} and S_{Z1S1} are respectively the same as the expressions derived for S_{Y1S2} and S_{Y1S1} , by replacing the index "Y" by "Z".

The expressions for the functions **A**, **C** and **G** of each sensor have been established through previous research works ([18], [21]), as illustrated in subsection 3.2.2. Nonetheless, the expression for the transfer function of the linear AOCS system **Gdf** is unknown. The CNES only provided gain and phase values for discrete values of frequencies, as seen in Table 3.1. The linear AOCS block is the same for the three linear axes X, Y and Z, leading to:

$$Gdf_X = Gdf_Y = Gdf_Z$$

Table 3.1: Gain and Phase values of the linear AOCS system for discrete values of frequency, provided by the CNES

f (Hz)	$\omega = 2\pi f$ (rad/s)	Gain	Gain expressed in decibels (dB)	Phase (°)
0.001	0.0063	14880.3955	83.4523	-218.9955
0.003	0.0188	341.0216	50.6556	-264.6633
0.006	0.0377	29.3917	29.3645	-239.5528
0.01	0.0628	7.1646	17.1038	-195.8111
0.03	0.1885	1.5327	3.7089	-124.4834
0.06	0.3770	0.7485	-2.5163	-107.0318
0.1	0.6283	0.4466	-7.0022	-100.1781
0.3	1.8850	0.1461	-16.7077	-93.3319
0.6	3.7699	0.0688	-23.2456	-91.5697
1	6.2832	0.0351	-29.1027	-90.7998

In order to be able to estimate the gain and phase values of the linear AOCS system at the frequency of the test, the linear AOCS block has to be modelled by a transfer function complying with the constraints imposed by the values provided by the CNES. A brief analysis of the evolution of both the gain and the phase indicates a 4th order system. The transfer function therefore contains 4 poles and at most 3 zeros, leading to a relation with the following form:

$$Gdf(p) = \frac{b_0 + b_1 p + b_2 p^2 + b_3 p^3}{a_0 + a_1 p + a_2 p^2 + a_3 p^3 + a_4 p^4} \quad (3.14)$$

The parameters a_0 , a_1 , a_2 , a_3 , b_0 , b_1 , b_2 , b_3 and b_4 mentioned in the relation above are estimated by means of a nonlinear least-squares method, to minimize the loss function:

$$\text{Minimize} \sum_{k=1}^{n_f} \left| \left(y(\omega_k) - \frac{N(\omega_k)}{D(\omega_k)} u(\omega_k) \right) \right|^2$$

Table 3.2: Estimated values for the parameters of the linear AOCS block transfer function

Numerator Parameters				
b_0	b_1	b_2	b_3	
$4.1051 \cdot 10^{-5}$	$1.9853 \cdot 10^{-3}$	$3.5369 \cdot 10^{-2}$	$2.8797 \cdot 10^{-1}$	
Denominator Parameters				
a_0	a_1	a_2	a_3	a_4
$3.4497 \cdot 10^{-10}$	$2.0220 \cdot 10^{-7}$	$8.7468 \cdot 10^{-5}$	$1.4486 \cdot 10^{-2}$	1

Where N and D respectively denote the numerator and denominator of the transfer function model that is to be estimated, y and u are the measured output and input data, and n_f is the number of frequencies. The results of the estimation algorithm, to convert the frequency-response data into a transfer function are gathered below:

The Figure 3.4 illustrates the Bode diagram of the estimated linear AOCS block transfer function with respect to the real magnitude and phase values provided by the CNES.

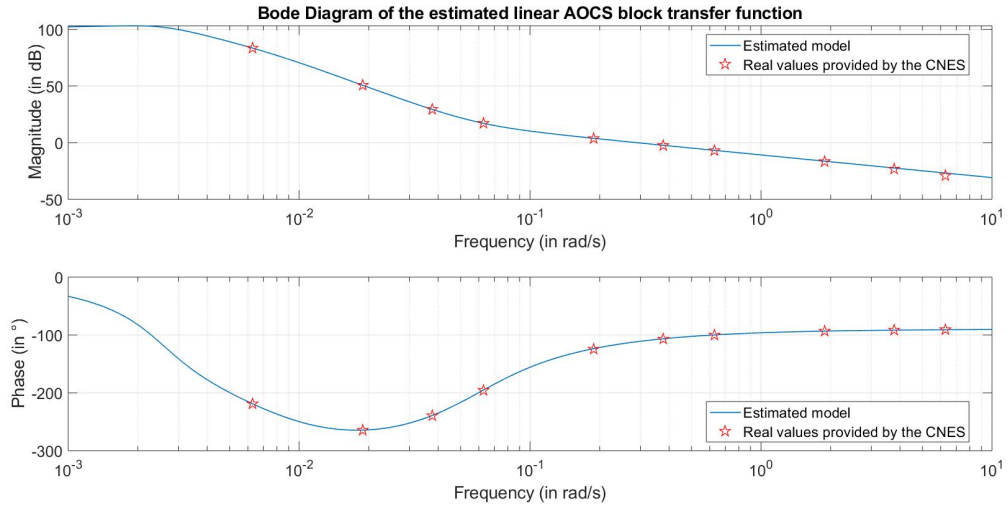


Figure 3.4: Bode Diagram of the estimated linear AOCS block transfer function with respect to the real magnitude and phase values provided by the CNES

It can be inferred from the Figure 3.4 that the magnitude of the transfer function Gdf at the frequency of the calibration session $f_{cal/lin} = 1.23 \cdot 10^{-3}$ Hz is approximately equal to **78dB**. In comparison with the other transfer functions A , C and G at the same frequency $f_{cal/lin}$, the magnitude of the Gdf transfer function can be considered as infinite. The relations established in the previous paragraph can therefore be simplified. In the following relations, the accelerometer transfer function along the i -direction, for the test-mass j is equal to:

$$K_{ij}(p) = \frac{A_{ij}(p)C_{ij}(p)}{p^2 + \omega_{p,ij}^2 + C_{ij}(p)G_{ij}(p)}$$

Considering the magnitude of the linear AOCS transfer function as infinite at the frequency of the calibration session, the closed-loop transfer functions of the models illustrated in Figure 3.1 and Figure 3.3 can be simplified:

□ X_{IS2} :

$$|S_{XIS2}(f = f_{cal/lin})| \approx 0 \quad (3.15)$$

□ X_{IS1} :

$$S_{XIS1}(f = f_{cal/lin}) \approx -\frac{K_{XIS1}(p_{f=f_{cal/lin}})}{K_{XIS2}(p_{f=f_{cal/lin}})} E_X \quad (3.16)$$

□ Y_{IS2} :

$$|S_{YIS2}(f = f_{cal/lin})| \approx 0 \quad (3.17)$$

□ Y_{IS1} :

$$S_{YIS1}(f = f_{cal/lin}) \approx \frac{K_{YIS1}(p_{f=f_{cal/lin}})}{K_{XIS2}(p_{f=f_{cal/lin}})} (\alpha_{XYIS2} - \alpha_{XYIS1}) E_X \quad (3.18)$$

□ Z_{IS2} :

$$|S_{ZIS2}(f = f_{cal/lin})| \approx 0 \quad (3.19)$$

□ Z_{IS1} :

$$S_{ZIS1}(f = f_{cal/lin}) \approx \frac{K_{ZIS1}(p_{f=f_{cal/lin}})}{K_{XIS2}(p_{f=f_{cal/lin}})} (\alpha_{XZIS2} - \alpha_{XZIS1}) E_X \quad (3.20)$$

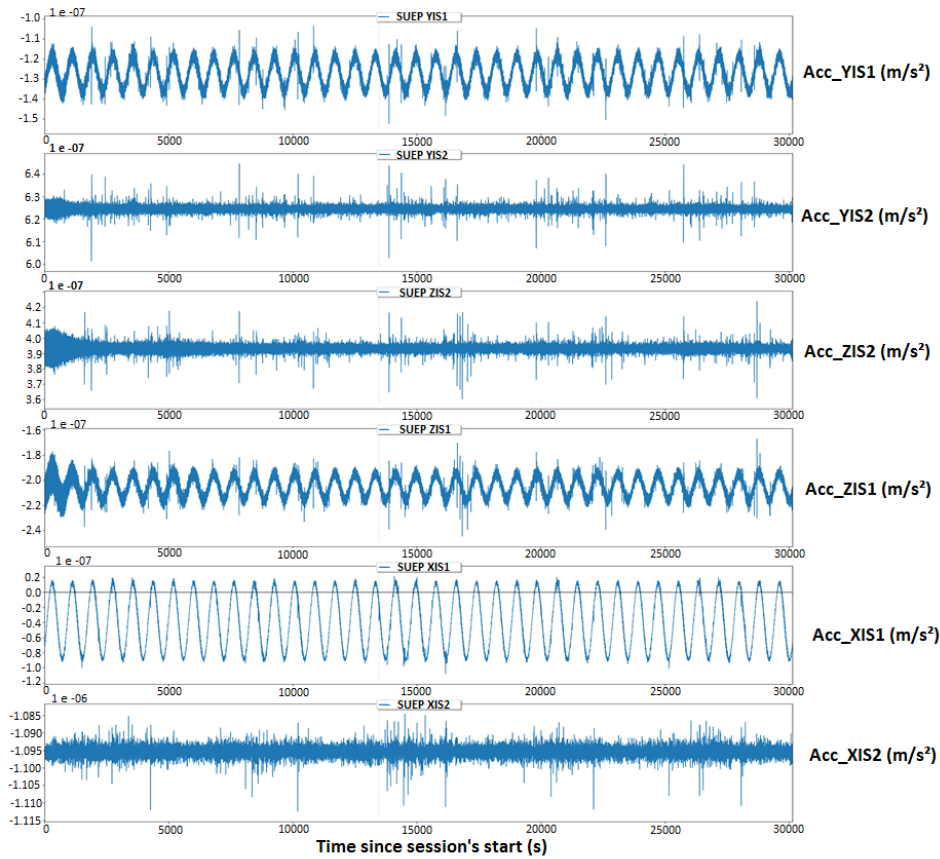


Figure 3.5: Acceleration measured in-orbit along the linear axes during a $K1dx$ calibration session

As observed in the previous relations, and illustrated in Figure 3.5, because of the high gain of the linear AOCs transfer function at $f_{cal/lin}$, the S_{XIS2} , S_{YIS2} and S_{ZIS2} outputs are mainly constituted of noise (the random peaks observed in the accelerometer data along every axes in Figure 3.5 result from both instrument noise

and saturation events due to the satellite environment). At a frequency $f_{cal/lin}$, the drag-free control block is able to precisely compensate for the acceleration applied to the external test-mass IS2 (expected behavior). In other words, because of the gain of the linear AOCS transfer function at $f_{cal/lin}$, no valuable information can be extracted from the S_{XIS2} , S_{YIS2} and S_{ZIS2} outputs. Thanks to the relations previously established, it can be derived that:

$$\left| \frac{S_{YIS1}(f = f_{cal/lin})}{S_{XIS1}(f = f_{cal/lin})} \right| \approx \left| \frac{K_{YIS1}(p_f = f_{cal/lin})}{K_{XIS1}(p_f = f_{cal/lin})} \right| |\alpha_{XYIS1} - \alpha_{XYIS2}| \quad (3.21)$$

and

$$\left| \frac{S_{ZIS1}(f = f_{cal/lin})}{S_{XIS1}(f = f_{cal/lin})} \right| \approx \left| \frac{K_{ZIS1}(p_f = f_{cal/lin})}{K_{XIS1}(p_f = f_{cal/lin})} \right| |\alpha_{XZIS1} - \alpha_{XZIS2}| \quad (3.22)$$

The expression for K_{XIS1} , K_{YIS1} and K_{ZIS1} being known, it can easily be computed that:

$$\left| \frac{K_{YIS1}(p_f = f_{cal/lin})}{K_{XIS1}(p_f = f_{cal/lin})} \right| \approx 1 \quad \text{and} \quad \left| \frac{K_{ZIS1}(p_f = f_{cal/lin})}{K_{XIS1}(p_f = f_{cal/lin})} \right| \approx 1$$

Equation 3.21 and Equation 3.22 therefore lead to:

$$\left| \frac{S_{YIS1}(f = f_{cal/lin})}{S_{XIS1}(f = f_{cal/lin})} \right| \approx |\alpha_{XYIS1} - \alpha_{XYIS2}| \quad (3.23)$$

and

$$\left| \frac{S_{ZIS1}(f = f_{cal/lin})}{S_{XIS1}(f = f_{cal/lin})} \right| \approx |\alpha_{XZIS1} - \alpha_{XZIS2}| \quad (3.24)$$

It can be inferred from Equation 3.23 and Equation 3.24 that a careful analysis of the accelerometer data during the calibration sessions allows an estimation of the values of $(\alpha_{XYIS1} - \alpha_{XYIS2})$ and $(\alpha_{XZIS1} - \alpha_{XZIS2})$, referred to as the differential linear-to-linear coupling factors. A sinusoid is first fit to each data set and the absolute value of the differential coupling factors is obtained from the ratio of the oscillation amplitudes. The signs (+/-) of the differential coupling factors are given by a comparative study of the phases of the fitted signals. An algorithm encoded in Python language has been developed to automate the process to all the calibration sessions. It is described below in Table 3.3.

The results from all the K_{1dx} calibration sessions are presented in Table 3.4. As mentioned earlier, the various session numbers correspond to the several calibration sessions achieved throughout the MICROSCOPE mission. The results are presented with a 99% confidence interval (3- σ results).

This method has drawbacks because the sinusoid requires a fit of three variables (amplitude, phase and offset) for each data set, but only the amplitude and phase are used. In the K_{1dx} calibration sessions processed, the drag-compensating system was set to compensate the motion of the external test-mass IS2 (characterized as $DFIS2$, standing for Drag-Free on IS2). The same reasoning applied to sessions in which the drag-compensating system is set to compensate the motion of the internal test-mass IS1 (characterized as $DFIS1$) leads to the following relations:

□ X_{IS2} :

$$S_{XIS2}(f = f_{cal/lin}) \approx -\frac{K_{XIS2}(p_f = f_{cal/lin})}{K_{XIS1}(p_f = f_{cal/lin})} E_X \quad (3.25)$$

□ X_{IS1} :

$$|S_{XIS1}(f = f_{cal/lin})| \approx 0 \quad (3.26)$$

□ Y_{IS2} :

$$S_{YIS2}(f = f_{cal/lin}) \approx \frac{K_{YIS2}(p_f = f_{cal/lin})}{K_{XIS1}(p_f = f_{cal/lin})} (\alpha_{XYIS1} - \alpha_{XYIS2}) E_X \quad (3.27)$$

Table 3.3: Algorithm used to extract the differential linear-to-linear coupling factors from the K_{1dx} calibration sessions

Algorithm 1: Extraction of the differential linear-to-linear coupling factors from the K_{1dx} calibration sessions	
Require:	The accelerometer data sets measured along the linear axes during all the K_{1dx} calibration sessions
Require:	The frequency of the signal applied to force an oscillation of the test-mass along the X-axis
1:	For all K_{1dx} calibration sessions
2:	Fit the accelerometer data sets S_{XIS1} , S_{YIS1} and S_{ZIS1} with a sinusoidal function $a \sin(2\pi f_{callin} t + \Phi) + b$ by means of a least-squares method. This process requires a fit of three variables for each data set: the amplitude a , the phase Φ and the offset b .
3:	Compute the ratios of the estimated oscillation amplitudes $\frac{a_{YIS1}}{a_{XIS1}}$ and $\frac{a_{ZIS1}}{a_{XIS1}}$. These ratios are respectively equal to $ \alpha_{XYIS1} - \alpha_{XYIS2} $ and $ \alpha_{XZIS1} - \alpha_{XZIS2} $.
4:	if $\Phi_{YIS1} = \Phi_{XIS1} [2\pi]$ then
5:	$\alpha_{XYIS1} - \alpha_{XYIS2} = \alpha_{XYIS1} - \alpha_{XYIS2} $
6:	else
7:	$\alpha_{XYIS1} - \alpha_{XYIS2} = - \alpha_{XYIS1} - \alpha_{XYIS2} $
8:	end if
9:	if $\Phi_{ZIS1} = \Phi_{XIS1} [2\pi]$ then
10:	$\alpha_{XZIS1} - \alpha_{XZIS2} = \alpha_{XZIS1} - \alpha_{XZIS2} $
11:	else
12:	$\alpha_{XZIS1} - \alpha_{XZIS2} = - \alpha_{XZIS1} - \alpha_{XZIS2} $
13:	end if
14:	end for

Table 3.4: Processing of the $K_{1dx-DFIS2}$ calibration sessions and 3- σ estimation of $(\alpha_{XYIS1} - \alpha_{XYIS2})$ and $(\alpha_{XZIS1} - \alpha_{XZIS2})$ for the SUEP instrument

K_{1dx} calibration session - SUEP - Drag-Free IS2		
Session number	$\alpha_{XYIS1} - \alpha_{XYIS2}$	$\alpha_{XZIS1} - \alpha_{XZIS2}$
208	0.16142	0.17867
216	0.17611	0.20442
232	0.17617	0.20459
246	0.17632	0.20545
250	0.17615	0.20461
264	0.17662	0.20597
312	0.17719	0.20932
318	0.17693	0.20905
324	0.17684	0.20997
330	0.17703	0.20773
400	0.17694	0.20769
422	0.15839	0.18151
436	0.15797	0.17567
444	0.15831	0.17668
Mean Value	0.172	0.20
Standard Deviation σ	0.008	0.01
3-σ result	0.172 \pm 0.024	0.20 \pm 0.03

□ Y_{IS1} :

$$|S_{YIS1}(f = f_{callin})| \approx 0 \quad (3.28)$$

□ Z_{IS2} :

$$|S_{ZIS2}(f = f_{cal/lin})| \approx \frac{K_{ZIS2}(p_{f=f_{cal/lin}})}{K_{XIS2}(p_{f=f_{cal/lin}})} (\alpha_{XZIS1} - \alpha_{XZIS2}) E_X \quad (3.29)$$

□ Z_{IS1} :

$$|S_{ZIS1}(f = f_{cal/lin})| \approx 0 \quad (3.30)$$

The expression for K_{XIS2} , K_{YIS2} and K_{ZIS2} being known, it can be easily derived that:

$$\left| \frac{S_{YIS2}(f = f_{cal/lin})}{S_{XIS2}(f = f_{cal/lin})} \right| \approx |\alpha_{XYIS2} - \alpha_{XYIS1}| \quad (3.31)$$

and

$$\left| \frac{S_{ZIS2}(f = f_{cal/lin})}{S_{XIS2}(f = f_{cal/lin})} \right| \approx |\alpha_{XZIS2} - \alpha_{XZIS1}| \quad (3.32)$$

While the processing of the $K_{1dx-DFIS2}$ calibration sessions led to an estimation of the values of $(\alpha_{XYIS1} - \alpha_{XYIS2})$, and $(\alpha_{XZIS1} - \alpha_{XZIS2})$, it can be inferred from Equation 3.31 and Equation 3.32 that a careful analysis of the accelerometer data during the $K_{1dx-DFIS1}$ calibration sessions allows an estimation of the values of $(\alpha_{XYIS2} - \alpha_{XYIS1})$ and $(\alpha_{XZIS2} - \alpha_{XZIS1})$. Therefore, the processing of the $K_{1dx-DFIS1}$ calibration sessions will allow to support the results previously computed for the differential linear-to-linear coupling factors. Another Python algorithm, similar to the one presented in Table 3.3, has been developed to automate the process to all the $K_{1dx-DFIS1}$ calibration sessions.

Table 3.5: Processing of the $K_{1dx-DFIS1}$ calibration sessions and 3- σ estimation of $(\alpha_{XYIS2} - \alpha_{XYIS1})$ and $(\alpha_{XZIS2} - \alpha_{XZIS1})$ for the SUEP instrument

K_{1dx} calibration session - SUEP - Drag-Free IS1		
Session number	$\alpha_{XYIS2} - \alpha_{XYIS1}$	$\alpha_{XZIS2} - \alpha_{XZIS1}$
78	-0.16012	-0.17327
84	-0.17376	-0.18211
106	-0.17291	-0.18125
146	-0.17373	-0.18384
206	-0.15241	-0.16807
Mean Value	-0.167	-0.178
Standard Deviation σ	0.009	0.006
3-σ result	-0.167 \pm 0.027	-0.178 \pm 0.018

The results obtained with the $K_{1dx-DFIS1}$ calibration sessions and gathered in Table 3.5 are relevant with the ones obtained with the $K_{1dx-DFIS2}$ calibration sessions and gathered in Table 3.4.

The same steps are adapted and applied to the other types of calibration sessions, introduced in subsection 3.2.1 and referred to as $Theta_{dy}$ and $Theta_{dz}$ sessions, in order to estimate the remaining differential linear-to-linear coupling factors ($Y > X$, $Y > Z$, $Z > X$ and $Z > Y$). The final results are summarized in Table 3.6 (all the detailed results of the various calibration sessions processing are gathered in Appendix C).

The exact same approach as the one developed in this part is applied to compute the differential linear-to-linear coupling factors for the second instrument, referred to as the SUREF instrument. The results are summarized in Table 3.7 (the session by session results are gathered in Appendix C). The $\Theta_{dy-DFIS1}$ and $\Theta_{dz-DFIS}$ calibration sessions (that is to say the Θ_{dy} and Θ_{dz} calibration sessions during which the drag-compensation system is set to compensate the motion of the internal test-mass IS1) do not appear on the table because they have not been achieved throughout the mission scenario.

This subsection has allowed to highlight the fact that, because of the high gain of the drag-free control block at $f_{cal/lin} = 1.23 \cdot 10^{-3}$ Hz, the processing of the various calibration sessions can only give access to the differential linear-to-linear coupling factors, as observed in Table 3.4, Table 3.5, Table 3.6 and Table 3.7. A new approach thus needs to be established in order to estimate the linear-to-linear coupling factors: this is developed in the next section.

Table 3.6: Processing of the Θ_{dy} and Θ_{dz} calibration sessions and 3- σ estimation of the remaining differential linear-to-linear coupling factors for the SUEP instrument

Θ_{dz} calibration session - SUEP - Drag-Free IS2			
Differential linear-to-linear coupling factors	Mean Value	Standard Deviation σ	3- σ result
$\alpha_{YXIS1} - \alpha_{YXIS2}$	$-5 \cdot 10^{-4}$	$2 \cdot 10^{-4}$	$[-5 \pm 6] \cdot 10^{-4}$
$\alpha_{YZIS1} - \alpha_{YZIS2}$	$3 \cdot 10^{-3}$	$1 \cdot 10^{-1}$	$[3 \pm 3] \cdot 10^{-3}$
Θ_{dz} calibration session - SUEP - Drag-Free IS1			
$\alpha_{YXIS2} - \alpha_{YXIS1}$	$5 \cdot 10^{-4}$	Only one session achieved	
$\alpha_{YZIS2} - \alpha_{YZIS1}$	$-1.8 \cdot 10^{-3}$	Only one session achieved	
Θ_{dy} calibration session - SUEP - Drag-Free IS2			
$\alpha_{ZXIS1} - \alpha_{ZXIS2}$	$4 \cdot 10^{-4}$	$2 \cdot 10^{-4}$	$[4 \pm 6] \cdot 10^{-4}$
$\alpha_{ZYIS1} - \alpha_{ZYIS2}$	$-6 \cdot 10^{-4}$	$2 \cdot 10^{-4}$	$[-6 \pm 6] \cdot 10^{-4}$
Θ_{dy} calibration session - SUEP - Drag-Free IS1			
$\alpha_{ZXIS2} - \alpha_{ZXIS1}$	No session completed		
$\alpha_{ZYIS2} - \alpha_{ZYIS1}$	No session completed		

Table 3.7: Processing of the K_{1dx} , Θ_{dy} and Θ_{dz} calibration sessions and 3- σ estimation of the differential linear-to-linear coupling factors for the SUREF instrument

K_{1dx} calibration session - SUREF - Drag-Free IS2			
Differential linear-to-linear coupling factors	Mean Value	Standard Deviation σ	3- σ result
$\alpha_{XYIS1} - \alpha_{XYIS2}$	0.103	$1 \cdot 10^{-3}$	0.103 \pm 0.003
$\alpha_{XZIS1} - \alpha_{XZIS2}$	-0.016	$1 \cdot 10^{-3}$	-0.016 \pm 0.003
K_{1dx} calibration session - SUREF - Drag-Free IS1			
$\alpha_{XYIS2} - \alpha_{XYIS1}$	-0.1013	$6 \cdot 10^{-4}$	-0.1013 \pm 0.0018
$\alpha_{XZIS2} - \alpha_{XZIS1}$	0.0133	$4 \cdot 10^{-4}$	0.0133 \pm 0.0012
Θ_{dz} calibration session - SUREF - Drag-Free IS2			
$\alpha_{YXIS1} - \alpha_{YXIS2}$	$-3 \cdot 10^{-4}$	$2 \cdot 10^{-4}$	$[-3 \pm 6] \cdot 10^{-4}$
$\alpha_{YZIS1} - \alpha_{YZIS2}$	$2.14 \cdot 10^{-3}$	$4 \cdot 10^{-5}$	$[2.14 \pm 0.12] \cdot 10^{-3}$
Θ_{dy} calibration session - SUREF - Drag-Free IS2			
$\alpha_{ZXIS1} - \alpha_{ZXIS2}$	$-2.3 \cdot 10^{-4}$	$8 \cdot 10^{-5}$	$[-2.3 \pm 2.4] \cdot 10^{-4}$
$\alpha_{ZYIS1} - \alpha_{ZYIS2}$	$-1.33 \cdot 10^{-3}$	$5 \cdot 10^{-5}$	$[-1.33 \pm 0.15] \cdot 10^{-3}$

3.3. Exploitation of a new type of mission phase

The new approach will be based on the processing of a specific mission phase referred to as **Technical session n°516**. Throughout this session, realized with the SUEP instrument, a sinusoid of amplitude 0.148V and frequency $f_{tech} = 0.1\text{Hz}$ is first applied in the instrument control loop to force an oscillation of the test-mass position along the X-axis during 100s, as illustrated in Figure 3.6.

Then, a sinusoid with the same frequency f_{tech} , but a different amplitude (0.01V) is induced in the satellite motion along the Y-axis during 100s, and finally along the Z-axis during 100s.

During this session, the drag-free control block is set to compensate the motion of the external test-mass IS2. According to Table 3.1, in comparison with the calibration sessions, at $f_{tech} = 0.1\text{Hz}$, the gain of the linear drag-free control block is reduced **from 78dB to -7dB**. Therefore, contrary to the calibration sessions during which no valuable information could be extracted from the S_{XIS2} , S_{YIS2} and S_{ZIS2} outputs, the technical session n°516 allows to process each one of these outputs, as observed on Figure 3.7.

The careful analysis of the technical session n°516 should thus lead to the derivation of the linear-to-linear coupling factors for the SUEP instrument. The session will be analyzed section by section: between 216s and 316s for the excitation along the X-axis, between 366s and 466s for the excitation along the Y-axis, and finally, between 516s and 566s for the excitation along the Z-axis. In the interest of clarity and simplicity, the investigation process will only be illustrated for the excitation along the X-axis, but the same approach will be applied for the excitation along the other axes.

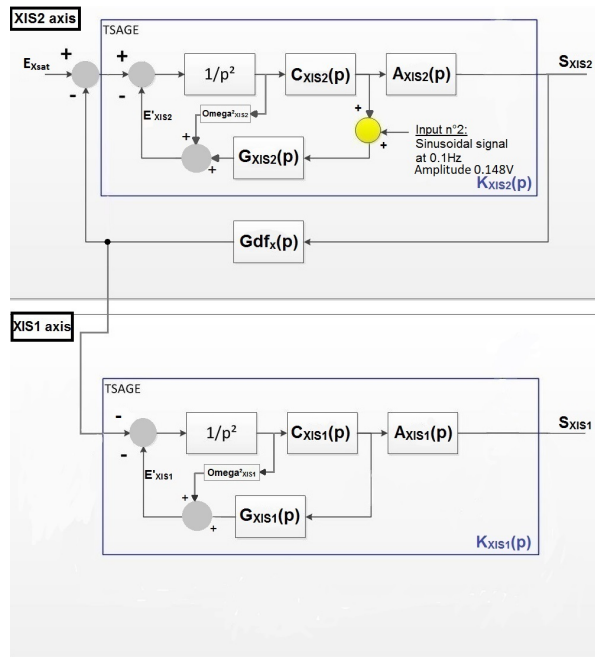


Figure 3.6: Illustration of the instrument control loop along the X-axis for the technical session n°516

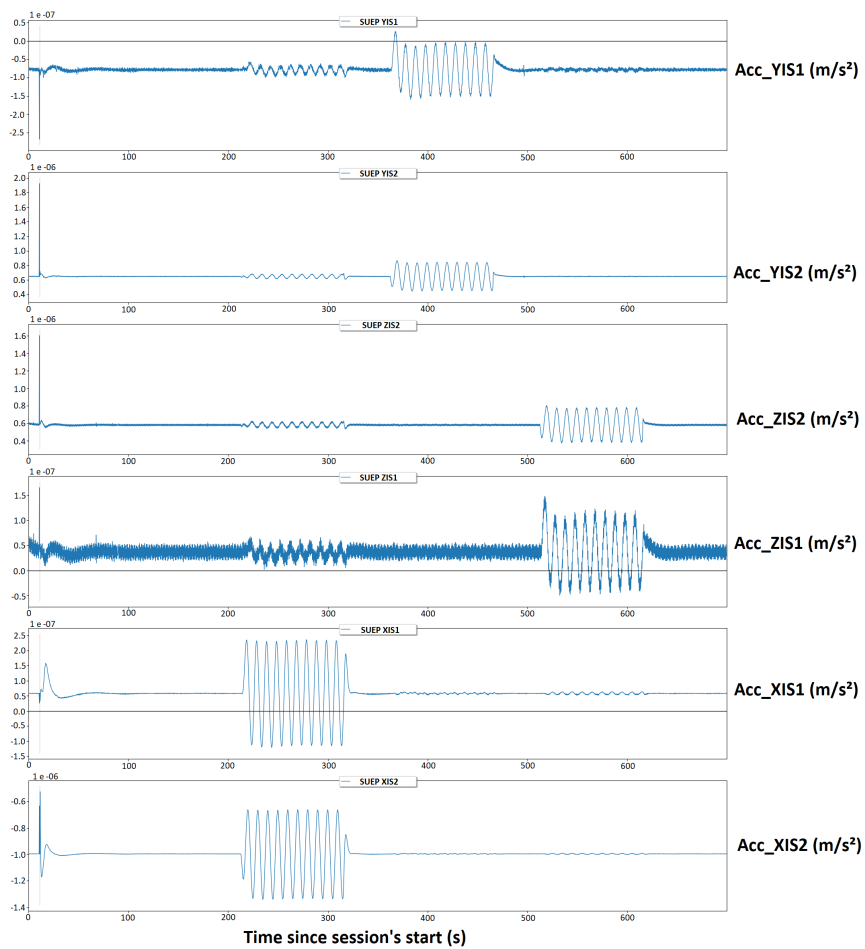


Figure 3.7: Acceleration measured in-orbit along the linear axes during the technical session n°516

Since the port of entry of the excitation signal is different than the one used for the calibration sessions, the closed-loop transfer functions of the linear axes models need to be derived again. The model for the X-axis is illustrated on Figure 3.6, while the model for the remaining axes is the same as the one used for the calibration sessions, illustrated on Figure 3.3.

□ X_{IS2} :

$$S_{XIS2} = - \left[\frac{A_{XIS2}(p)C_{XIS2}(p)G_{XIS2}(p)}{D_{XIS2}(p)} \right] E'_X \quad (3.33)$$

Where $D_{XIS2}(p)$ denotes the function introduced in subsection 3.2.3 and E'_X represents the sinusoid applied to the instrument loop to force an oscillation of the test-mass:

$$E'_X(t) = 0.148 \cdot \sin(2\pi(0.1)t)$$

□ X_{IS1} :

$$S_{XIS1} = K_{XIS1}(p) \left[\frac{A_{XIS2}(p)C_{XIS2}(p)G_{XIS2}(p)Gdf_X(p)}{D_{XIS2}(p)} \right] E'_X \quad (3.34)$$

Where $K_{XIS1}(p)$ denotes the accelerometer transfer function along the X-axis, for the internal test-mass, introduced in subsection 3.2.3.

The accelerometer data sets S_{XIS2} and S_{XIS1} are fitted with a sinusoidal function $a \sin(2\pi f_{tech}t + \phi) + b$ by means of a least-squares method. The frequency f_{tech} being admitted, this process requires a fit of three variables for each data set: the amplitude a , the phase ϕ and the offset b . Since the expressions for the functions **A**, **C**, **G** and **Gdf** of each sensor have already been established, the values for the theoretical values of $|S_{XIS2}(f = f_{tech})|$ and $|S_{XIS1}(f = f_{tech})|$ can be computed thanks to Equation 3.33 and Equation 3.34. They should be respectively equal to a_{XIS2} and a_{XIS1} . Nonetheless, it is not the case: the values obtained by means of a least-squares method (that is to say the amplitudes observed in-flight) are higher than the values computed through the theoretical model. This difference has allowed to highlight a pure phase delay in the drag-free control loop, as illustrated in Figure 3.8.

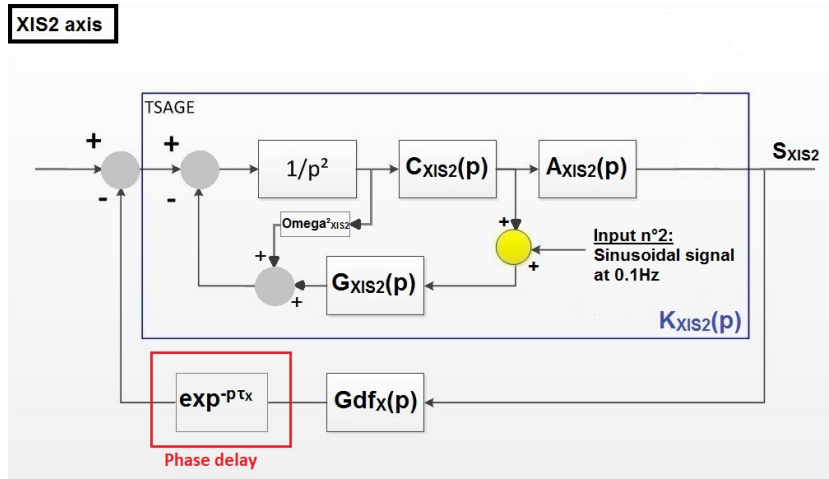


Figure 3.8: Illustration of the pure phase delay in the drag-free control loop - XIS2 sensor

The value of the delay τ_X is adjusted so that the amplitude values of the S_{XIS2} and S_{XIS1} outputs, computed through the theoretical model, match the amplitudes observed in-flight as closely as possible. This leads to a delay equal to $\tau_X = 0.60s$.

The same process is applied for the excitation along the Y-axis (section between 366s and 466s), and for the excitation along the Z-axis (section between 516s and 616s) to respectively estimate the phase delay in the drag-free control loop of the Y-axis (referred to as τ_Y), and of the Z-axis (referred to as τ_Z). This finally leads to

$\tau_Y = \tau_Z = 0.37\text{s}$ (values validated by the CNES responsible for the drag-free control block). The expressions for the transfer functions of the drag-free control loops thus need to be replaced by the following relation:

$$Gdf_i = \left[\frac{b_0 + b_1 p + b_2 p^2 + b_3 p^3}{a_0 + a_1 p + a_2 p^2 + a_3 p^3 + a_4 p^4} \right] \exp(-p\tau_i) \quad (3.35)$$

Where $i \in \{X, Y, Z\}$, and $a_0, a_1, a_2, a_3, b_0, b_1, b_2, b_3$ and b_4 represents the parameters of the transfer function previously evaluated in [subsection 3.2.3](#).

Now that the expressions for the drag-free control loop transfer function have been adjusted, the closed-loop transfer functions of the remaining linear axes can be derived:

□ Y_{IS2} :

$$S_{YIS2} = \left[\frac{A_{YIS2}(p)C_{YIS2}(p)}{D_{YIS2}(p)} \right] \left[\frac{p^2 + A_{XIS2}(p)C_{XIS2}(p)Gdf_X(p)}{D_{XIS2}(p)} \right] G_{XIS2}(p)\alpha_{XYIS2}E'_X \quad (3.36)$$

Leading to

$$|\alpha_{XYIS2}| = \left| \frac{D_{YIS2}(p)}{A_{YIS2}(p)C_{YIS2}(p)} \right| \left| \frac{D_{XIS2}(p)}{p^2 + A_{XIS2}(p)C_{XIS2}(p)Gdf_X(p)} \right| \left| \frac{S_{YIS2}(p)}{G_{XIS2}(p)E'_X} \right| \quad (3.37)$$

□ Y_{IS1} :

$$S_{YIS1} = K_{YIS1}(p) \left[\frac{\omega_{p_{XIS1}}^2 + C_{XIS1}(p)G_{XIS1}(p)}{p^2 + \omega_{p_{XIS1}}^2 + C_{XIS1}(p)G_{XIS1}(p)} \right] \left[\frac{A_{XIS2}(p)C_{XIS2}(p)G_{XIS2}(p)Gdf_X(p)}{D_{XIS2}(p)} \right] \alpha_{XYIS1}E'_X \\ - K_{YIS1}(p) \left[\frac{A_{YIS2}(p)C_{YIS2}(p)Gdf_Y(p)}{D_{YIS2}(p)} \right] \left[\frac{(p^2 + A_{XIS2}(p)C_{XIS2}(p)Gdf_X(p))G_{XIS2}(p)}{D_{XIS2}(p)} \right] \alpha_{XYIS2}E'_X \quad (3.38)$$

□ Z_{IS2} :

$$S_{ZIS2} = \left[\frac{A_{ZIS2}(p)C_{ZIS2}(p)}{D_{ZIS2}(p)} \right] \left[\frac{p^2 + A_{XIS2}(p)C_{XIS2}(p)Gdf_X(p)}{D_{XIS2}(p)} \right] G_{XIS2}(p)\alpha_{XZIS2}E'_X \quad (3.39)$$

Leading to

$$|\alpha_{XZIS2}| = \left| \frac{D_{ZIS2}(p)}{A_{ZIS2}(p)C_{ZIS2}(p)} \right| \left| \frac{D_{XIS2}(p)}{p^2 + A_{XIS2}(p)C_{XIS2}(p)Gdf_X(p)} \right| \left| \frac{S_{ZIS2}(p)}{G_{XIS2}(p)E'_X} \right| \quad (3.40)$$

□ Z_{IS1} :

$$S_{ZIS1} = K_{ZIS1}(p) \left[\frac{\omega_{p_{XIS1}}^2 + C_{XIS1}(p)G_{XIS1}(p)}{p^2 + \omega_{p_{XIS1}}^2 + C_{XIS1}(p)G_{XIS1}(p)} \right] \left[\frac{A_{XIS2}(p)C_{XIS2}(p)G_{XIS2}(p)Gdf_X(p)}{D_{XIS2}(p)} \right] \alpha_{XZIS1}E'_X \\ - K_{ZIS1}(p) \left[\frac{A_{ZIS2}(p)C_{ZIS2}(p)Gdf_Z(p)}{D_{ZIS2}(p)} \right] \left[\frac{(p^2 + A_{XIS2}(p)C_{XIS2}(p)Gdf_X(p))G_{XIS2}(p)}{D_{XIS2}(p)} \right] \alpha_{XZIS2}E'_X \quad (3.41)$$

It can be inferred from the relations derived above that a careful analysis of the accelerometer data during the technical session n°516 allows an estimation of the linear-to-linear coupling factor. The process used to evaluate these coupling factors is developed in [Table 3.8](#).

The same approach is applied for both the second section (excitation along the Y-axis) and the third section (excitation along the Z-axis) of the technical session n°516 to estimate the remaining linear-to-linear coupling factors. The results are gathered in [Table 3.9](#). In the same table, the differential linear-to-linear coupling factors are computed, and confronted with the values obtained with the processing of the calibration sessions. It is observed that the values computed are relevant with the ones obtained with the calibration sessions. The processing of the technical session n°516 has therefore allowed the derivation of the linear-to-linear coupling factors for the SUEP instrument.

Table 3.8: Algorithm used to extract the linear-to-linear coupling factors from the technical session n°516

Algorithm 2: Extraction of the linear-to-linear coupling factors from the first section of the technical session n°516	
Require:	The accelerometer data sets measured along the linear axes during the first section of the technical session n°516
Require:	The frequency of the signal applied to force an oscillation of the test-mass along the X-axis
1:	Fit the accelerometer data sets S_{XIS2} , S_{XIS1} , S_{YIS2} , S_{YIS1} , S_{ZIS2} and S_{ZIS1} with a sinusoidal function $a \sin(2\pi f_{cal/lin} t + \Phi) + b$ by means of a least-squares method.
2:	Compute $ \alpha_{XYIS2} $ thanks to Equation 3.37
	$ \alpha_{XYIS2} = \left \frac{p^2 + \omega_{pYIS2}^2 + C_{YIS2}(p)G_{YIS2}(p) + A_{YIS2}(p)C_{YIS2}(p)Gdf_Y(p)}{A_{YIS2}(p)C_{YIS2}(p)} \right \left \frac{p^2 + \omega_{pXIS2}^2 + C_{XIS2}(p)G_{XIS2}(p) + A_{XIS2}(p)C_{XIS2}(p)Gdf_X(p)}{p^2 + A_{XIS2}(p)C_{XIS2}(p)Gdf_X(p)} \right $ $\left \frac{\mathbf{a}_{YIS2}}{G_{XIS2}(p)E'_X} \right $
3:	if $\Phi_{YIS2} = \Phi_{XIS2} [2\pi]$ then
4:	$\alpha_{XYIS2} = \alpha_{XYIS2} $
5:	else
6:	$\alpha_{XYIS2} = - \alpha_{XYIS2} $
7:	end if
8:	The excitation frequency f_{tech} and the coupling factor α_{XYIS2} being known, using the Equation 3.38, find the value of α_{XYIS1} leading to: $ S_{YIS1}(f_{tech}, \alpha_{XYIS2}, \alpha_{XYIS1}) = \mathbf{a}_{YIS1}$ <p>The value found is equal to α_{XYIS1}</p>
9:	Apply the same process with the S_{ZIS2} and S_{ZIS1} outputs to estimate the coupling factors α_{XZIS2} and α_{XZIS1} .

Table 3.9: Processing of the technical session n°516: estimation of the linear-to-linear coupling factors and confrontation with the results obtained with the calibration sessions

Results from the Technical session n°516			Results from the Calibration sessions
Linear-to-linear coupling factor	Value	Differential (IS1-IS2)	Differential factor from the calibration sessions
α_{XYIS2}	-0,14963	0,17185	0.172 ± 0.024
α_{XYIS1}	0,02222		
α_{XZIS2}	-0,15748	0,22283	0.20 ± 0.03
α_{XZIS1}	0,06536		
α_{YXIS2}	-0,01046	$-3.2 \cdot 10^{-4}$	$[-5 \pm 6] \cdot 10^{-4}$
α_{YXIS1}	-0,01077		
α_{YZIS2}	0,01406	$6.43 \cdot 10^{-3}$	$[3 \pm 3] \cdot 10^{-3}$
α_{YZIS1}	0,02049		
α_{ZXIS2}	-0,02633	$2.6 \cdot 10^{-4}$	$[4 \pm 6] \cdot 10^{-4}$
α_{ZXIS1}	-0,02607		
α_{ZYIS2}	-0,01494	$-4.2 \cdot 10^{-4}$	$[-6 \pm 6] \cdot 10^{-4}$
α_{ZYIS1}	-0,01536		

A similar technical session realized with the SUREF instrument would lead to the estimation of the linear-to-linear coupling factors for the SUREF instrument. **Such a session has therefore been proposed to the scientific mission center and accepted.** It has been added to the mission scenario before the end of the MICROSCOPE mission.

The linear-to-linear coupling factors computed are an estimation of the real values, since the instrumental model used for the processing of the various sessions is a simplified linear model neglecting certain terms.

Indeed, the model used only took into account the couplings between the axis along which the sinusoid of specific frequency was applied, and the others. A more complex instrumental model taking into account all the linear-to-linear coupling factors will allow to improve the precision of the estimation. This is the purpose of the instrument simulator presented in the next section.

3.4. Design of an instrument simulator

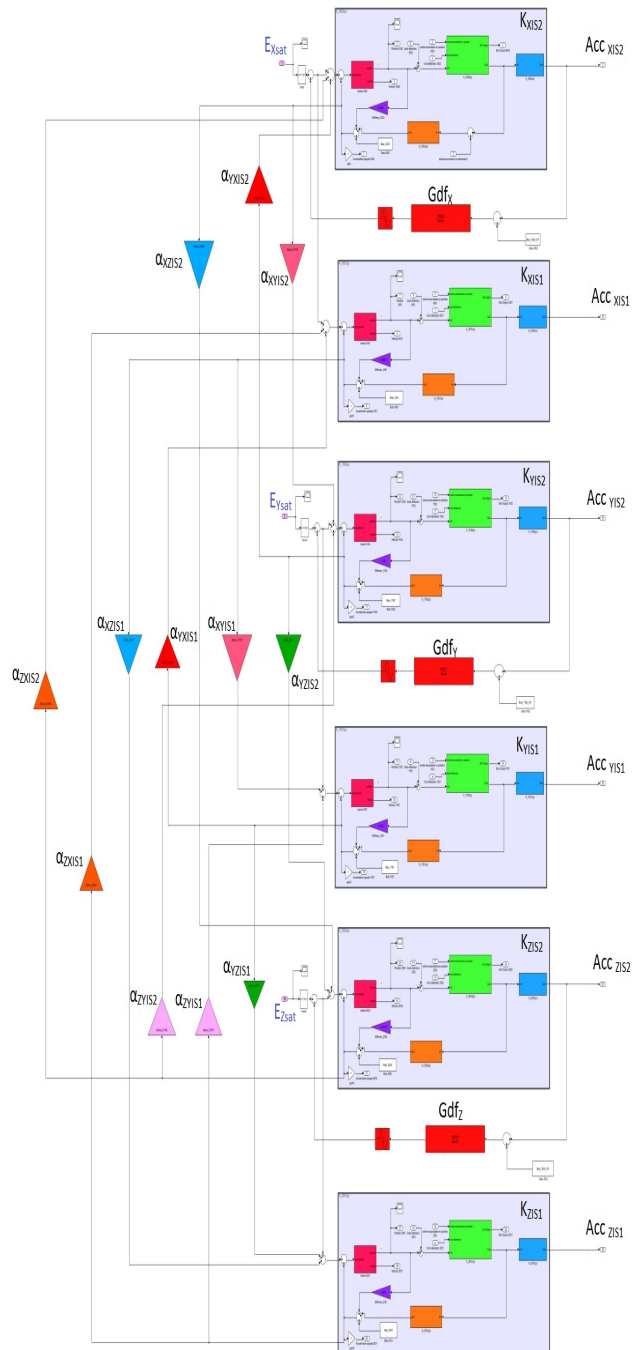


Figure 3.9: Illustration of the *Simulink* Simulator of the instrument

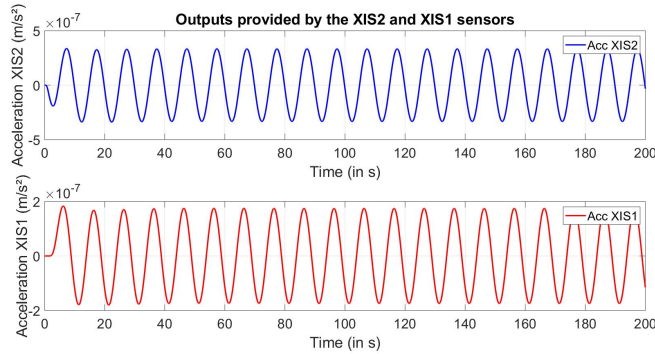
As mentioned at the end of the previous section, in the interest of clarity and simplicity, the instrumental model used so far only took into account the couplings between the axis along which the excitation signal was applied, and the others. This simplified model allowed a first estimation of the linear-to-linear coupling factors. In order to get closer to the real values, a more complex instrumental model, taking into account all the linear-to-linear coupling factors, needs to be designed: a *Simulink* simulator of the instrument is therefore developed, as illustrated on [Figure 3.9](#). *Simulink* is an add-on tool to *MATLAB* that provides an interactive, graphical environment for modeling, simulating, and analyzing dynamic systems. For modeling, *Simulink* provides a graphical user interface for building models as block diagrams. It therefore enables rapid construction of virtual prototypes to explore design concepts. This tool will thus allow to build an instrument simulator taking into account all the linear-to-linear coupling factors simultaneously.

The simulator simulates the behavior of the linear axes of the SUEP instrument. Each sensor of the accelerometer simulator is designed according to the model illustrated in [Figure 3.8](#). The control functions ($\mathbf{C}(\mathbf{p})$, $\mathbf{G}(\mathbf{p})$ and $\mathbf{A}(\mathbf{p})$) of each sensor have been detailed in [Appendix B](#). The drag-free control block is set to compensate the motion of the external test-mass (DFIS2). The linear-to-linear coupling factors are initialized with the values estimated in the previous section (as seen in [Table 3.9](#)).

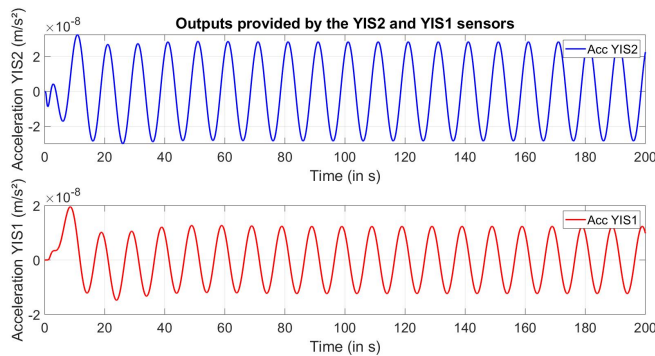
Three simulations are run with these first settings:

- First, a sinusoid of amplitude 0.148V and frequency $f_{tech} = 0.1\text{Hz}$ is applied in the instrument control loop to force an oscillation of the test-mass along the X-axis: $\mathbf{E}'_{\mathbf{X}}(\mathbf{t}) = \mathbf{0.148} \cdot \sin(2\pi(\mathbf{0.1})\mathbf{t})$
- Then, a sinusoid of amplitude 0.01V and frequency f_{tech} is induced in the satellite motion along the Y-axis: $\mathbf{E}'_{\mathbf{Y}}(\mathbf{t}) = \mathbf{0.01} \cdot \sin(2\pi(\mathbf{0.1})\mathbf{t})$
- Finally, a sinusoid of amplitude 0.01V and frequency f_{tech} is induced in the satellite motion along the Z-axis: $\mathbf{E}'_{\mathbf{Z}}(\mathbf{t}) = \mathbf{E}'_{\mathbf{Y}}(\mathbf{t}) = \mathbf{0.01} \cdot \sin(2\pi(\mathbf{0.1})\mathbf{t})$

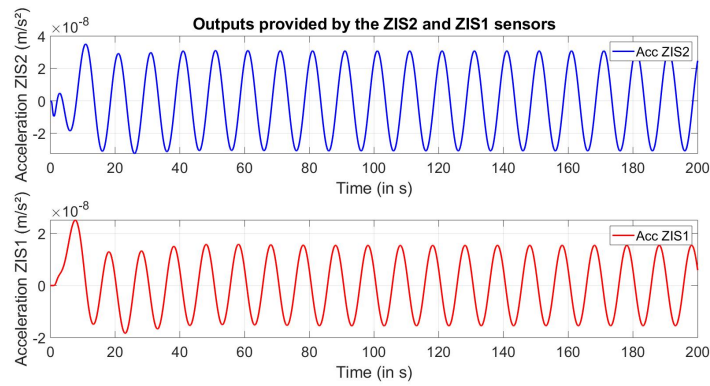
These three simulations attempt to reproduce the scenario realized during the technical session n°516. The outputs provided by each sensor of the instrument simulator for the first simulation are illustrated on [Figure 3.10](#). The first random oscillations observed on these figures correspond to the convergence time of the simulator. The outputs observed with the two other simulations are gathered in [Appendix D](#).



(a) XIS2 and XIS1 axes



(b) YIS2 and YIS1 axes



(c) ZIS2 and ZIS1 axes

Figure 3.10: Outputs provided by the instrument simulator for the first simulation (Excitation along the X-axis)

For each simulation, the amplitude of the acceleration measured by every sensor is computed by means of a least-squares method, and confronted with the values observed in-flight during the technical session n°516.

The results are gathered in Table 3.10.

Table 3.10: Results obtained with the instrument simulator - Linear-to-linear coupling factors initialized with the values computed in section 3.3

Excitation along the X-axis - Amplitude 0.148V - Frequency 0.1Hz		
Sensor	Amplitude obtained with the Simulator (m/s^2)	Amplitude obtained in-flight during the first section of the technical session n°516 (m/s^2)
XIS2	$3.330 \cdot 10^{-7}$	$3.349 \cdot 10^{-7}$
XIS1	$1.747 \cdot 10^{-7}$	$1.754 \cdot 10^{-7}$
YIS2	$2.84 \cdot 10^{-8}$	$2.86 \cdot 10^{-8}$
YIS1	$1.24 \cdot 10^{-8}$	$1.16 \cdot 10^{-8}$
ZIS2	$3.00 \cdot 10^{-8}$	$3.01 \cdot 10^{-8}$
ZIS1	$1.55 \cdot 10^{-8}$	$1.02 \cdot 10^{-8}$
Excitation along the Y-axis - Amplitude 0.01V - Frequency 0.1Hz		
Sensor	Amplitude obtained with the Simulator (m/s^2)	Amplitude obtained in-flight during the second section of the technical session n°516 (m/s^2)
YIS2	$1.937 \cdot 10^{-7}$	$1.931 \cdot 10^{-7}$
YIS1	$9.14 \cdot 10^{-8}$	$7.08 \cdot 10^{-8}$
XIS2	$1.8 \cdot 10^{-9}$	$1.7 \cdot 10^{-9}$
XIS1	$1.8 \cdot 10^{-9}$	$1.8 \cdot 10^{-9}$
ZIS2	$1.9 \cdot 10^{-9}$	$1.6 \cdot 10^{-9}$
ZIS1	$2.1 \cdot 10^{-9}$	$2.0 \cdot 10^{-9}$
Excitation along the Z-axis - Amplitude 0.01V - Frequency 0.1Hz		
Sensor	Amplitude obtained with the Simulator (m/s^2)	Amplitude obtained in-flight during the third section of the technical session n°516 (m/s^2)
ZIS2	$1.934 \cdot 10^{-7}$	$1.923 \cdot 10^{-7}$
ZIS1	$9.14 \cdot 10^{-8}$	$7.00 \cdot 10^{-8}$
XIS2	$4.4 \cdot 10^{-9}$	$4.3 \cdot 10^{-9}$
XIS1	$4.3 \cdot 10^{-9}$	$4.2 \cdot 10^{-9}$
YIS2	$1.0 \cdot 10^{-9}$	$1.7 \cdot 10^{-9}$
YIS1	$1.7 \cdot 10^{-9}$	$2.2 \cdot 10^{-9}$

As planned, with a more complex instrumental model, the values of the linear-to-linear coupling factors need to be adjusted so that the accelerations amplitudes obtained with the *Simulink* simulator get as close as possible to the values observed in-flight during the technical session n°516. The *Simulink Design Optimization* toolbox allows to adjust the parameters of a *Simulink* model in order to meet certain constraints. This feature will be of great interest in the linear-to-linear coupling factors optimization process developed in [Table 3.11](#).

Table 3.11: Algorithm used to adjust the values of the linear-to-linear coupling factors

Algorithm 3: Optimization of the linear-to-linear coupling factors
Require: The first estimates of the linear-to-linear coupling factors computed in section 3.3 to initialize the process
<ol style="list-style-type: none"> 1: Initialize the linear-to-linear coupling factors with the estimates computed in section 3.3. 2: The parameters α_{YXIS2}, α_{YXIS1}, α_{YZIS2}, α_{YZIS1}, α_{ZXIS2}, α_{ZXIS1}, α_{ZYSIS2} and α_{ZYSIS1} are fixed. The simulator is set so that an excitation signal $\mathbf{E}'_X(\mathbf{t})$ is applied in the instrument loop to force an oscillation of the test-mass along the X-axis. Use the <i>Simulink Design Optimization</i> to adjust the parameters α_{XYIS2}, α_{XYIS1}, α_{XZIS2} and α_{XZIS1} so that the accelerations amplitudes obtained with the simulator get as close as possible to the values observed in-flight during the first section of technical session n°516 (Excitation along the X-axis). 3: Update the values of the parameters α_{XYIS2}, α_{XYIS1}, α_{XZIS2} and α_{XZIS1}. 4: The parameters α_{XYIS2}, α_{XYIS1}, α_{XZIS2}, α_{XZIS1}, α_{ZXIS2}, α_{ZXIS1}, α_{ZYSIS2} and α_{ZYSIS1} are fixed. The simulator is set so that an excitation signal $\mathbf{E}'_Y(\mathbf{t})$ is applied in the instrument loop to force an oscillation of the test-mass along the Y-axis. Use the <i>Simulink Design Optimization</i> to adjust the parameters α_{YXIS2}, α_{YXIS1}, α_{YZIS2} and α_{YZIS1} so that the accelerations amplitudes obtained with the simulator get as close as possible to the values observed in-flight during the second section of technical session n°516 (Excitation along the Y-axis). 5: Update the values of the parameters α_{YXIS2}, α_{YXIS1}, α_{YZIS2} and α_{YZIS1}. 6: The parameters α_{XYIS2}, α_{XYIS1}, α_{XZIS2}, α_{XZIS1}, α_{YXIS2}, α_{YXIS1}, α_{YZIS2} and α_{YZIS1} are fixed. The simulator is set so that an excitation signal $\mathbf{E}'_Z(\mathbf{t})$ is applied in the instrument loop to force an oscillation of the test-mass along the Z-axis. Use the <i>Simulink Design Optimization</i> to adjust the parameters α_{ZXIS2}, α_{ZXIS1}, α_{ZYSIS2} and α_{ZYSIS1} so that the accelerations amplitudes obtained with the simulator get as close as possible to the values observed in-flight during the third section of technical session n°516 (Excitation along the Z-axis). 7: Update the values of the parameters α_{ZXIS2}, α_{ZXIS1}, α_{ZYSIS2} and α_{ZYSIS1}. 8: The steps 2 to 7 are repeated until convergence of the linear-to-linear coupling factors.

The values obtained with this approach are presented in [Table 3.12](#). The accelerations amplitudes provided by the simulator using the adjusted linear-to-linear coupling factors are shown in [Table 3.13](#) while the simulator outputs are gathered in [Appendix D](#).

As observed in [Table 3.13](#), the optimization process has allowed an improvement of the precision. Nonetheless, the accelerations amplitudes provided by the instrument simulator are still slightly different from the values measured in-flight throughout the technical session n°516. This can be explained by the simplifications used for the instrumental model: **the simulator neglected the electrical bias and the instrumental noise, but also and above all did not take into account the coupling between the linear and angular axes**. A simulator simulating the behavior of the six axes of the instrument, and considering both the coupling between the linear and angular axes, and the other perturbations mentioned would provide more accurate results. The work achieved so far has therefore paved the way for further research that would lead to an even more precise estimation of the instrument coupling factors.

Table 3.12: Adjusted linear-to-linear coupling factors provided by the optimization process

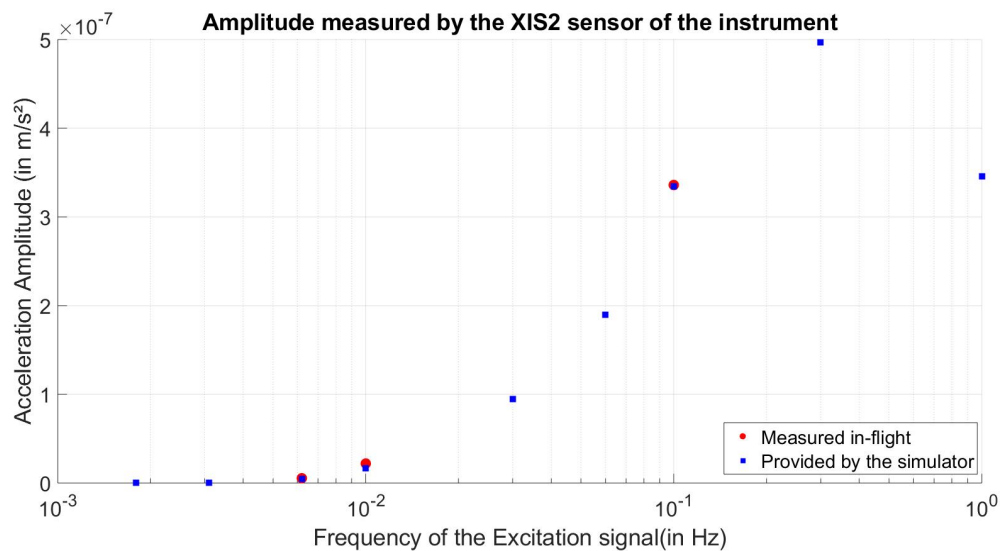
Linear-to-linear coupling factors	Estimated Value (section 3.3)	Adjusted Value
α_{XYIS2}	-0.14963	-0.15101
α_{XYIS1}	0.02222	0.02725
α_{XZIS2}	-0.15748	-0.15400
α_{XZIS1}	0.06536	0.03010
α_{YXIS2}	-0.01046	-0.01019
α_{YXIS1}	-0.01077	-0.01059
α_{YZIS2}	0.01406	0.01145
α_{YZIS1}	0.02049	0.01962
α_{ZXIS2}	-0.02633	-0.02647
α_{ZXIS1}	-0.02607	-0.02627
α_{ZYIS2}	-0.01494	-0.02120
α_{ZYIS1}	-0.01536	-0.02151

Table 3.13: Results obtained with the instrument simulator using the adjusted linear-to-linear coupling factors

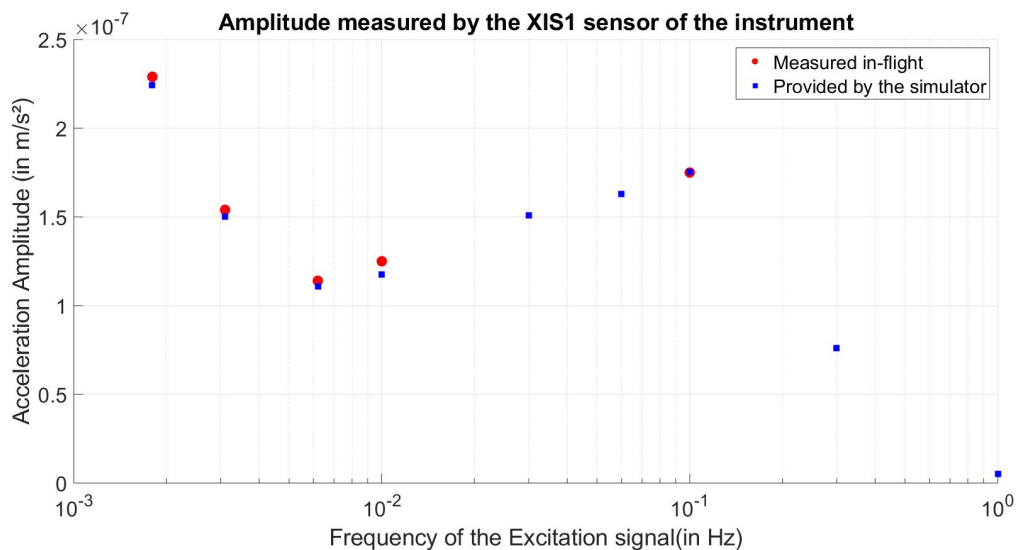
Excitation along the X-axis - Amplitude 0.148V - Frequency 0.1Hz			
Sensor	Amplitude measured in-flight during the first section of the technical session n°516 (m/s^2)	Amplitude obtained with the simulator using the coupling factors first estimates (m/s^2)	Amplitude obtained with the simulator using the adjusted coupling factors (m/s^2)
XIS2	$3.349 \cdot 10^{-7}$	$3.330 \cdot 10^{-7}$	$3.347 \cdot 10^{-7}$
XIS1	$1.754 \cdot 10^{-7}$	$1.747 \cdot 10^{-7}$	$1.750 \cdot 10^{-7}$
YIS2	$2.86 \cdot 10^{-8}$	$2.84 \cdot 10^{-8}$	$2.86 \cdot 10^{-8}$
YIS1	$1.16 \cdot 10^{-8}$	$1.24 \cdot 10^{-8}$	$1.21 \cdot 10^{-8}$
ZIS2	$3.01 \cdot 10^{-8}$	$3.00 \cdot 10^{-8}$	$3.01 \cdot 10^{-8}$
ZIS1	$1.02 \cdot 10^{-8}$	$1.55 \cdot 10^{-8}$	$1.34 \cdot 10^{-8}$
Excitation along the Y-axis - Amplitude 0.01V - Frequency 0.1Hz			
Sensor	Amplitude measured in-flight during the second section of the technical session n°516 (m/s^2)	Amplitude obtained with the simulator using the coupling factors first estimates (m/s^2)	Amplitude obtained with the simulator using the adjusted coupling factors (m/s^2)
YIS2	$1.931 \cdot 10^{-7}$	$1.937 \cdot 10^{-7}$	$1.930 \cdot 10^{-7}$
YIS1	$7.08 \cdot 10^{-8}$	$9.14 \cdot 10^{-8}$	$9.10 \cdot 10^{-8}$
XIS2	$1.7 \cdot 10^{-9}$	$1.8 \cdot 10^{-9}$	$1.7 \cdot 10^{-9}$
XIS1	$1.8 \cdot 10^{-9}$	$1.8 \cdot 10^{-9}$	$1.8 \cdot 10^{-9}$
ZIS2	$1.6 \cdot 10^{-9}$	$1.9 \cdot 10^{-9}$	$1.6 \cdot 10^{-9}$
ZIS1	$2.0 \cdot 10^{-9}$	$2.1 \cdot 10^{-9}$	$2.0 \cdot 10^{-9}$
Excitation along the Y-axis - Amplitude 0.01V - Frequency 0.1Hz			
Sensor	Amplitude measured in-flight during the third section of the technical session n°516 (m/s^2)	Amplitude obtained with the simulator using the coupling factors first estimates (m/s^2)	Amplitude obtained with the simulator using the adjusted coupling factors (m/s^2)
ZIS2	$1.923 \cdot 10^{-7}$	$1.934 \cdot 10^{-7}$	$1.930 \cdot 10^{-7}$
ZIS1	$7.00 \cdot 10^{-8}$	$9.14 \cdot 10^{-8}$	$9.11 \cdot 10^{-8}$
XIS2	$4.3 \cdot 10^{-9}$	$4.4 \cdot 10^{-9}$	$4.3 \cdot 10^{-9}$
XIS1	$4.2 \cdot 10^{-9}$	$4.3 \cdot 10^{-9}$	$4.3 \cdot 10^{-9}$
YIS2	$1.7 \cdot 10^{-9}$	$1.0 \cdot 10^{-9}$	$1.7 \cdot 10^{-9}$
YIS1	$2.2 \cdot 10^{-9}$	$1.7 \cdot 10^{-9}$	$2.4 \cdot 10^{-9}$

Nonetheless, as of now, the values computed represent a good estimation of the linear-to-linear coupling factors of the SUEP instrument, and the *Simulink* simulator designed can predict the amplitudes of the linear accelerations measured in-flight with a satisfactory accuracy.

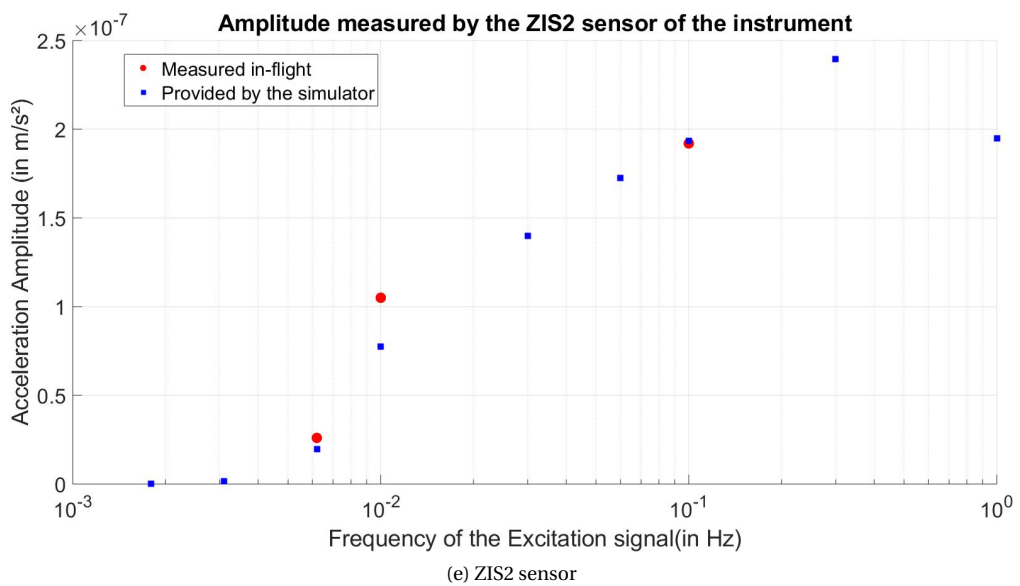
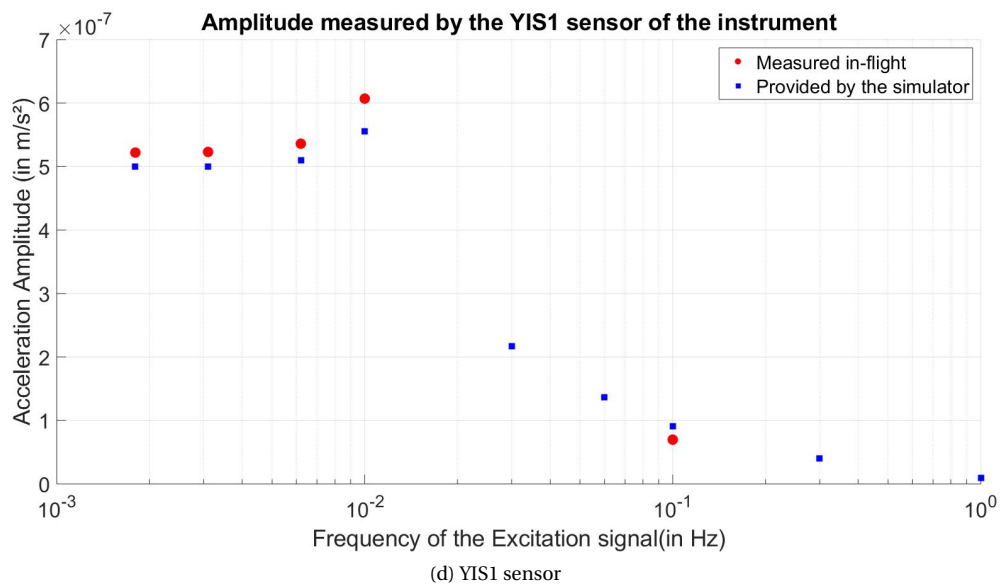
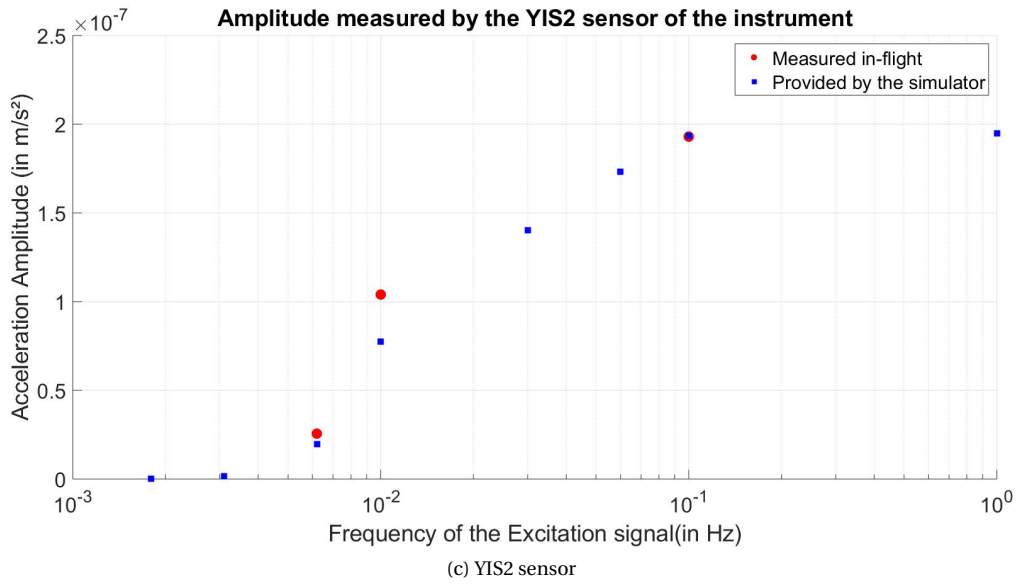
To illustrate this point, several simulations during which a sinusoid is applied in the instrument loop to force an oscillation of the test-mass along the X-axis are run. The frequency range of the excitation signal goes from 0.0018Hz to 1Hz. The accelerations amplitudes provided by each sensor of the simulator are then confronted with the amplitudes measured in-flight during dedicated mission phases. This is illustrated in [Figure 3.11](#). The values missing for the amplitudes measured in-flight will be completed through future research work.



(a) XIS2 sensor



(b) XIS1 sensor



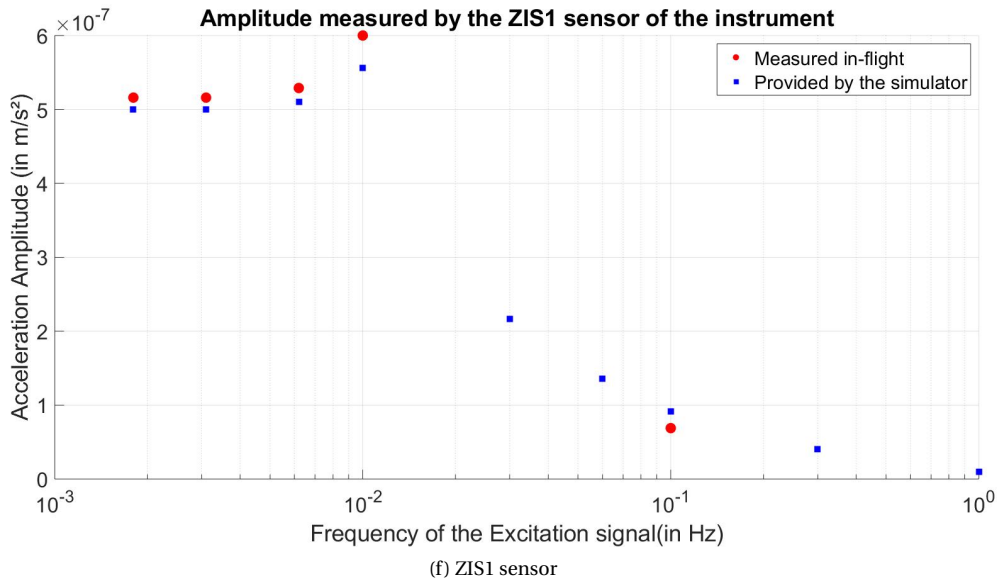


Figure 3.11: Confrontation between the amplitudes of the accelerations provided by each simulator sensor, and the values measured in-flight during dedicated mission phases

This chapter has investigated various ways to estimate the coupling between axes. In a first time, the processing of the various calibration sessions allowed an evaluation of the differential linear-to-linear coupling factors. Then, the careful analysis of a specific mission phase led to a first estimation of the linear-to-linear coupling factors of the SUEP instrument. The coupling factors of the SUREF instrument could be derived from a similar session realized with the SUREF instrument. Therefore, such a session may be added to the mission scenario before the end of the MICROSCOPE space mission. The first coupling factors estimates then underwent an optimization process based on a more complex instrumental model, in order to get closer to the real values. As the simulator designed can predict the amplitude of the linear accelerations measured in-flight with a satisfactory accuracy, it can be inferred that the adjusted values represent a good estimation of the linear-to-linear coupling factors of the SUEP instrument.

Nonetheless, the instrumental model used in the investigation process was based on a number of simplifications: it neglected the electrical bias and the instrumental noise, but also and above all did not take into account the coupling between the linear and angular axes. An instrumental model including both the couplings and the other perturbations mentioned would enhance the precision of the results. Therefore, the work achieved so far has paved the way for further research that would lead to an even more accurate estimation of the instrument coupling factors.

Thermal Sensitivity of the instrument

Contents

4.1 Thermal perturbations in the measurement process.	51
4.2 Thermal mission phases.	53
4.2.1 Presentation of the thermal mission phases	53
4.2.2 Exploitation of the thermal sessions in the investigation of the instrument thermal sensitivity	53

For each instrument, the components of both the Sensor Units (SU) and the Front-End Electronic Units (FEEU) require a steady thermal environment as well as a limited operating temperature range to ensure an optimal performance. The accelerometers performance is indeed highly sensitive to temperature variations. The thermal effects represent one of the main contribution to the systematic error perturbing the measurement process. The evaluation of the instrument thermal sensitivity is thus of significant importance in the improvement of the instrumental model. This is the purpose of this fourth chapter.

4.1. Thermal perturbations in the measurement process

As mentioned in [section 2.2](#), each SAGE instrument is composed of three units:

- The Sensor Unit (referred to as SU), composed by two concentric and coaxial cylindrical test-masses surrounded by four silica cores. The whole is disposed inside the same tight cage.
- The Front-End Electronic Unit (referred to as FEEU), containing the analogue electronics of the control loop. Each FEEU is associated to one SU and includes the capacitive sensors of the internal and external test-masses, the reference voltage sources, and the electronics generating the voltages applied to the surrounding electrodes.
- The Interface Control Unit (ICU), that hosts the digital laws controlling the motion of the two test-masses, and serves as the interface to the on-board computer.

The two Sensor Units are installed with the two Front-End electronic Units on plate, referred to as the Sensor Unit Mechanical Interface (SUMI), within a highly stabilized thermal environment named Payload Block, as illustrated on [Figure 4.1](#).

The accelerometers performance being highly sensitive to temperature variations, 6 temperature probes have been integrated into each SU, and 5 temperature probes have been integrated into each FEEU in order to carefully monitor the evolution of the thermal environment within the Payload block. Only two thermal transfer methods are possible in-flight: the conduction and the radiation (it is assumed that, at an orbital altitude of 700km, the convection is negligible). These transfers occur between the SU, the FEEU and the surrounding elements through interfaces such as the wiring or the SUMI.

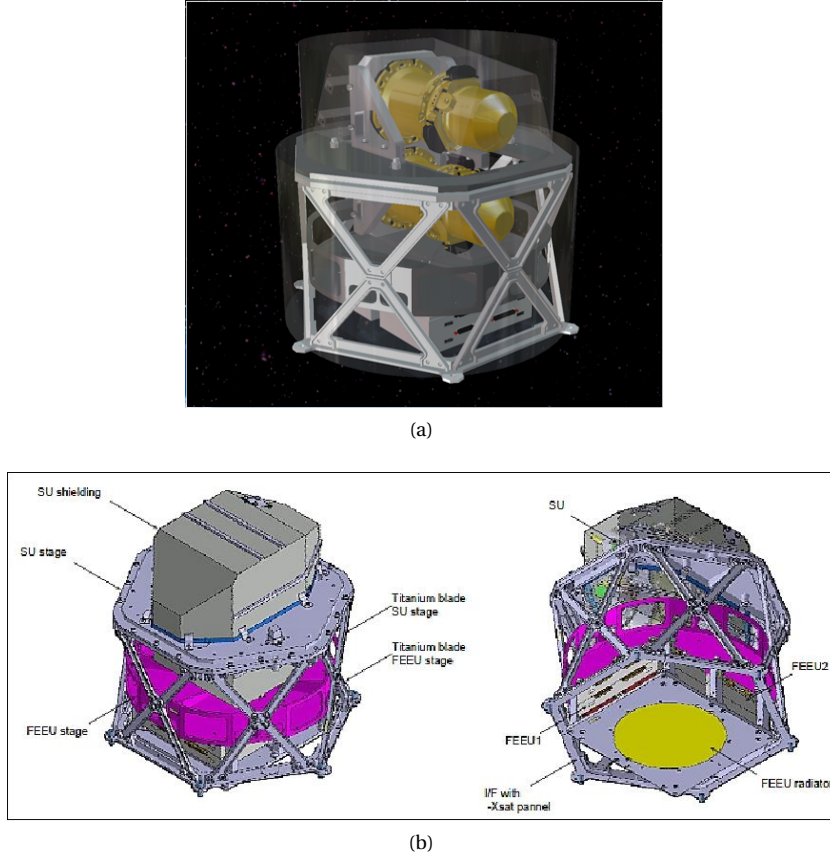


Figure 4.1: Illustration of the MICROSCOPE Payload Block [4]

It has been demonstrated in subsection 2.3.3 that the acceleration measurement along the X-axis, affected by all the systematic and stochastic errors can be defined as:

$$\Gamma_{meas,X} = b_{0X} + [A_X]\Gamma_{App,X} + Q_X + [C_X]\dot{Q}_X + n_X$$

Where $\Gamma_{App,X}$ denotes the electrostatic acceleration applied to the test-mass, $[A_X]$ represents the sensitivity matrix, $[C_X]$ corresponds to the coupling matrix, Q_X models the quadratic terms, and n_X is the instrumental noise. Although the sensitivity matrix can depend on the temperature, its thermal sensitivity is assumed to be negligible. Nonetheless, the electrical bias b_{0X} including all the parasitic constant terms, is temperature-dependent, as illustrated by the relation:

$$b_{0X} \approx B + \lambda(T_{SU} - \bar{T}) + \beta(T_{FEEU} - \bar{T}) \quad (4.1)$$

Where B represents the bias due to the perturbations other than temperature variations; λ and β respectively denote the SU and FEEU temperature sensitivity (expressed in $m \cdot s^{-2} \cdot K^{-1}$); \bar{T} is the mean temperature within the instrument. The temperature of the Sensor Unit T_{SU} is modelled by the average of the temperatures provided by two probes among the six integrated into the SU:

$$T_{SU} = \langle T_4, T_6 \rangle$$

T_i denotes the temperature provided by the i^{th} probe. The temperature of the Front-End Electronic Unit T_{FEEU} is assumed to be equal to the temperature provided by a specific probe integrated into the FEEU, referred to as the TRP probe (standing for Temperature Reference Point probe). The TRP probe is located at the interface between the FEEU and the SUMI:

$$T_{FEEU} = T_{TRP}$$

The impact of these thermal effects on the acceleration signal is:

$$\Gamma_X^{meas}(\text{therm}) = \lambda \Delta T_{SU} + \beta \Delta T_{FEEU} \quad (4.2)$$

The estimation of the thermal sensitivities λ and β are thus of significant importance in the improvement of the instrumental model. These parameters will be investigated in the next section.

4.2. Thermal mission phases

This section will be dedicated to the design of a process to estimate the thermal sensitivity of the SUEP and SUREF instruments.

4.2.1. Presentation of the thermal mission phases

In order to investigate the thermal sensitivity of the SUEP and SUREF instruments, some specific mission phases, referred to as thermal sessions, have been integrated to the mission scenario. During these sessions, thermistors located within the Payload Block are activated in order to apply thermal fluctuations at f_{EP} either to the SU baseplate (session referred to as **SU thermal session**), or to the electronic interface (session referred to as **FEEU thermal session**). Throughout a SU thermal session, the Sensor Unit temperature T_{SU} varies while the FEEU temperature fluctuations ΔT_{FEEU} remain relatively negligible, as illustrated in Figure 4.2. On the contrary, throughout a FEEU thermal session, the Front-End Electronic Unit temperature T_{FEEU} varies while the SU temperature fluctuations ΔT_{SU} remain relatively negligible, as illustrated in Figure 4.3.

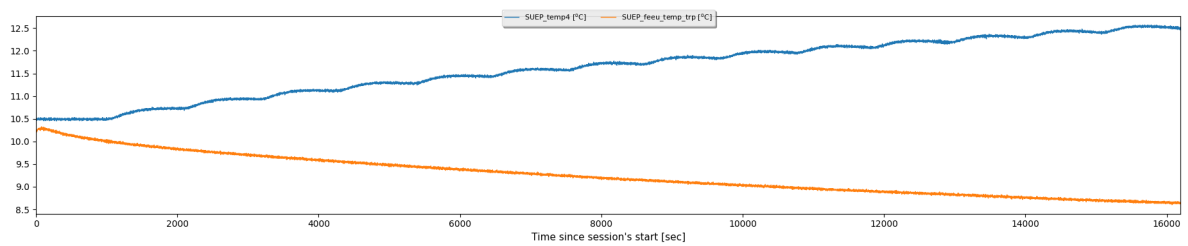


Figure 4.2: Evolution of both the SU (in blue) and the FEEU (in orange) temperatures throughout a SU thermal session realized with the SUEP instrument

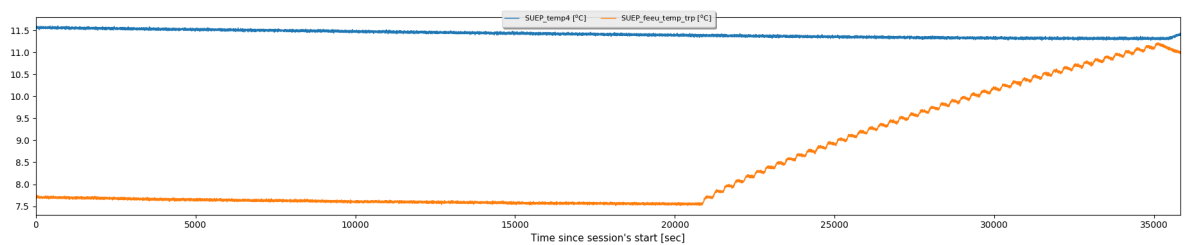


Figure 4.3: Evolution of both the SU (in blue) and the FEEU (in orange) temperatures throughout a FEEU thermal session realized with the SUEP instrument

The thermal sensitivity of the instrument is modelled by the ratio between the acceleration variation along the X-axis and the temperature variation. It can therefore be inferred that the careful processing of the SU and FEEU thermal sessions will lead to the estimation of both the SU temperature sensitivity λ , and the FEEU temperature sensitivity β . Nonetheless, only the SU thermal sessions have been analyzed through this research work, and consequently, only the λ parameter will be evaluated here. The investigation process is developed in the next subsection.

4.2.2. Exploitation of the thermal sessions in the investigation of the instrument thermal sensitivity

As specified in the previous subsection, the thermal sensitivity of the instrument is modelled by the ratio between the acceleration variation along the X-axis and the temperature variation. The acceleration data is sampled at 4Hz, whereas the temperature data is sampled at 1Hz. The temperature data has therefore been interpolated in order to oversample the signal at 4Hz.

Then, a 2nd order Butterworth low-pass filter with a cut-off frequency $f_c = 5 \cdot 10^{-2}$ Hz has been applied to both the acceleration and the temperature data in order to reduce the noise perturbing the signal:

$$H_{Butterworth}(p) = \frac{G_0}{\left(\left(\frac{p}{\omega_c} \right)^2 + 1.4142 \left(\frac{p}{\omega_c} \right) + 1 \right)}$$

Where $G_0 = 1$ and $\omega_c = 2\pi f_c$.

Previous research work [13] has allowed to demonstrate that the thermal transients could be modelled with satisfactory precision by the following function:

$$f(t) = A(1 - \exp^{-Bt})(1 - \exp^{-Ct}) + D$$

Where A, B, C and D denote the parameters to be determined.

The investigation process used to estimate either the SU temperature sensitivity λ (in case of a SU thermal session), or the FEEU temperature sensitivity β (in case of a FEEU thermal session) is developed in Table 4.1.

Table 4.1: Algorithm used to extract the instrument thermal sensitivity from the thermal sessions

Algorithm 4: Extraction of either the SU or the FEEU temperature sensitivity from the mission thermal sessions	
Require:	The accelerometer data sets measured along the X-axis during the thermal session
Require:	The SU temperature data set (in case of a SU thermal session) or the FEEU temperature data set (in case of a FEEU thermal session), oversampled at 4Hz
1:	Fit the accelerometer data sets S_{XIS1} and S_{XIS2} as well as the temperature data set with a function $A(1 - \exp^{-Bt})(1 - \exp^{-Ct}) + D$ by means of a least-squares method. This process has drawbacks because it requires a fit of four variables (A,B,C and D) for each data set whereas only the value of A will be used.
2:	if SU thermal session then
5:	$\lambda_{IS1} = \frac{A_{XIS1}}{A_{T_{SU}}}$ and $\lambda_{IS2} = \frac{A_{XIS2}}{A_{T_{SU}}}$ ΔA_{XIS1} , ΔA_{XIS2} and $\Delta A_{T_{SU}}$ denote the error made on the estimation of the parameters A_{XIS1} , A_{XIS2} and $A_{T_{SU}}$. The absolute uncertainty on the derived thermal sensitivities λ_{IS1} and λ_{IS2} can therefore be expressed as: $\Delta \lambda_{IS1} = \frac{\Delta A_{XIS1}}{A_{T_{SU}}} + \frac{A_{XIS1}}{A_{T_{SU}}^2} \Delta A_{T_{SU}}$ and $\Delta \lambda_{IS2} = \frac{\Delta A_{XIS2}}{A_{T_{SU}}} + \frac{A_{XIS2}}{A_{T_{SU}}^2} \Delta A_{T_{SU}}$
6:	else if FEEU thermal session then
7:	$\beta_{IS1} = \frac{A_{XIS1}}{A_{T_{FEEU}}}$ and $\beta_{IS2} = \frac{A_{XIS2}}{A_{T_{FEEU}}}$ ΔA_{XIS1} , ΔA_{XIS2} and $\Delta A_{T_{FEEU}}$ denote the error made on the estimation of the parameters A_{XIS1} , A_{XIS2} and $A_{T_{FEEU}}$. The absolute uncertainty on the derived thermal sensitivities β_{IS1} and β_{IS2} can therefore be expressed as: $\Delta \beta_{IS1} = \frac{\Delta A_{XIS1}}{A_{T_{FEEU}}} + \frac{A_{XIS1}}{A_{T_{FEEU}}^2} \Delta A_{T_{FEEU}}$ and $\Delta \beta_{IS2} = \frac{\Delta A_{XIS2}}{A_{T_{FEEU}}} + \frac{A_{XIS2}}{A_{T_{FEEU}}^2} \Delta A_{T_{FEEU}}$

As mentioned in the previous subsection, only the SU thermal sessions have been analyzed through this research work, and consequently, only the λ parameter will be evaluated here. The results of the investigation process are gathered in Table 4.2 and confronted with the SU temperature sensitivity theoretical values.

As observed on Table 4.2, the evaluated SU temperature sensitivities are more than 3 orders of magnitude larger than expected. Such values are way too high to be due to the radiometer effect or radiation pressure and must therefore result from another source. As previously stated, the impact of the thermal fluctuations on the acceleration signal is equal to $\Gamma_X^{meas}(\text{therm}) = \lambda \Delta T_{SU} + \beta \Delta T_{FEEU}$. Therefore, further research on the FEEU temperature sensitivity β and on the FEEU and SU temperature variations during an EP test session will

Table 4.2: Processing of the SU thermal session and estimation of the SU temperature sensitivity λ

Instrument	SU Temperature sensitivity	Theoretical Value (m/s ² /K)	Estimated Value (m/s ² /K)	Absolute uncertainty (m/s ² /K)
SUEP	λ_{IS2}	$2.78 \cdot 10^{-12}$	$1.71 \cdot 10^{-8}$	$2.35 \cdot 10^{-10}$
	λ_{IS1}	$2.55 \cdot 10^{-13}$	$5.8 \cdot 10^{-9}$	$7.66 \cdot 10^{-10}$
SUREF	λ_{IS2}	$1.56 \cdot 10^{-12}$	$1.7 \cdot 10^{-9}$	$1.84 \cdot 10^{-10}$
	λ_{IS1}	$2.30 \cdot 10^{-13}$	$3.0 \cdot 10^{-9}$	$1.34 \cdot 10^{-10}$

allow to decide whether the conservative upper limit used for the thermal systematic error can be lowered, and thus lead to further improve the instrumental model.

This chapter represents the first steps towards more in-depth investigations of the instrument thermal sensitivity. A process to extract both the SU and FEEU temperature sensitivity from the thermal mission sessions has been designed, and led to an evaluation of the parameter λ more than 3 orders of magnitude larger than expected. This chapter has therefore paved the way for further research work on both the FEEU temperature sensitivity β , and on the FEEU and SU temperature fluctuations during an EP test session, that would allow to decide whether the conservative upper limit used for the thermal systematic error can be lowered, leading to an enhanced instrumental model.

Chapter 5

Conclusion and prospects

The MICROSCOPE space mission aims at testing the equivalence principle in space with an unrivalled precision of 10^{-15} (a gain of two order of magnitude compared to the current experiment set up on Earth). The success of the mission relies on a thorough and careful data analysis to point out a possible signal of a WEP violation among time variations observed in the data caused by other physical phenomena, such as perturbations due to the instrument imperfections. Some of the perturbations, such as small misalignments in the satellite design, can be accurately modeled and corrected; some other perturbations require further research to be accurately estimated, and could therefore limit the accuracy of the MICROSCOPE experiment. This Master Thesis work has investigated two of these perturbations: the coupling between axes, and the instrument thermal sensitivity.

The [chapter 3](#) has explored various ways to evaluate the coupling between axes through a simplified model, leading eventually to a good estimation of the linear-to-linear coupling factors of the SUEP instrument. Throughout [chapter 4](#), a process to extract the instrument thermal sensitivity from specific mission phases, referred to as thermal sessions, has been designed, leading to a first estimation of the SU temperature sensitivity more than 3 orders of magnitude larger than expected.

The work carried out during this Master Thesis Project nonetheless only represent the first steps towards more in-depth investigations. Additional mission sessions are needed to compute the coupling factors of the SUREF instrument. Moreover, a more complex model taking into account the coupling between the linear and the angular axes would enhance the precision of the results. Regarding the instrument thermal sensitivity, a more in-depth exploration of both the FEEU temperature sensitivity and the FEEU and SU temperature variations during an EP test session would allow to decide whether the conservative upper limit used for the thermal systematic error can be lowered, and also, to find out the source involving the large value of the SU thermal sensitivity. In a nutshell, this Master thesis Project has paved the way for further research work that would lead to an even more accurate instrumental model.

Bibliography

- [1] RELATIVITY: THE SPECIAL AND THE GENERAL THEORY / Penguin Classics, 2006. *Scientific American*, 295:97, 2006.
- [2] MICROSCOPE Attitude and Orbit Control System. <https://microscope.cnes.fr/fr/MICROSCOPE/Fr/scaa.htm/>, July 2014.
- [3] MYRIADE CNES Micro-Satellite Program. https://myriade.cnes.fr/fr/MYRIADE/Fr/GP_plateforme.htm/, October 2014.
- [4] SAGE instrument developed by ONERA. <https://microscope.onera.fr/instrument/>, 2014.
- [5] B. P. Abbott, R. Abbott, T. D. Abbott, M. R. Abernathy, and A. I. Acernese. Observation of gravitational waves from a binary black hole merger. *Phys. Rev. Lett.*, 116:061102, Feb 2016. doi: 10.1103/PhysRevLett.116.061102. URL <https://link.aps.org/doi/10.1103/PhysRevLett.116.061102>.
- [6] B. P. Abbott, R. Abbott, T. D. Abbott, M. R. Abernathy, F. Acernese, K. Ackley, C. Adams, T. Adams, P. Addesso, R. X. Adhikari, and et al. Observation of Gravitational Waves from a Binary Black Hole Merger. *Physical Review Letters*, 116(6):061102, February 2016. doi: 10.1103/PhysRevLett.116.061102.
- [7] Quentin Baghi. *Optimization of the data analysis of the MICROSCOPE space mission for the test of the equivalence principle and other applications*. PhD thesis, PSL Research University, October 2016.
- [8] J.M. Bird. *Einstein's Theories of Relativity and Gravitation*. Scientific American Publishing Company, 1921. URL <https://books.google.fr/books?id=CyUQAAAAAYAAJ>.
- [9] V. B. Braginskii and V. I. Panov. Verification of the Equivalence of Inertial and Gravitational Mass. *Soviet Journal of Experimental and Theoretical Physics*, 34:463, 1972.
- [10] S. M. Carroll. *Spacetime and geometry. An introduction to general relativity*. 2004.
- [11] Thibault Damour. Testing the equivalence principle: why and how? *Classical and Quantum Gravity*, 13 (11A):A33, 1996. URL <http://stacks.iop.org/0264-9381/13/i=11A/a=005>.
- [12] Thibault Damour. Questioning the equivalence principle. *Comptes Rendus de l'Académie des Sciences - Series IV - Physics*, 2(9):1249 – 1256, 2001. ISSN 1296-2147. doi: [https://doi.org/10.1016/S1296-2147\(01\)01272-0](https://doi.org/10.1016/S1296-2147(01)01272-0). URL <http://www.sciencedirect.com/science/article/pii/S1296214701012720>.
- [13] Océane Dhuicque. *Analyse des données de la mission microscope : Détermination de la sensibilité thermique de l'instrument*. Rapport de stage, Ecole Polytechnique de l'Université François Rabelais de Tours, Tours, France, 2018.
- [14] C.W.F. Everitt, T. Damour, K. Nordtvedt, and R. Reinhard. Historical perspective on testing the equivalence principle. *Advances in Space Research*, 32(7):1297 – 1300, 2003. ISSN 0273-1177. doi: [https://doi.org/10.1016/S0273-1177\(03\)90335-8](https://doi.org/10.1016/S0273-1177(03)90335-8). URL <http://www.sciencedirect.com/science/article/pii/S0273117703903358>. Fundamental Physics in Space.
- [15] Emeline GUIU. *Calibration for the MICROSCOPE space mission: performance optimization*. PhD thesis, Université de Nantes, September 2007.
- [16] Jens H. Gundlach, Stephan Schlamminger, and Todd Wagner. Laboratory tests of the equivalence principle at the university of washington. *Space Science Reviews*, 148(1):201–216, Dec 2009. ISSN 1572-9672. doi: 10.1007/s11214-009-9609-3. URL <https://doi.org/10.1007/s11214-009-9609-3>.
- [17] E. Hardy, G. Metris, M. Santos Rodrigues, P. Touboul, R. Chhun, Q. Baghi, and J. Berge. Scientific data processing for the MICROSCOPE space experiment. In *40th COSPAR Scientific Assembly*, volume 40 of *COSPAR Meeting*, 2014.

- [18] Emilie Hardy. *Experimental procedures and data analysis for the MICROSCOPE space mission*. PhD thesis, Ecole doctorale Astronomie et Astrophysique d'Ile de France, September 2013.
- [19] M. P. Haugan and C. Lämmerzahl. Principles of Equivalence: Their Role in Gravitation Physics and Experiments That Test Them. In C. Lämmerzahl, C. W. F. Everitt, and F. W. Hehl, editors, *Gyros, Clocks, Interferometers ...: Testing Relativistic Gravity in Space*, volume 562 of *Lecture Notes in Physics*, Berlin Springer Verlag, page 195, 2001. doi: 10.1007/3-540-40988-2_10.
- [20] Stephen Hawking and Roger Penrose. *The Nature of Space and Time (New in Paper)*. Princeton University Press, 1996. ISBN 9780691145709. URL <http://www.jstor.org/stable/j.ctt7szq2>.
- [21] Danya Hudson. *Experimental and Theoretical Analysis of the Inertial Sensor Prototype for the MICROSCOPE in-orbit test of the Equivalence Principle*. PhD thesis, Ecole doctorale Astronomie et Astrophysique d'Ile de France, December 2007.
- [22] T. W. Murphy, Jr., E. G. Adelberger, J. B. R. Battat, C. D. Hoyle, N. H. Johnson, R. J. McMillan, C. W. Stubbs, and H. E. Swanson. APOLLO: millimeter lunar laser ranging. *Classical and Quantum Gravity*, 29(18):184005, September 2012. doi: 10.1088/0264-9381/29/18/184005.
- [23] S. Pireaux and J.-P. Rozelot. Solar quadrupole moment and purely relativistic gravitation contributions to mercury's perihelion advance. *Astrophysics and Space Science*, 284(4):1159–1194, Jun 2003. ISSN 1572-946X. doi: 10.1023/A:1023673227013. URL <https://doi.org/10.1023/A:1023673227013>.
- [24] J. Polchinski. *String Theory*. String Theory 2 Volume Hardback Set. Cambridge University Press, 2001. ISBN 9780521633031. URL <https://books.google.fr/books?id=54DGYyNAjacC>.
- [25] R. V. Pound and G. A. Rebka. Gravitational red-shift in nuclear resonance. *Phys. Rev. Lett.*, 3:439–441, Nov 1959. doi: 10.1103/PhysRevLett.3.439. URL <https://link.aps.org/doi/10.1103/PhysRevLett.3.439>.
- [26] Adam G. Riess, Alexei V. Filippenko, Peter Challis, Alejandro Clocchiatti, Alan Diercks, Peter M. Garnavich, Ron L. Gilliland, Craig J. Hogan, Saurabh Jha, Robert P. Kirshner, B. Leibundgut, M. M. Phillips, David Reiss, Brian P. Schmidt, Robert A. Schommer, R. Chris Smith, J. Spyromilio, Christopher Stubbs, Nicholas B. Suntzeff, and John Tonry. Observational evidence from supernovae for an accelerating universe and a cosmological constant. *The Astronomical Journal*, 116(3):1009, 1998. URL <http://stacks.iop.org/1538-3881/116/i=3/a=1009>.
- [27] P. G. Roll, R. Krotkov, and R. H. Dicke. The equivalence of inertial and passive gravitational mass. *Annals of Physics*, 26:442–517, February 1964. doi: 10.1016/0003-4916(64)90259-3.
- [28] P. Touboul, G. Métris, V. Lebat, and A. Robert. The MICROSCOPE experiment, ready for the in-orbit test of the equivalence principle. *Classical and Quantum Gravity*, 29(18):184010, September 2012. doi: 10.1088/0264-9381/29/18/184010.
- [29] P. Touboul, G. Métris, M. Rodrigues, Y. André, Q. Baghi, J. Bergé, D. Boulanger, S. Bremer, P. Carle, R. Chhun, B. Christophe, V. Cipolla, T. Damour, P. Danto, H. Dittus, P. Fayet, B. Foulon, C. Gageant, P.-Y. Guidotti, D. Hagedorn, E. Hardy, P.-A. Huynh, H. Inchauspe, P. Kayser, S. Lala, C. Lämmerzahl, V. Lebat, P. Leseur, F. Liorzou, M. List, F. Löffler, I. Panet, B. Pouilloux, P. Prieur, A. Rebray, S. Reynaud, B. Rievers, A. Robert, H. Selig, L. Serron, T. Sumner, N. Tanguy, and P. Visser. MICROSCOPE Mission: First Results of a Space Test of the Equivalence Principle. *Physical Review Letters*, 119(23):231101, December 2017. doi: 10.1103/PhysRevLett.119.231101.
- [30] T. Van Helleputte, E. Doornbos, and P. Visser. CHAMP and GRACE accelerometer calibration by GPS-based orbit determination. *Advances in Space Research*, 43:1890–1896, June 2009. doi: 10.1016/j.asr.2009.02.017.
- [31] T. A. Wagner. *Rotating Torsion Balance Tests of the Weak Equivalence Principle*. PhD thesis, University of Washington, 2014.
- [32] C. M. Will. The Confrontation between General Relativity and Experiment. *Living Reviews in Relativity*, 17:4, June 2014. doi: 10.12942/lrr-2014-4.

-
- [33] Clifford M. Will. The confrontation between general relativity and experiment. *Living Reviews in Relativity*, 9(1):3, Mar 2006. ISSN 1433-8351. doi: 10.12942/lrr-2006-3. URL <https://doi.org/10.12942/lrr-2006-3>.
- [34] J. G. Williams, S. G. Turyshev, and D. H. Boggs. Lunar Laser Ranging Tests of the Equivalence Principle with the Earth and Moon. *International Journal of Modern Physics D*, 18:1129–1175, 2009. doi: 10.1142/S021827180901500X.
- [35] J. G. Williams, S. G. Turyshev, and D. H. Boggs. Lunar laser ranging tests of the equivalence principle. *Classical and Quantum Gravity*, 29(18):184004, September 2012. doi: 10.1088/0264-9381/29/18/184004.
- [36] J. G. Williams, S. G. Turyshev, and D. H. Boggs. Lunar laser ranging tests of the equivalence principle. *Classical and Quantum Gravity*, 29(18):184004, September 2012. doi: 10.1088/0264-9381/29/18/184004.

Chapter A

Anti-Aliasing Filter

This appendix will present the anti-aliasing filter used in the A block of the instrument loop.

The anti-aliasing filter is used to restrict the bandwidth of a signal in order to satisfy the Nyquist sampling theorem stated below.

Nyquist Sampling Theorem. *A bandlimited continuous-time signal can be sampled and perfectly reconstructed from its samples only if the waveform is sampled over twice as fast as its highest frequency component. In other words, in order to perfectly reconstruct a signal with spectrum between 0 and f_{max} , the sampling frequency must be greater than $2f_{max}$, referred to as the Nyquist frequency.*

When selecting a filter, one should provide a cutoff frequency allowing to remove unwanted signals from the input or at least attenuate them so that they do not affect the circuit. An ideal anti-aliasing filter should have a "brick-wall" response, as illustrated in [Figure A.1](#), corresponding to an infinite quality factor Q . Nonetheless, such a configuration is impossible in practice. A higher value of Q comes with a more complex filter design and therefore, high quality factors can lead to filter instabilities and self-oscillation at the desired corner frequency.

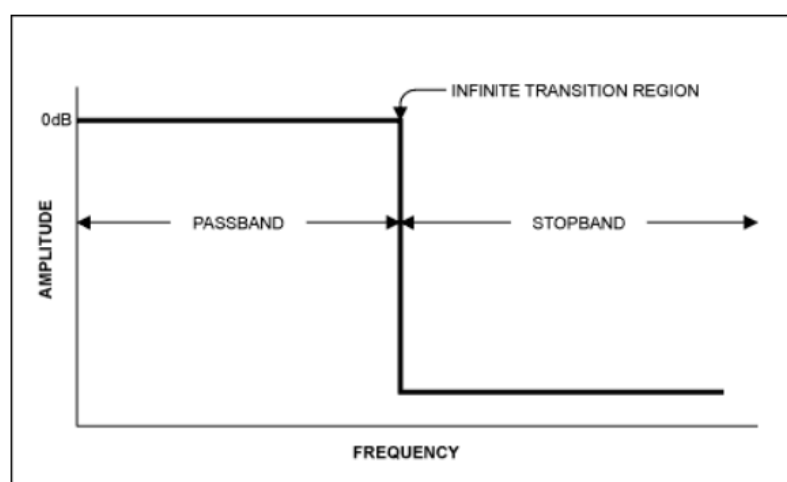


Figure A.1: Gain diagram of an ideal anti-aliasing filter

Among the four basic filter types (Elliptic, Chebyshev, Butterworth and Bessel), the filter selected for the

instrument loop is a 5th order Butterworth low-pass filter, with a cut-off frequency $f_c = 2\text{Hz}$:

$$H_{\text{Butterworth}}(p) = \frac{G_0}{\left[\left(\frac{p}{\omega_c}\right) + 1\right] \left[\left(\frac{p}{\omega_c}\right)^2 + 0.6180\left(\frac{p}{\omega_c}\right) + 1\right] \left[\left(\frac{p}{\omega_c}\right)^2 + 1.6180\left(\frac{p}{\omega_c}\right) + 1\right]}$$

Where $G_0 = 1$ and $\omega_c = 2\pi f_c$. The Bode diagram of the selected filter is presented on Figure A.2.

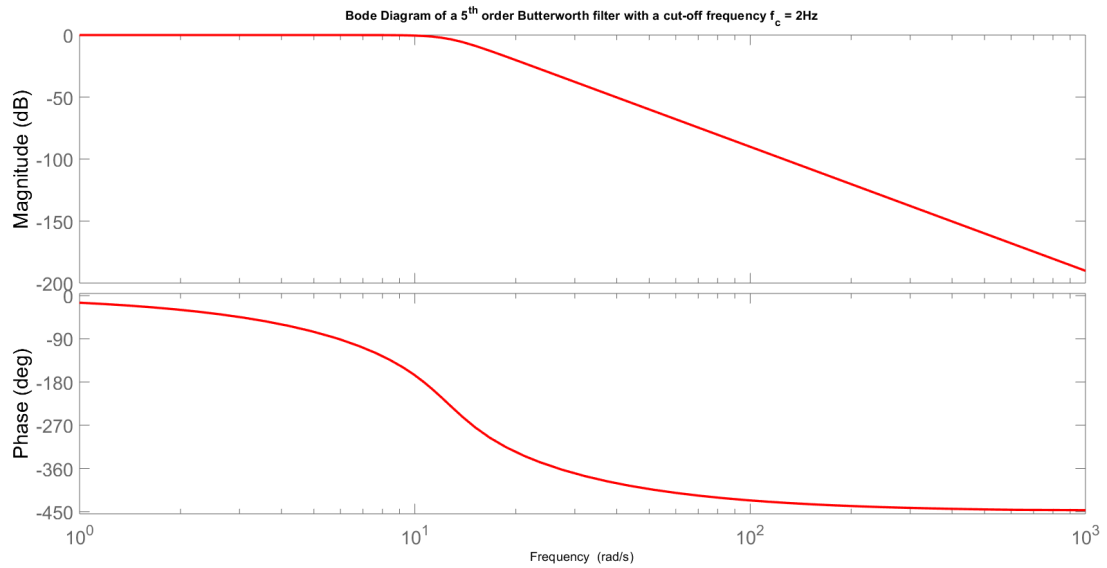


Figure A.2: Bode diagram of a 5th Butterworth filter with a cut-off frequency $f_c = 2\text{Hz}$

The Butterworth filter has been chosen because it has the flattest frequency response in the passband region. In other words, it provides the least attenuation over the desired frequency range.

Chapter B

Control Functions Parameters

In this appendix, the various parameter values for the C(p), G(p) and A(p) block control functions will be detailed. As a reminder, the general expressions of the concerned block control functions are specified below:

$$\mathbf{C}(p) = \left[\frac{G_{det}G_{fm}}{1 + \frac{p}{2\pi F_{CutOffDet}}} \right] \left[\frac{K_p}{1 + \frac{\sqrt{2}}{2\pi F_{pre}} p + \left(\frac{p}{2\pi F_{pre}}\right)^2} \right] \left[\frac{\frac{p}{2\pi F_{D1}}}{\left(1 + \frac{p}{2\pi F_{D2}}\right) \cdot \left(1 + \frac{p}{2\pi F_C}\right)} + \frac{F_{D1} + F_I}{F_{D1}} + \frac{2\pi F_I}{p} \right] \left[\frac{1}{1 + \frac{p}{2\pi F_{post}}} \right]$$

$$\mathbf{G}(p) = \frac{G_{DVA}}{1 + \frac{p}{2\pi F_{CutOffDVA}}} \cdot G_{actuation}$$

$$\mathbf{A}(p) = G_{DVA} \cdot G_{actuation} \cdot H_{Butterworth}(p)$$

The values of the parameters introduced through these relations are gathered in [Table B.1](#), [Table B.2](#) and [Table B.3](#), for both instruments (SUEP and SUREF), and both test-masses (internal and external).

Table B.1: Values of the control functions parameters for the internal test-mass of both the SUEP and the SUREF instrument

Internal Test-mass IS1 - SUEP and SUREF instruments				
Class	Parameter	X_{IS1} axis	Y_{IS1} axis	Z_{IS1} axis
Actuation	$\mathbf{G}_{actuation}$ (in m/s ² /V)	-6.86E-08	1.60E-07	1.60E-07
DVA	\mathbf{G}_{DVA} (in V)	-16	-16	-16
	$\mathbf{F}_{CutOffDVA}$ (in Hz)	76	76	76
Control	\mathbf{F}_{pre} (in Hz)	10	30	30
	\mathbf{F}_{post} (in Hz)	10	30	30
	\mathbf{K}_p	-2.0	18.5	18.5
	\mathbf{F}_I (in Hz)	0.004	0.1	0.1
	\mathbf{F}_{D1} (in Hz)	0.05	0.25	0.25
	\mathbf{F}_{D2} (in Hz)	1	20	20
	\mathbf{F}_C (in Hz)	5	25	25
Capacitive Sensor	\mathbf{G}_{det} (in V/F)	82E+12	-17E+12	-17E+12
	$\mathbf{F}_{CutOffDet}$ (in Hz)	167	167	167
Capacitive Transducer	\mathbf{G}_{fm} (in F/m)	3.69E-09	-1.29E-08	-1.29E-08
Stiffness	ω_p^2 (in s ⁻²)	3.2E-03	-0.0715	-0.0715

Table B.2: Values of the control functions parameters for the external test-mass of the SUEP instrument

External Test-mass IS2 - SUEP instrument				
Class	Parameter	X_{IS2} axis	Y_{IS2} axis	Z_{IS2} axis
Actuation	$\mathbf{G}_{actuation}$ (in m/s ² /V)	$-8.01E-08$	$9.85E-07$	$9.85E-07$
DVA	\mathbf{G}_{DVA} (in V)	-16	-16	-16
	$\mathbf{F}_{CutOffDVA}$ (in Hz)	76	76	76
Control	\mathbf{F}_{pre} (in Hz)	10	30	30
	\mathbf{F}_{post} (in Hz)	10	30	30
	\mathbf{K}_p	-1.9957	2.22	2.22
	\mathbf{F}_I (in Hz)	0.004	0.1	0.1
	\mathbf{F}_{D1} (in Hz)	0.05	0.25	0.25
	\mathbf{F}_{D2} (in Hz)	1	20	20
	\mathbf{F}_C (in Hz)	5	25	25
Capacitive Sensor	\mathbf{G}_{det} (in V/F)	$40E+12$	$-5E+12$	$-5E+12$
	$\mathbf{F}_{CutOffDet}$ (in Hz)	167	173	173
Capacitive Transducer	\mathbf{G}_{fm} (in F/m)	$6.46E-09$	$-5.94E-08$	$-5.94E-08$
Stiffness	ω_p^2 (in s ⁻²)	$3.8E-03$	-0.42	-0.42

Table B.3: Values of the control functions parameters for the external test-mass of the SUREF instrument

External Test-mass IS2 - SUREF instrument				
Class	Parameter	X_{IS2} axis	Y_{IS2} axis	Z_{IS2} axis
Actuation	$\mathbf{G}_{actuation}$ (in m/s ² /V)	$-5.34E-08$	$4.36E-07$	$2.18E-07$
DVA	\mathbf{G}_{DVA} (in V)	-16	-16	-16
	$\mathbf{F}_{CutOffDVA}$ (in Hz)	76	76	76
Control	\mathbf{F}_{pre} (in Hz)	10	30	30
	\mathbf{F}_{post} (in Hz)	10	30	30
	\mathbf{K}_p	-3.0025	5.0129	5.0129
	\mathbf{F}_I (in Hz)	0.004	0.1	0.1
	\mathbf{F}_{D1} (in Hz)	0.05	0.25	0.25
	\mathbf{F}_{D2} (in Hz)	1	20	20
	\mathbf{F}_C (in Hz)	5	25	25
Capacitive Sensor	\mathbf{G}_{det} (in V/F)	$40E+12$	$-5E+12$	$-5E+12$
	$\mathbf{F}_{CutOffDet}$ (in Hz)	172	168	168
Capacitive Transducer	\mathbf{G}_{fm} (in F/m)	$6.46E-09$	$-5.94E-08$	$-5.94E-08$
Stiffness	ω_p^2 (in s ⁻²)	$4.6E-03$	-0.11	-0.11

Detailed results of the calibration sessions processing

This appendix will present the detailed results of the calibration sessions processing.

C.1. K_{1dx} calibration sessions

Table C.1: Processing of the $K_{1dx-DFIS2}$ calibration sessions and 3- σ estimation of $(\alpha_{XYIS1} - \alpha_{XYIS2})$ and $(\alpha_{XZIS1} - \alpha_{XZIS2})$ for the SUREF instrument

K_{1dx} calibration session - SUREF - DFIS2		
Session Number	$\alpha_{XYIS1} - \alpha_{XYIS2}$	$\alpha_{XZIS1} - \alpha_{XZIS2}$
128	0,102989	-0,014319
172	0,102016	-0,014916
192	0,103162	-0,015119
286	0,102300	-0,015856
296	0,102893	-0,016571
302	0,103994	-0,017329
308	0,104091	-0,017664
374	0,101630	-0,015621
382	0,103263	-0,015882
450	0,106918	-0,017665
Mean Value	0,103	-0,016
Standard Deviation σ	0,001	0,001
3-σ result	0,103 \pm 0,003	-0,016 \pm 0,003

Table C.2: Processing of the $K_{1dx-DFIS1}$ calibration sessions and 3- σ estimation of $(\alpha_{XYIS2} - \alpha_{XYIS1})$ and $(\alpha_{XZIS2} - \alpha_{XZIS1})$ for the SUREF instrument

K_{1dx} calibration session - SUREF - DFIS1		
Session Number	$\alpha_{XYIS2} - \alpha_{XYIS1}$	$\alpha_{XZIS2} - \alpha_{XZIS1}$
70	-0,100858	0,013031
114	-0,101770	0,013541
Mean Value	-0,1013	0,0133
Standard Deviation σ	0,0006	0,0004
3-σ result	-0,1013 \pm 0,0018	0,0133 \pm 0,0012

C.2. Θ_{dz} calibration sessions

Table C.3: Processing of the $\Theta_{dz-DFIS2}$ calibration sessions and 3- σ estimation of $(\alpha_{YXIS1} - \alpha_{YXIS2})$ and $(\alpha_{YZIS1} - \alpha_{YZIS2})$ for the SUEP instrument

Θ_{dz} calibration session - SUEP - DFIS2		
Session Number	$\alpha_{YXIS1} - \alpha_{YXIS2}$	$\alpha_{YZIS1} - \alpha_{YZIS2}$
220	-8,13E-04	4,608E-03
244	-5,15E-04	2,558E-03
262	-3,57E-04	1,458E-03
426	-5,09E-04	1,421E-03
Mean Value	-5E-04	3E-03
Standard Deviation σ	2E-04	1E-03
3-σ result	$[-5 \pm 6] \cdot 10^{-4}$	$[3 \pm 3] \cdot 10^{-3}$

Table C.4: Processing of the $\Theta_{dz-DFIS2}$ calibration sessions and 3- σ estimation of $(\alpha_{YXIS1} - \alpha_{YXIS2})$ and $(\alpha_{YZIS1} - \alpha_{YZIS2})$ for the SUREF instrument

Θ_{dz} calibration session - SUREF - DFIS2		
Session Number	$\alpha_{YXIS1} - \alpha_{YXIS2}$	$\alpha_{YZIS1} - \alpha_{YZIS2}$
122	-5.01E-04	2.145E-03
178	-3.90E-04	2.097E-03
290	-5,1E-05	2.173E-03
Mean Value	-3E-04	2,14E-03
Standard Deviation σ	2E-04	4E-05
3-σ result	$[-3 \pm 6] \cdot 10^{-4}$	$[2, 14 \pm 0, 12] \cdot 10^{-3}$

C.3. Θ_{dy} calibration sessions

Table C.5: Processing of the $\Theta_{dy-DFIS2}$ calibration sessions and 3- σ estimation of $(\alpha_{ZXIS1} - \alpha_{ZXIS2})$ and $(\alpha_{ZYIS1} - \alpha_{ZYIS2})$ for the SUEP instrument

Θ_{dy} calibration session - SUEP - DFIS2		
Session Number	$\alpha_{ZXIS1} - \alpha_{ZXIS2}$	$\alpha_{ZYIS1} - \alpha_{ZYIS2}$
222	2.70E-04	-4.75E-4
242	4.41E-04	-5.63E-04
258	2.43E-04	-4.69E-04
424	6.06E-04	-9.45E-04
Mean Value	4E-04	-6E-04
Standard Deviation σ	2E-04	2E-04
3-σ result	$[4 \pm 6] \cdot 10^{-4}$	$[-6 \pm 6] \cdot 10^{-4}$

Table C.6: Processing of the $\Theta_{dy-DFIS2}$ calibration sessions and 3- σ estimation of $(\alpha_{ZXIS1} - \alpha_{ZXIS2})$ and $(\alpha_{ZYIS1} - \alpha_{ZYIS2})$ for the SUREF instrument

Θ_{dy} calibration session - SUREF - DFIS2		
Session Number	$\alpha_{ZXIS1} - \alpha_{ZXIS2}$	$\alpha_{ZYIS1} - \alpha_{ZYIS2}$
124	-1,89E-04	-1,364E-03
180	-3,23E-04	-1,359E-03
288	-1,88E-04	-1,276E-03
Mean Value	-2,3E-04	-1,33E-03
Standard Deviation σ	8E-05	5E-05
3-σ result	$[2, 3 \pm 2, 4] \cdot 10^{-4}$	$[-1, 33 \pm 0, 15] \cdot 10^{-3}$

Outputs provided by the simulator

This appendix will present the outputs provided by the instrument simulator for various simulations. Two cases are distinguished: in the first case, the *Simulink* simulator uses the linear-to-linear coupling factors first estimates (as seen in section 3.3), while in the second case, it uses the adjusted values of the linear-to-linear coupling factors (presented in section 3.4).

D.1. Simulator using the linear-to-linear coupling factors first estimates

In this first section, the instrument simulator uses the linear-to-linear coupling factors first estimates presented in Table 3.9.

D.1.1. Simulation n°2: Satellite oscillation along the Y-axis

During this simulation, a sinusoid of amplitude $0.01V$ and frequency $f_{tech} = 0.1\text{Hz}$ is induced in the satellite motion **along the Y-axis**: $E'_Y(t) = 0.01 \cdot \sin(2\pi(0.1)t)$. The following figures illustrate the outputs provided by each sensor of the simulator during the simulation:

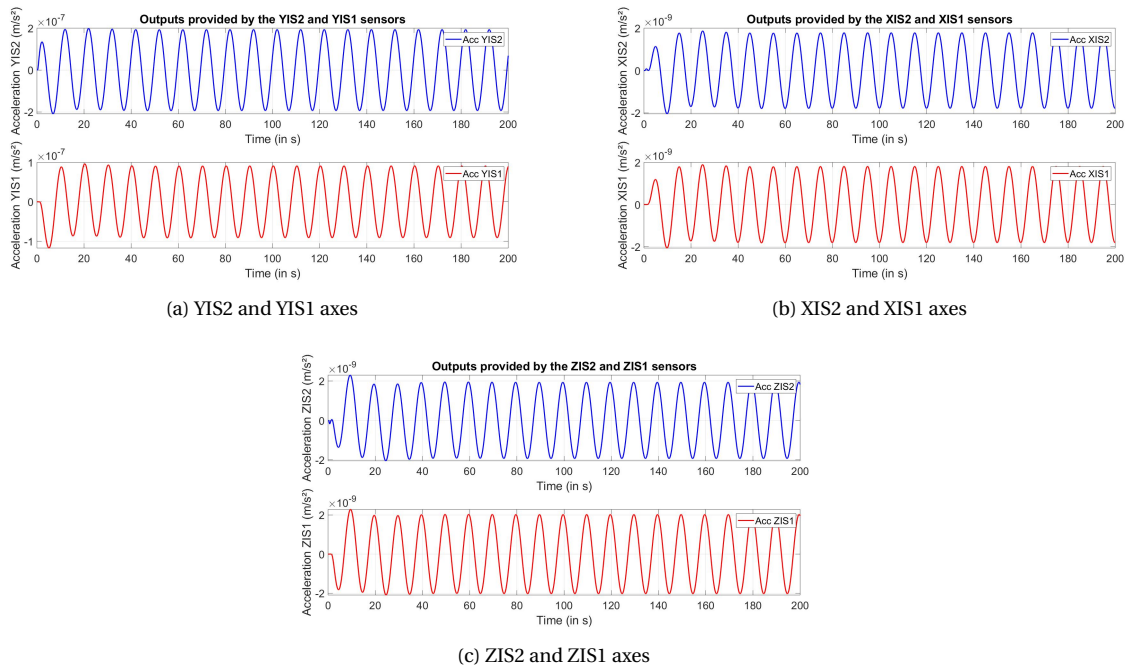


Figure D.1: Outputs provided by the simulator for the second simulation (Excitation along the Y-axis) - **Coupling factors first estimates**

D.1.2. Simulation n°3: Satellite oscillation along the Z-axis

Throughout this simulation, a sinusoid of amplitude 0.01V and frequency f_{tech} is induced in the satellite motion **along the Z-axis**: $E'_Z(t) = E'_Y(t) = 0.01 \cdot \sin(2\pi(0.1)t)$. Once again, the following figure illustrates the outputs provided by each sensor of the simulator during the simulation.

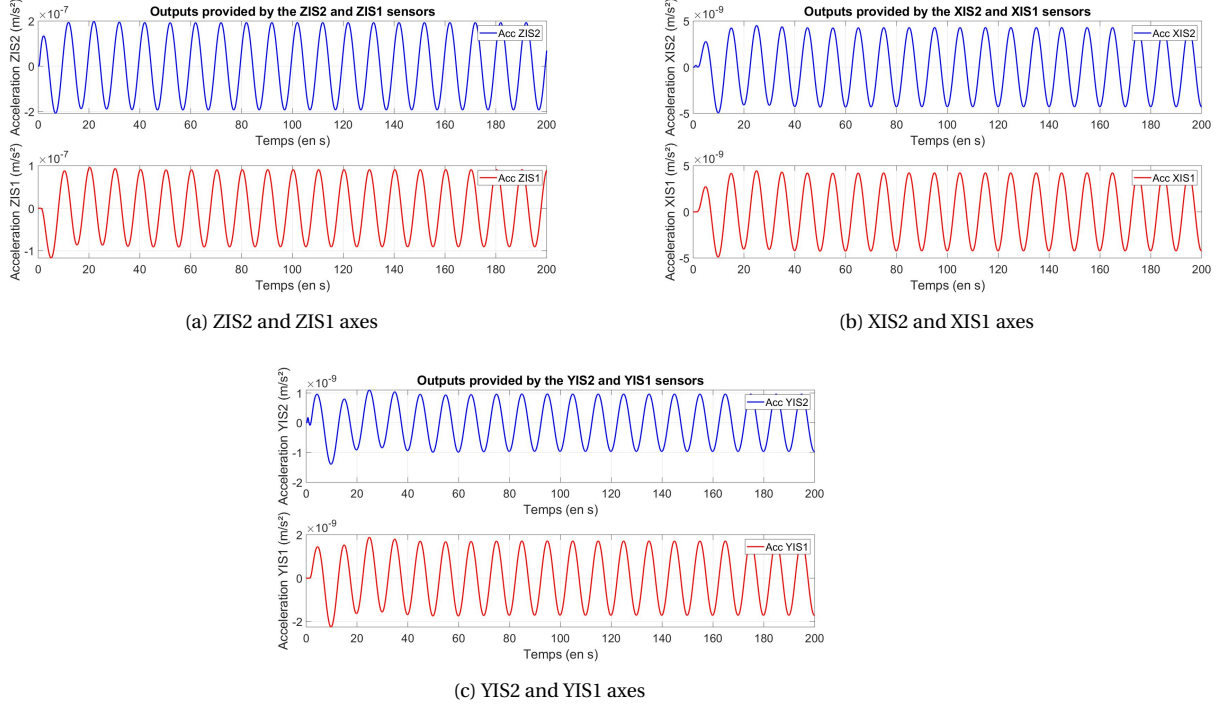


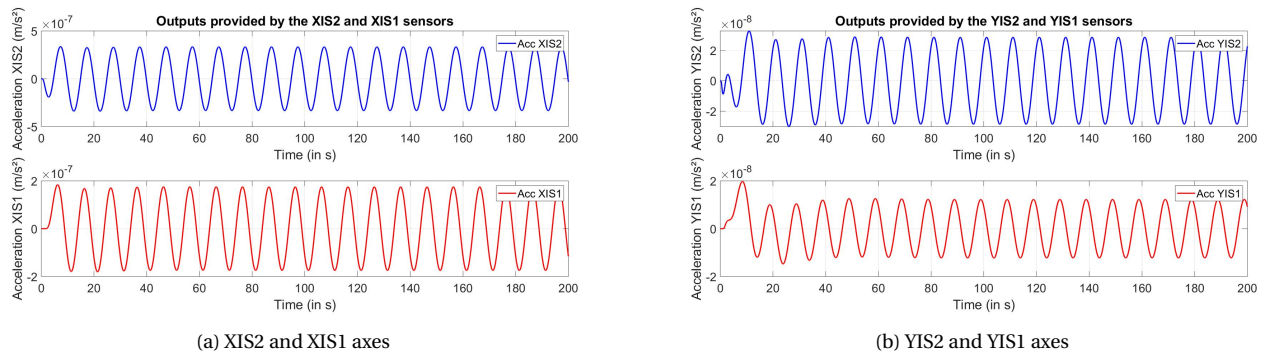
Figure D.2: Outputs provided by the simulator for the third simulation (Excitation along the Z-axis) - **Coupling factors first estimates**

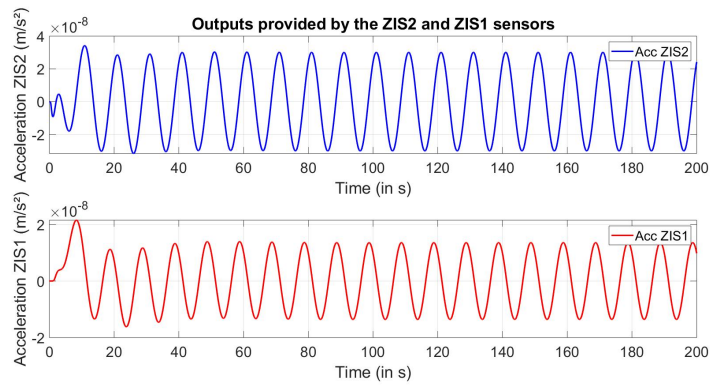
D.2. Simulator using the adjusted linear-to-linear coupling factors

In this second section, the instrument simulator now uses the linear-to-linear coupling factors adjusted values, as seen in [Table 3.12](#).

D.2.1. Simulation n°1: Satellite oscillation along the X-axis

During this simulation, a sinusoid of amplitude 0.148V and frequency f_{tech} is applied in the instrument control loop to force an oscillation of the test-mass **along the X-axis**: $E'_X(t) = 0.148 \cdot \sin(2\pi(0.1)t)$.



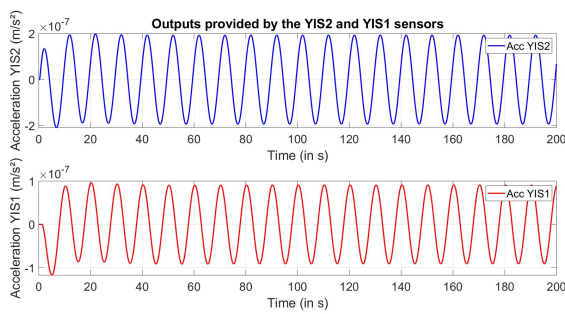


(a) ZIS2 and ZIS1 axes

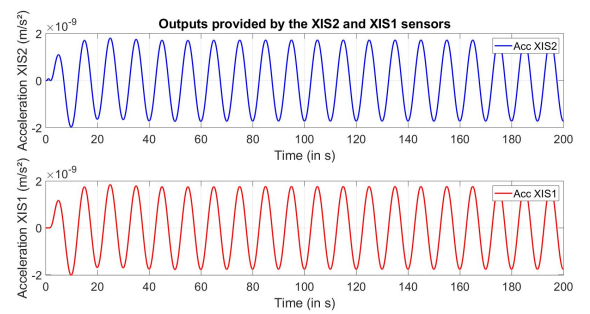
Figure D.3: Outputs provided by the simulator for the first simulation (Excitation along the X-axis) - **Coupling factors adjusted values**

D.2.2. Simulation n°2: Satellite oscillation along the Y-axis

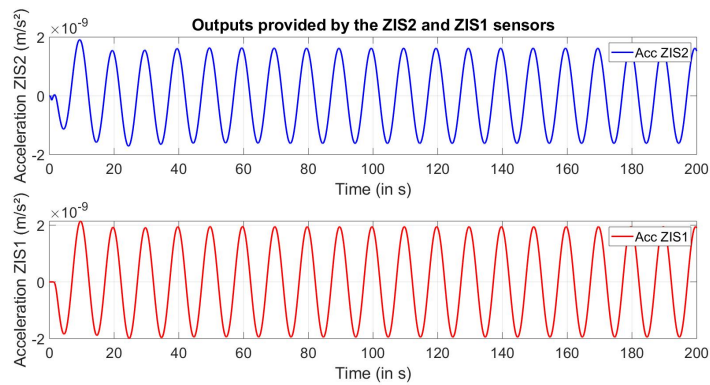
The same simulation as the one introduced in the previous section (oscillation **along the Y-axis**) is run with the simulator new settings.



(a) YIS2 and YIS1 axes



(b) XIS2 and XIS1 axes

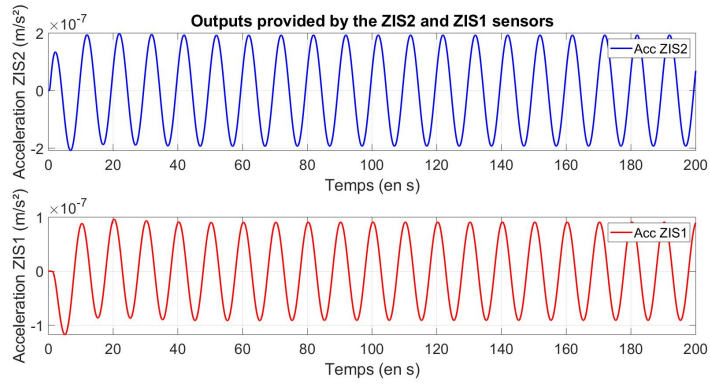


(c) ZIS2 and ZIS1 axes

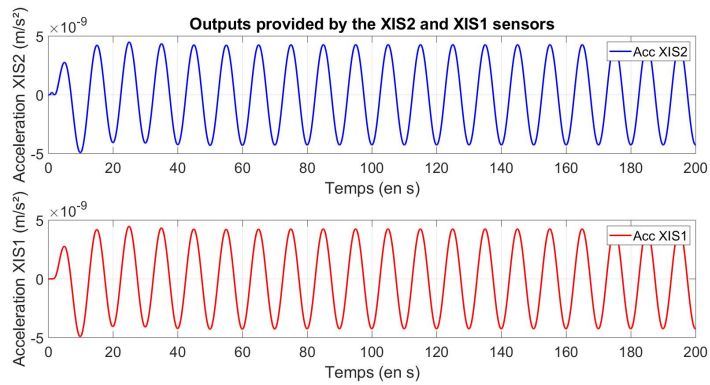
Figure D.4: Outputs provided by the simulator for the second simulation (Excitation along the Y-axis) - **Coupling factors adjusted values**

D.2.3. Simulation n°3: Satellite oscillation along the Z-axis

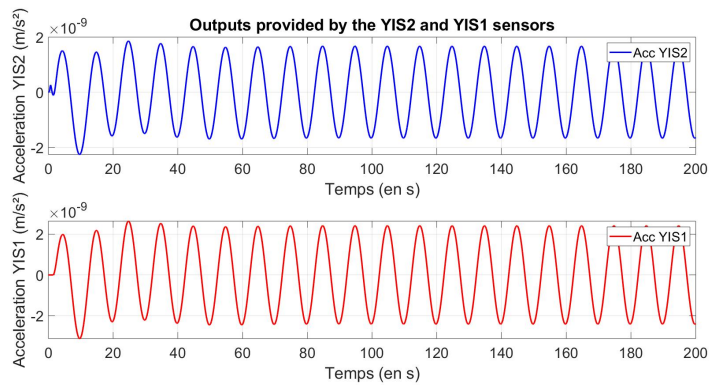
Finally, the same simulation as the one introduced in the previous section (oscillation **along the Z-axis**) is run with the simulator new settings.



(a) ZIS2 and ZIS1 axes



(b) XIS2 and XIS1 axes



(c) YIS2 and YIS1 axes

Figure D.5: Outputs provided by the simulator for the third simulation (Excitation along the Z-axis) - **Coupling factors adjusted values**